Photocatalysis in a New Light: A Biohybrid Approach for Improved Reactivity with Tunable, Low-Energy Light Excitation

by

Paul T. Cesana

B.S., University of Rhode Island (2019)

Submitted to the Department of Chemistry
in partial fulfillment of the requirements for the degree of

DOCTOR OF PHILOSOPHY IN CHEMISTRY

at the

MASSACHUSETTS INSTITUTE OF TECHNOLOGY

SEPTEMBER 2024

Authored by: Paul T. Cesana…………………………………………………………………………
                   Department of Chemistry
                   August 5th, 2024

Certified by: Gabriela S. Schlau-Cohen………………………………………………………..
                   Professor of Chemistry
                   Thesis Supervisor

Accepted by: Adam P. Willard…………………………………………………………………….
                   Professor of Chemistry
                   Graduate Officer

This doctoral thesis has been examined by a committee of the
Department of Chemistry as follows:

Professor Moungi G. Bawendi…………………………………………………...………
                                                                Thesis Committee Chair
                                                                Lester Wolfe Professor of Chemistry

Professor Gabriela S. Schlau-Cohen…………………………………………………..
                                                                Thesis Supervisor
                                                                Professor of Chemistry

Professor Adam P. Willard………………………………………………………………….
                                                                Thesis Committee Member
                                                                Professor of Chemistry

Photocatalysis in a New Light: A Biohybrid Approach for Improved Reactivity with Tunable, Low-Energy Light Excitation

by

Paul T. Cesana

Submitted to the Department of Chemistry on August 5th, 2024
in partial fulfillment of the requirements for the
Degree of Doctor of Philosophy in Chemistry

ABSTRACT

Since the advent of photoredox catalysis, much thought has been devoted to the development of exciting reaction modalities and the catalysts which perform these reactions. Less thought has been placed into the specific aspects of light absorption as the key step in photocatalytic mechanisms. Natural photosynthetic systems drive the high-energy reactions of photosynthesis with efficient and broadband energy capture. They provide a blueprint toward optimizing these processes in synthetic systems. In photosynthesis, both light capture and reactivity have been optimized by separation into distinct sites. The dominant process by which absorbed sunlight is transferred between these sites is through resonance energy transfer, which is highly efficient over long distances. This work highlights that light capture and energy transfer are crucial steps for the design of highly efficient photocatalysts in the future.

Chapter 1 describes the relevant structures in natural photosynthesis as inspiration for synthetic approaches, the different mechanisms of energy transfer, and examples of photocatalytic systems that harness such excitation transfer processes to improve performance. Chapter 2 reports the synthesis of a biohybrid photocatalyst inspired by the modular architecture of photosynthetic apparatus which conjugated a photosynthetic light harvesting protein to a transition metal photocatalyst. Spectroscopic investigation found that absorbed photoenergy was efficiently funneled from the light harvester to the photocatalyst. The utility of the biohybrid photocatalyst was demonstrated via an increase in yields for two test reactions, including enabled reactivity at red wavelengths where the photocatalyst alone does not absorb. Chapter 3 establishes the power of incorporating nature's design into non-natural photoenzymatic catalysis, generalizing the approach to other systems and methodologies. Photoenzymes require high-intensity light to function because of the poor absorption properties of their photoactive intermediate. A conjugate composed of a covalently linked photoenzyme and light antennae separates light capture from catalysis. Spectroscopic characterization of the conjugate showed the presence of efficient energy transfer from the light-harvesting components to the photoenzyme. In the presence of energy transfer, a maximum ~4-fold increase in product yields was observed as well as enabled reactivity. Chapter 4 highlights spectroscopic exploration into emerging molecular catalyst species. Finally, Chapter 5 provides an outlook to the future possibilities of the topics presented herein.

Thesis supervisor: Gabriela S. Schlau-Cohen
Title: Professor of Chemistry

ACKNOWLEDGEMENTS

I am extremely lucky to be surrounded by a great number of fantastic people who push my work forward, support me through challenges, and deal with me every day (not the easiest task).

I thank first my advisor, Prof. Gabriela Schlau-Cohen, for not only leading the charge throughout the past five years, culminating in some successful, impactful science, but also for vastly improving my scientific communication skills in presentation and written form. Her useful words of advice will be seared in my brain for years to come. For example, the intentional use of color in figures, as well as white space (it frames the image). I will similarly be forever grateful to her for giving me the chance to study at MIT, a place I simply could not have imagined attending growing up.

I thank my thesis committee members, Prof. Moungi Bawendi and Prof. Adam Willard for their helpful feedback throughout my career here. Moungi somehow made quantum mechanics easily understandable and accessible in his 5.73 course and was open to all discussion in our thesis chair meetings.

For the work specifically, I thank my collaborators and BioLEC, an energy frontier research center funded by the U.S. Department of Energy. I was lucky enough to collaborate with Profs. David MacMillan, Abigail Doyle, Felix Castellano, Todd Hyster, Jenny Yang, Guido Clever, many others, and their lab members, each of whom provided excellent feedback and assistance.

All of the members of the Schlau-Cohen lab past and present have made my time here more enjoyable. I could tell a story about each of you, and we all know I'm prone to telling stories, but there simply is not enough time or pages. I would like to highlight those in my lab cohort – Audrey Norris, Maddie Hoffmann, Shirley Chen, and Angela Lee for being there from academic day one. Other members of the cohort deserve major shout-outs – Sarah Quinn, David Berkinsky, Tara Sverko, and anyone else I'm likely forgetting at the moment.

From personal day one, I thank my family – Suzanne Cesana (mom), Paul Cesana (dad), Dina Cesana (aunt), Milan Cesana (cousin), and everyone else. You are the strongest, most resilient people I know, and I thank you for making me the person I am today. None of my achievements could have been accomplished without your constant support.

Life is a series of ups and downs, filled with any number of challenges that we encounter on a daily basis, whether that be in our professional or personal lives. Grad school, while hard enough on its own, comes at a period in life of great uncertainty about the future, only adding to the stress. Surrounding yourself with people who care, people who make you laugh and smile, people who foster positivity, is essential. It is never the place that you remember, it is those you spent the time with while there. I am lucky to have been surrounded by and supported by all of you, and those not mentioned too. You have made a lasting impact, and I thank you all for it.

TABLE OF CONTENTS

LIST OF FIGURES

LIST OF TABLES

CHAPTER 1:
INTRODUCTION – BIOINSPIRED LIGHT-HARVESTING STRATEGIES AS APPLIED TO PHOTOCATALYSIS

The power granted by photocatalysis cannot be overstated, as it affords chemical reactivity previously thought to be inaccessible.[1–3] Over the last few decades, the ability to access high energy reactive intermediates through controlled photon absorption has led to a swath of new reaction methodologies, expanded the scope of available substrates, and forged new approaches through multidisciplinary collaboration.[4] In a typical photocatalytic reaction, the photocatalyst absorbs light and enters a high-energy electronically excited state. In the next step, it either transfers the energy or an electron to a substrate which then undergoes the desired reaction to an intermediate or the product. If an electron was transferred, the photocatalyst is regenerated by a suitable electron donor (which can also be an intermediate formed by the substrate). Such light-driven reactions can be more selective than thermal chemistry, as ideally only the photocatalyst absorbs the input light and translates it to useful reactivity. Photonic energy is more efficient than thermal energy as frequently used LED light sources run with extremely low needed energy inputs, even if that energy is often produced via fossil fuels. Light losses, while common, can be accounted for via alterations in illumination level, absorber concentration, or reactor design.[5,6] The photocatalytic scheme also takes advantage of the high energy of visible light. The absorption of a 450 nm photon corresponds to the input energy of super-heating to 32,000 K. With this combination of selectivity and high energy input, these reactions can be performed under mild conditions which additionally limits thermal side reactions and energy consumption.

As solar energy becomes increasingly relevant to power homes and transportation, it can also be utilized to power chemical reactivity directly, with the goal of one day performing industrial chemical production via sunlight. While photons may seem to be an affordable and endless source

of energy, they are not inherently free.[7,8] In addition, many photochemical transformations are currently light-limited. Hence, it is important to consider how light can be injected most efficiently in photocatalytic systems.[5] Commonly used photoredox catalysts, such as ruthenium (II) tris-bipyridine ($[Ru(bpy)_3]^{2+}$) or iridium (III) tris-phenylpyridine ($[Ir(ppy)_3]^{3+}$), are broadly applied to a variety of reactions and substrates.[1,2] These catalysts are fulfilling two distinct functions at once, trying to strongly and efficiently harvest light *and* convert it into chemical reactivity, often unintentionally restricting both for a happy medium. Similarly, *how* this energy is utilized for capture and reactivity remains underexplored, and this step should be considered in photocatalyst design.

While an in-depth discussion of reactivity is outside of this perspective's scope, light capture properties of most photocatalysts are limited especially in comparison to natural photosynthetic machinery, both in terms of absorption cross sections and bandwidths. Absorption cross sections or molar absorption coefficients for photocatalysts based on transition metal complexes and organic molecules are typically on the order of 10^3–10^4 M^{-1} cm^{-1}.[1,2,9–12] Some small molecule organic dyes can absorb light an order of magnitude more strongly, and metal nanoparticles and semiconductors can reach molar absorption coefficients in the billions due to strong delocalization of their electron clouds.[13–17] To best use the broad solar spectrum reaching earth, a broad absorption bandwidth is desirable.[18] However, most molecular systems show relatively narrow absorption bands that only cover a small spectral range with typical bandwidths of 50–100 nm.[1,2,9–12 18]

Efforts to improve the absorption properties of a photocatalyst often affect its reactivity. For example, increasing the molar absorption coefficient often leads to a red-shift of the absorption spectra which also lowers the energy of the photoreactive states.[19] Therefore, methods to preserve

high energy reactivity while increasing light capture are desirable.[20–23] A very promising approach is decoupling light absorption and reactivity as found in natural photosynthesis.[24–26] Here, light is absorbed by an array of antenna proteins that funnel the excitation energy to the reaction center (RC) where chemical transformation occurs (Figure 1.1a). The modular nature of the system allows both components to evolve separately for their respective functions. These systems absorb a respectably large portion of the solar spectrum with much higher photon capture than synthetic systems, and broadened light capture allows for a broadened reaction scope (Figure 1.1b). This perspective seeks to lay the groundwork for applying this design principle of natural photosynthesis in the architecture of tailored photocatalysts at large. First, we will discuss different excitation transfer mechanisms and briefly discuss biological systems and their overarching similarities. Then, recent literature examples will be highlighted and compared to nature's chosen method of excitation. Finally, the potential to utilize bioinspiration in catalyst design for greater mechanistic control of novel reactivity will be posited.
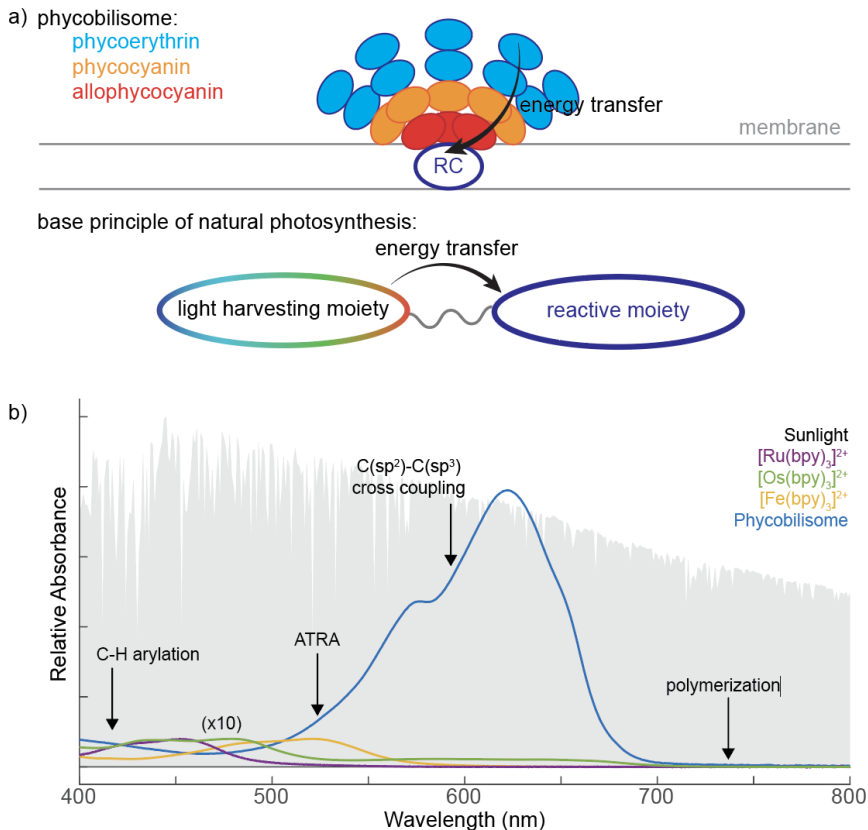
Figure 1.1: Bioinspiration from natural organisms. (a) Structure of the light harvesting supercomplex, the phycobilisome and the base principles nature utilizes for photosynthetic light harvesting to funnel energy to the reaction center (RC). (b) The relative absorption spectrum comparison of sunlight, the phycobilisome, three common d^6 tris-bipyridyl photoredox catalysts scaled in their relative absorption by a factor of 10 and based on the maximum of their molar absorption coefficients, and examples of reactions catalyzed in literature at their irradiated wavelengths. ATRA = atom transfer radical addition.

1.1 BIOINSPIRATION FROM NATURAL DESIGN

The most logical step to take when trying to optimize light capture is to look to natural photosynthetic systems, which have evolved over millennia to harness sunlight and power nearly all life on earth. The architecture many organisms have in common is the separation and individual optimization of proteins for light harvesting and reactivity.[24,25] These moieties are energetically, and sometimes physically, connected to one another to maximize energy utilization. The intensity of sunlight at or below ground level is very low which is why efficient light capture is essential for

photosynthetic organisms. Hence, most photosynthetic light harvesting complexes have molar absorption coefficients on the order of 10^6 M^{-1} cm^{-1} with multi-chromophoric assemblies stretching absorption bandwidths above 100 nm (Figure 1.1b).[24,27] In addition, light harvesting modalities often outnumber reactive modalities by large ratios (up to 400:1 in higher plants and green algae).[24] The excitation energy in the light harvesting proteins is transported to reaction centers via Förster resonance energy transfer (FRET) which can act over long ranges of tens of nanometers with high efficiency (see Section 1.2 for more details). At the reaction center the photonic energy is finally converted to separated charges typically with near unity quantum yields.[28]

In the following, the architectural design features of selected photosynthetic organisms will be described to deliver a salient point: it does not take much structural effort to divide and conquer the processes of light harvesting and reactivity. Green plants have the most optimized and organized structures, where chloroplast organelles contain stacked thylakoids with light harvesting proteins assembled in membranes.[29] The Light Harvesting Complexes II and I, commonly LHCII and LHCI, absorb photons, efficiently transfer energy within their pigment-protein structures, and generate electrons. These electrons are transported along a chain of redox relays and finally converted into chemical energy, e.g. by establishing a proton gradient or synthesizing ATP or NADPH.[30,31] Red algae and cyanobacteria, among other organisms, possess a phycobilisome (Figure 1.1a), which contain different light harvesting proteins which each absorb a certain spectral range, such as phycoerythrin ($\sim$500-575 nm, ε_{max} = 1.96 x 10^6 M^{-1} cm^{-1}), phycocyanin ($\sim$560-630 nm, ε_{max} = 1.54 x 10^6 M^{-1} cm^{-1}), and allophycocyanin ($\sim$575-660 nm, ε_{max} = 0.70 x 10^6 M^{-1} cm^{-1}). These proteins are stacked into rods that in turn cluster around a central reaction center on the membrane. Within this structure, the proteins transport excitation energy following an energy gradient with near unity quantum yield.[27,32–35] In contrast to the highly structured photosynthetic

machinery discussed above, purple bacteria possess much more disordered lilypad-like structures. Here, the membrane is populated with reaction centers, an equivalent stoichiometric ratio of light harvesting complex I (LHI) encircling the reaction center, and a greater abundance (~3-7x depending on light conditions and species) of light harvesting complex II (LHII).[36,37] Energy is transferred among LHII to LHI and then to reaction centers to complete the photosynthetic process.[38,39] Lastly, cryptophyte algae show the lowest complexity. These organisms only possess one type of light harvesting proteins, typically phycoerythrins, which are assembled in the intermembranous space and transfer energy indiscriminately amongst one another until reaching the reactive protein.[29,40]

The key takeaway from this discussion is that architectures for distributed light harvesting and reactivity do not need to be complicated to be efficient. While physical connection between light harvesting and reactive species may strengthen energy transfer between species due to a shorter distance, even it is not strictly required. Finally, a note on artificial photosynthesis, which are synthetic methods to replicate the reactions of photosynthesis with photoactivation, such as CO_2 reduction and water oxidation.[41–43] While this perspective mainly focuses on light absorption aspects, the number of reactions that photosynthetic design could be applied to are not limited to just the reactions of photosynthesis – increased light capture can broadly benefit photocatalytic reactions.

1.2 THE THREE MAJOR MECHANISMS OF EXCITATION TRANSFER

Firstly, the three major mechanisms of excitation transfer, Förster resonance energy transfer (FRET), Dexter energy transfer (DET), and electron transfer (ET) are discussed.[44,45] FRET is non-

radiative energy transfer from an electronically excited donor molecule to an acceptor molecule via a transition dipole-dipole interaction. The rate of FRET, k_{FRET}, is described by equations 1–3:

$$(1) \quad k_{\text{FRET}} = \frac{1}{\tau_D^0}\left(\frac{R_0}{r}\right)^6 \qquad (2) \quad R_0^6 = \frac{9\ln(10)\kappa^2\Phi_D^0}{128\pi^5 N_A n^4}J \qquad (3) \quad J = \int F(\lambda)\varepsilon(\lambda)\lambda^4 d\lambda$$

In equation 1, τ_D^0 is the excited state lifetime of the donor in absence of the acceptor, r is the distance between donor and acceptor, and R_0 is the Förster radius, which is the distance at which the energy transfer efficiency is 50%. Equation 2 describes the Förster radius, where κ^2 is a dimensionless value describing the orientation of the donor-acceptor transition dipoles (typically assumed isotropic with a value of 2/3, but can vary between 0 and 4), Φ_D^0 is the luminescence quantum yield of the donor, N_A is Avogadro's constant, n is the refractive index of the medium, and J is the spectral overlap integral between the area-normalized luminescence spectrum of the donor $F(\lambda)$ and the absorption spectrum of the acceptor $\varepsilon(\lambda)$ with the wavelength λ (Eq. 3).

The two main requirements for efficient FRET are energetic connectivity, i.e., spectral overlap between the donor emission and acceptor absorption spectra and a suitable distance r between donor and acceptor species. Because FRET is a dipole-dipole interaction, there is a distance dependence of r^{-6} for k_{FRET}, meaning FRET can be highly efficient over long distances (~10 nm).[44] FRET is typically limited to singlet-singlet energy transfer reactions. While FRET involving triplet states has been reported,[46] its efficiency is severely limited by the low spectral overlap integral J as direct excitations of triplet states are spin-forbidden.

Typically energy transfer processes form thermodynamic products, but photosynthetic organisms are also known to perform uphill energy transfer via FRET.[47,48] These processes occur most easily in longer wavelengths because of the λ^4 term for the spectral overlap integral J (Eq. 3), but they have also been reported for lower wavelengths as well.[49] The kinetic product of energy transfer can be obtained in the uphill direction when additional energy is supplied to the system

(e.g. as thermal energy) and a "trap" state exists which limits back transfer to the donor, such as an intersystem crossing or charge separation.[49,50] Therefore, desirable higher energy reactivity can be obtained from low energy light excitation, as will be described further in the examples below.

Overall, key benefits of FRET include the long operative range and the fact that matching donor-acceptor pairs can be easily identified using routine absorption and emission measurements. A library of potential components can be developed for future conjugate catalyst design, and modeling their energy transfer characteristics is relatively straightforward using the above theory. Then, because the operative distance is long, the complexity of potential linkage strategies between donor and acceptor in conjugate catalyst design is lessened, if desired at all.

DET is a non-radiative excitation transfer mechanism that features simultaneous exchange of electrons between the electronically excited donor and the acceptor in the ground state.[44,45] For this double electron exchange to occur, DET requires orbital overlap between donor and acceptor which results in a steep exponential distance dependence. The rate of DET, k_{DET} (Eq. 4), is:

$$(4) \quad k_{DET} = K J' \exp\left[-\frac{2r}{L}\right] \quad (5) \quad J' = \int F(\lambda)\varepsilon(\lambda)d\lambda$$

where K is a term dependent on the orbital interaction of the donor and acceptor, J' is the overlap integral between fully normalized absorption and emission spectra (Eq. 5), r is the donor-acceptor distance, and L is the sum of the van der Waals radii of the donor and acceptor. Most of these terms are experimentally inaccessible, meaning that rationally designing a system for DET as the operative excitation transfer mechanism is difficult. In contrast to FRET, DET is compatible with singlet and triplet states and a common mechanism for triplet-triplet energy transfer. [44,46]

Electron transfer (ET) is conceptually different from energy transfer as it yields oxidized and reduced donors and acceptors typically in the ground state instead of an acceptor in an excited state. Similar to DET this mechanism of excitation transfer also requires orbital overlap between

donor and acceptor which again results in an exponential distance dependence for the rate k_{ET} as described by Marcus theory.[44,45,51] So, linkages between donor and acceptor must be kept very short (within bond distances) or the collision of species need be relied upon. If diffusion is used as the medium for donor acceptor transfer, the potential for unwanted side reactivity or natural deexcitation increases. Tethering of the species to one another will certainly help, but because individual charges move amongst the components rather than targeted energetic flow, this can still lead to issues of directionality. CV measurements provide a step toward the predictability of ET, by obtaining the ground state oxidation-reduction potentials, spectroelectrochemical measurements can provide insight into the oxidized or reduced species, and theoretical calculations can provide predicted ET rates. All of the listed experimental and theoretical methods are more complicated for prediction as compared to FRET, however.

1.3 APPROACHES TO BIOINSPIRED LIGHT HARVESTING

The transfer of excitation energy from the light harvesting moiety to the reaction center is essential to natural photosynthesis. While FRET is dominant in light harvesting proteins, different mechanisms have been explored in synthetic systems so far. In the following, we seek to highlight examples for different excitation transfer mechanisms where light was harvested efficiently, often to enable reactivity (Figure 1.2). The following approaches to explore light capture and photocatalysis are grouped under "bioinspired light-harvesting" as they align with the core concepts found in the natural processes discussed above, even though they may not have been explicitly reported as such.
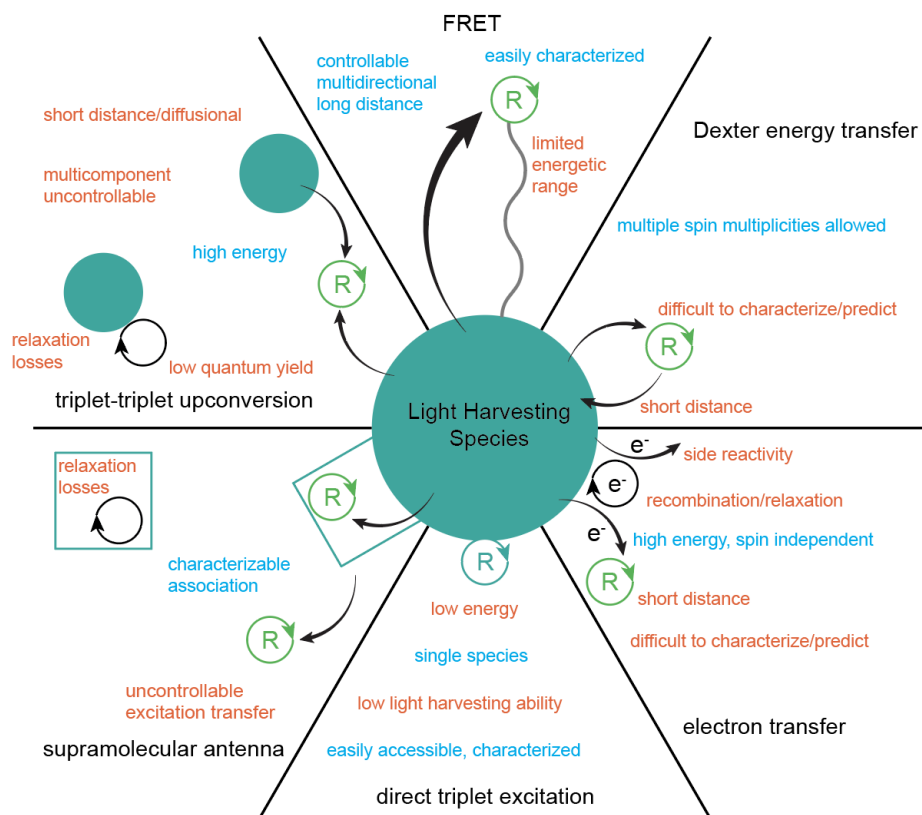
Figure 1.2: Various approaches to improved light harvesting, with their benefits and drawbacks. R stands for the reactive species, and arrows depict excitation movement/relaxation scenarios.

1.3.1 Energy transfer

FRET has mainly been demonstrated for sensitization and expansion of light absorption on large scale macromolecular systems directly utilizing biological systems.[52–56] Hassan Omar et al. conjugated a synthesized molecular absorber, AE_{800}, to the reaction center (RC) of the purple bacteria *R. sphaeroides* which absorbs within the spectral valley of the RC and transfers energy with 62% efficiency to the RC. This conjugation resulted in a 30% increase in the photochemical activity of the RC across the visible light absorption spectrum.[54] Following on this work, Amoruso et al. conjugated a CdTe quantum dot to the same RC which greatly enhanced the absorption spectrum across the visible region, transferred the energy to the RC with 75% efficiency, and

enhanced the modified RC's emission, though reactivity was not examined.[53] Finally, a host guest self-assembled system consisting of a naphthalene modified pyrene derivative and cucurbit[8]uril transferred energy with 49% efficiency to rhodamine B, and the entire system was shown to catalyze a debromination reaction at enhanced product yields up to 98%.[57] These examples highlight that multicomponent systems can utilize light very effectively and result in broad spectrum reactivity. They also highlight other light harvesting systems can be used to enhance these characteristics, with dyes and quantum dots employed.

Much work has been focused on triplet-triplet energy transfer via DET in molecular photocatalysts.[58,59] Triplet states are long-lived (ns–µs) and high enough in energy to enable reactions under mild conditions. In previous studies much focus was put on optimizing reactivity while the efficiency of light capture was mostly neglected. This deviation showcases the many opportunities for collaboration between researchers interested in organic transformations and those interested in light harvesting apparatus and spectroscopy.[4] Some of the most recent and impactful examples of triplet-triplet energy transfer can be found in Ir-Ni co-catalyst systems, which have become an emergent subfield in photocatalysis since the combination of photoredox and nickel catalysis one decade ago.[60] Here, an iridium(III) photosensitizer is posited to transfer its triplet energy after initial excitation to a nickel(II) based co-catalyst, which then performs the desired reaction.[61–63] While this affords unique chemical properties and reactivity, enhances in light absorption are not achieved, as the Ir photosensitizers have relatively small spectral bandwidths centered at 375 nm and molar absorption coefficients ($\sim 10^4$ $M^{-1}cm^{-1}$), especially in comparison to biological systems, as described above. Similarly, the mechanism of excitation transfer is often probed and predicted as much as possible, but it is not targeted during catalyst design, only discovered.[58]

1.3.2 Electron transfer

Electron transfer from a photosensitizer to a catalytic substituent represents another method of excitation transfer with biological underpinnings, as photosynthetic organisms perform sequential electron injections to perform the required reactions.[31] Components such as semiconductor nanoparticles are suitable candidates for electron transfer, as electrons within these systems can delocalize easily across a nanoparticle. They also possess high molar absorption coefficients ($\geq 10^5$ M^{-1} cm^{-1}) and broad enough absorption bandwidths (>100 nm).[64] Transition metal complexes possess smaller absorption bandwidths (50-100 nm) and molar absorption coefficients (10^3-10^4 M^{-1} cm^{-1}) than nanoparticles, but they are amenable to electron transfer because they often possess multiple stable oxidation-reduction states. Utschig, Mulfort, and coworkers have demonstrated directly bioinspired hybrid complexes consisting of a [Ru(bpy)$_3$]$^{2+}$ -ferridoxin-cobalt complex which successfully performed hydrogen evolution after electron transfer from the [Ru(bpy)$_3$]$^{2+}$ to the cobalt complex across the bridging ferridoxin.[65–67] More recently, they reported two biohybrids, [Ru(bpy)$_3$]$^{2+}$-ferridoxin-ferridoxin NADP$^+$ reductase (FNR) and [Ru(bpy)$_3$]$^{2+}$-flavodoxin-FNR, which replaces photosystem I (PSI) from the native photosynthetic system with a transition metal photosensitizer to afford NADPH.[68] The resulting biohybrid was used to study the underlying mechanism of the electron transport process to FNR with the goal of informing future solar energy harnessing design. In the above cases, multiple excitation and electron transfer steps were posited to occur stepwise, either directly from the sensitizer to the reactive component or via the bridge component. Even a relatively straightforward path within a three component biohybrid can have multiple possibilities for stepwise transfer. Dukovic, King, and coworkers have extensively studied quantum dot redox enzyme biohybrids which perform electron transfer from the quantum dot to an enzyme such as a nitrogenase to afford

ammonia from N_2, with a recent report describing the large effect sacrificial electron donors for hole scavenging has on this process.[69–72] These systems are explicitly bioinspired hybrids containing photosynthetic design principles and demonstrate energy relevant reactivity.

All of these systems, though, are limited by exponentially decaying distance dependence of electron transfer and the fact that electron hopping is much less controllable and predictable than energy transfer may be, especially as systems scale in size.[73] Electrons require orbital overlap to jump from species to species in a construct, evoking the "indecisiveness" in mechanism described in the biohybrids exampled above. This requirement also means that donor and acceptor must essentially be bound together with only a few angstroms between them, leading to more challenging synthetic requirements for ground-up catalysts, or reliant on diffusion between components, leading to a complete lack of controllable excitation transfer and an even higher likelihood of side reactivity and deexcitation. FRET, being a concerted deexcitation-excitation mechanism similarly does not require sacrificial electron donors or acceptors, as the excitation transfers without electron movement, leading to even lesser consideration of complications on light harvesting and excitation transfer. Finally, nanoparticles can have defects in their formulation, leading to excitation traps or relaxation, or when used for organic transformations, the surface substituents appended to the nanoparticle can prevent an acceptor species from obtaining the charge.[74,75]

1.3.3 Direct triplet excitation

Another method of expanding absorption to more fully cover the solar spectrum, especially toward red-near IR excitation, is to directly excite species in solution through strongly absorbing triplet states.[19,76] Because triplet states are formally spin forbidden, the molar absorption coefficients of these complexes is low (10^2 M^{-1} cm^{-1}). Using the Beer-Lambert law, $A = \varepsilon bc$ where

ε is the molar absorption coefficient, b is the path length of absorbing material, and c is the concentration, equivalent absorption to a more strongly absorbing species is achieved with a longer effective path length. This penetration depth argument means that red light absorbed less strongly by a triplet state can travel deeper into a reaction mixture, and initiate reactions nearly throughout the entire vessel. Energy loss via intersystem crossing is also avoided because the reactive triplet state is directly excited. Singlet-triplet absorptions can extend into the far-red visible region (~700 nm) for some transition metal complexes with moderate absorption coefficients (~400 $M^{-1} cm^{-1}$).[76] Transitions of this type with any appreciable strength require strong spin orbit coupling, and so very heavy metal centers are often required to make complexes of this type. Red light above 600 nm is also considered to be the phototherapeutic window of excitation.[19,77] The Rovis lab has pioneered the use of spin-forbidden excitation (SFE) complexes as sensitizers for organic transformations.[76,78–80] The initial report focused on Os-centered complexes, which when excited with 740 nm lamps, could directly catalyze photopolymerizations or photoredox reactions in high yields (>74%), or when combined with another metal species, such as Cu, Co, Ni, and Pd complexes, and used as a sensitizer, could perform challenging metallaphotoredox reactions with up to 92% product yield.[76] This approach has been extended to use $[Os(phen)_3]^{2+}$ as a sensitizer and single electron donor in combination with $NiBr_2$ for C-N cross coupling reactions[80] and in combination with Ru-catalyzed olefin metathesis to polymer synthesis under NIR light excitation.[79] Finally, the group developed modified Ir(III) based catalysts with conjugated ligands which could be excited by low energy orange light (595 nm) directly to their triplet states to demonstrate the first low-energy metallaphotoredox $C(sp^2)$-$C(sp^3)$ cross-coupling.[78]

One can counter with two main arguments to this approach: weaker absorption (photon utilization) means that the process is overall less energy efficient at equivalent catalyst loadings,

and redder absorption means that the number of accessible reactions to catalyze can be limited to lower energies. Triplet states, even when strong enough to be accessed directly, often only absorb with molar absorption coefficients on the order of 10^1-10^2 M^{-1} cm^{-1}, which are much weaker than charge transfer or many singlet transitions. Even with the benefits of high spin orbit coupling of transition metal complexes, these transitions are spin-forbidden, leading to their lower absorption properties. Considering the penetration depth argument, while valid, higher overall photon absorption afforded by an optimized light harvesting biohybrid can lead to vastly reduced catalyst loadings with likely the same number of reaction initiations. A dedicated light absorber appended to the catalytic species may be able to increase the amount of triplet excitation even further. The high spin orbit coupling of these catalysts means intersystem crossing is extremely facile. Then, FRET to these red absorbing complexes is predicted to be strong because longer wavelengths result in more efficient FRET, as the spectral overlap integral depends on λ^4 (Eq. 3). Finally, while pushing photon absorption redder is a major goal, redder light is much lower in energy than blue-to-UV light. Ir(ppy)$_3$ is partly so popular as a photocatalyst because of its near-visible 375 nm ^{1}MLCT absorption and ~60 kcal/mol triplet state energy. High energy reactivity with low energy absorption is extremely desirable, and near-IR, low-absorbing triplet states are insufficient for this need.[58]

1.3.4 Supramolecular chemistry approaches

Supramolecular host guest approaches to catalysis are another fascinating research direction. These systems slightly mimic the active sites of enzymes by non-covalently binding reactants within a host molecule, and have been explored for their use in molecular machines and biomedical applications.[43,81–84] For photochemistry, one can use a supramolecular host system as an antenna complex that binds a catalyst or substrate. The host molecule can transfer its excitation

after photoexcitation to the bound guest, allowing the guest to perform reactivity. The supramolecular chemistry approach is more selective to certain guests than strictly reliant on diffusion like other methods and the distances for excitation transfer can be kept small and therefore highly efficient, as the acceptor species is held inside the donor. Two recent examples demonstrate unique methods of excitation transfer. Li et al. encapsulated a rhodamine-6G photocatalyst inside a metal organic cage host, excited the host with 420 nm light, which then transferred this energy to the rhodamine-6G with up to 80% efficiency at a 10:1 acceptor:donor ratio. The excited rhodamine-6G then catalyzed C-H arylation reactions with up to 95% product yield.[85] In a separate study, Li et al. developed a host molecule termed the green box, which could encapsulate a naphthalene moiety in between two of its planar conjugated substituents, transfer an electron to the guest, and afford hydrogen production at a maximum of 34 μmol H_2/h.[86] Yet, supramolecular hosts lack the extremely specific control seen in the active sites of enzymes due to the fact that they are laboratory-made. Selectivity of substrate binding is much lesser than the extreme selectivity of the active sites of natural enzymes, and because of a relatively open binding site, the exact binding mode is difficult to characterize.[81] Most supramolecular hosts in use today bind guests on the basis of their polarity, size, or a predicted molecular interaction. If a reaction is to contain multiple similarly sized and polar molecules, the selectivity of guest binding can be presumed to be poor. Controllable binding is especially difficult if two different reactants are expected to bind within the host to then react with one another. Expected energy transfer from host molecules to bound guests can lead to multiple inefficiencies, such as energy transfer to the wrong acceptor species if a different guest than targeted binds or inefficient relaxation of excited hosts without bound guests. A covalently bound light harvester and reactive catalyst eliminates many of these issues. More targeted and energy efficient systems can be developed because of the covalent

24

tether and prior consideration in regards to energy transfer directionality. Photoactivated hosts directly catalyzing reactions or sensitizing catalytic hosts may lead to too many inefficient possible pathways.

1.3.5 Upconverting systems

Upconverting systems represent unique approaches to reactivity, as they convert the energy of two lower energy excited triplet states into one excited state at roughly double the energy. In triplet-triplet annihilation-upconversion (TTA-UC), the most common process is that two sensitizer molecules absorb photonic energy and then undergo intersystem crossing to triplet states. Then, the energy is transferred to two annihilator molecules via DET populating their triplet states. If two annihilators in their triplet states collide, they can undergo triplet-triplet annihilation returning one annihilator to the ground state and the other to a high-energy singlet state with up to double the energy of the triplet state, notwithstanding state relaxations along the way.[87] TTA-UC systems have been used to polymerize reactions and catalyze many others.[22,88] The Wenger lab has specifically utilized first row metal-centered complexes to initiate reactivity via TTA-UC, exploiting the increased penetration of low energy light into reaction mixtures while simultaneously generating high energy emissive states to initiate reactivity in a mixture. A Mo(0) homoleptic complex sensitizer exhibiting properties similar to Os(II) complexes was developed which performed TTA-UC at a quantum yield of 1.8 %, generating 430 nm light from 635 nm excitation. This process was efficient enough to initiate a $[Ru(bpy)_3]^{2+}$-catalyzed photoisomerization.[89] Following this work, the Wenger group has demonstrated similarly remarkable activity with a Cr(0) photosensitizer that performed TTA-UC at 1.8% efficiency with a 0.88 eV pseudo anti-Stokes shift that could eventually initiate a polymerization reaction of

acrylamide and with the first known Fe(III) complex to perform TTA-UC at 4% efficiency with a 0.52 eV pseudo anti-Stoke shift.[90,91]

The ability to absorb lower energy light and produce high energy excited states, and thereby catalyze high energy reactions, is powerful and desired as has been enumerated. The major drawback to TTA-UC is in its complexity and efficiency. TTA-UC systems have many steps that need to occur to afford utility. In total, to achieve high energy reactivity, two excitations, three energy transfer steps, and three collisions must occur between four molecules. TTA-UC quantum yields are ~10-20%, oftentimes lower than 10%, which is much lower in terms of photon efficiency than many of the prior described systems.[87] Along with being diffusion controlled, the triplet-triplet energy transfer steps require orbital overlap, which again has exponentially decaying distance dependence. From an energy utilization perspective, this is simply too inefficient, as photons are not inherently free. FRET requires only a donor and acceptor, and high energy reactivity can be achieved with low energy light at high efficiencies as we have demonstrated and explained herein, though much more limited than the achievable energies found in TTA-UC. So, the complexity and inefficiency of TTA-UC can be easily avoided through utilization of a bioinspired approach.

CHAPTER 2:
PROOF OF DESIGN – A BIOHYBRID STRATEGY FOR ENABLING PHOTOREDOX CATALYSIS WITH LOW-ENERGY LIGHT

2.1 INTRODUCTION

Photoredox catalysis harnesses light energy to afford potent reactivity to a broad range of chemistries and substrates that are otherwise unreactive. Upon visible excitation, the photocatalyst is transformed into a high-energy reactive intermediate that can be used to promote challenging or previously elusive transformations.[92–95] The reactivity is most often ascribed to electron- or energy-transfer from long-lived triplet metal-to-ligand charge transfer (^{3}MLCT) states that generate potent reductants or oxidants.[96,97] For example, transition metal photoredox catalysts have been used for many carbon-carbon bond formations that have been instrumental in the development of pharmaceuticals, agrochemicals, and complex natural products.[98–104] Despite their catalytic utility, the charge transfer and other reactive states are limited by small absorption bandwidths (~100 nm) and low molar absorptivities (10^3-10^4 M^{-1} cm^{-1}), resulting in poor photon conversion efficiency.[94,105–108] Additionally, most transition metal photoredox catalysts require excitation at high photon energies where the effective absorbance is often further reduced by secondary catalysts, substrates or reagents that act as optical filters. The high energy excitation can also cause cellular damage and so has limited the biological applications of this powerful technology.[109–112]

Nature overcomes the poor light-harvesting ability of the charge transfer and similar reactive states with dedicated machinery to capture sunlight for photosynthesis.[113–118] Light-harvesting proteins absorb over large spectral bandwidths (~250 nm) with high molar

absorptivities ($\sim 10^6$ M^{-1} cm^{-1}), and then efficiently transfer this energy to sensitize neighboring proteins that contain the reactive site.[116–123] Inspired by the modularity found in biology, several types of photocatalysts have been produced that employ a similar approach.[124] Nanoparticles or small molecules were covalently attached to enzymes, and electron transfer between them has been demonstrated.[125–134] However, the stringent distance dependence requirements and nonspecific reactivity of electron transfer create additional synthetic and operational challenges.[135–138] Energy transfer, which occurs over longer distances, was introduced by conjugating together transition metal photocatalysts with different excitation energies, which expanded their absorption window.[139–146] Despite the expanded absorption, the low extinction coefficients of the photocatalysts lead to light-limited activity under many conditions. The absorption range was also expanded into the low energy (near-infrared) region by direct excitation of the ^{3}MLCT state, and the utility of this scheme was demonstrated on a range of photoredox reactions.[147] However, the extremely low molar absorptivity ($\sim 10^2$ M^{-1} cm^{-1}) of this state limits its light-harvesting ability.[148–150] Upconversion of triplet states in a sensitizer/photocatalyst mixture was introduced as an alternative strategy to use near-infrared light, but with low photon conversion efficiency.[151–153] Finally, sensitization of a transition metal photoredox catalyst through energy transfer from light-harvesting ligands was demonstrated, but its impact on reactivity was not investigated.[154–156]

Here, we mimicked the design found in photosynthesis by conjugating the prototypical transition metal photocatalyst, tris(2,2′-bipyridine)ruthenium(II) ([Ru(bpy)$_3$]$^{2+}$), to the commercially-available, photosynthetic light-harvesting protein, R-phycoerythrin (RPE), from red algae (Figure 2.1). The resultant biohybrid, henceforth referred to as RPE-(Ru)$_n$, absorbed at wavelengths up to 630 nm and transferred energy from RPE to [Ru(bpy)$_3$]$^{2+}$. The energy capture provided by the light harvester enhanced catalytic yields by a factor of ten as compared to controls

that lacked light harvesting for two representative reactions, a radical thiol-ene coupling and a cysteinyl desulfurization.
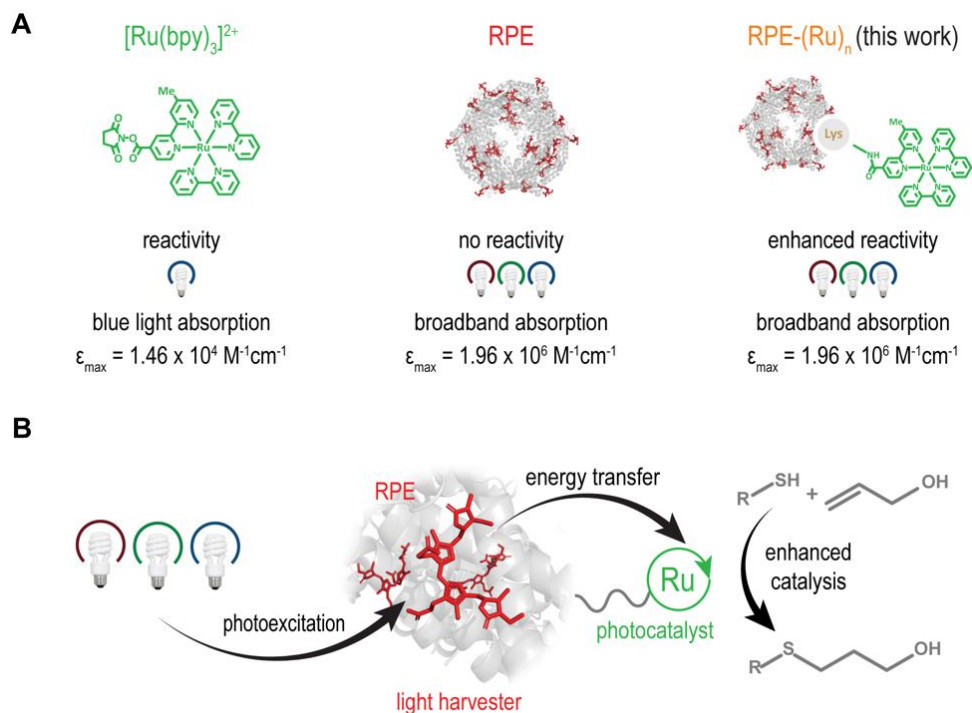
Figure 2.1: Components and concept of light-enhanced catalysis. (A) The small molecule photocatalyst, $[Ru(bpy)_3]^{2+}$ (green, left), conjugated to the photosynthetic light-harvesting protein, RPE (red, center), forms a biohybrid photocatalyst, RPE-$(Ru)_n$ (orange, right). The photocatalytic reactivity of $[Ru(bpy)_3]^{2+}$ and the light harvesting of RPE are combined in the RPE-$(Ru)_n$ biohybrid. (B) Schematic of RPE-$(Ru)_n$ photocatalysis in which photoexcitation of pigments (red, chemical structures in SI Figure S13) in RPE at any wavelength leads to energy transfer to $[Ru(bpy)_3]^{2+}$ (green), which can catalyze reactions.

2.2 RESULTS AND DISCUSSION

2.2.1 Biohybrid Synthesis and Steady-State Characterization

Synthesis of the biohybrid construct shown in Figure 2.1A, right, was accomplished by taking advantage of the 72 surface-exposed lysine residues on RPE identified using Pymol (SI Section 3A). Conjugation of $[Ru(bpy)_3]^{2+}$ to the lysine side chains occurred readily upon treatment of RPE with a derivative of $[Ru(bpy)_3]^{2+}$ substituted with an *N*-hydroxysuccinimide ester (SI Figure S2.1). While conjugation to other amino acids is possible, the lysines are the most likely

29

site due to the nucleophilicity of the amine group and their propensity for exterior positioning.[157,158] They are primarily evenly dispersed across the surface of the outer ring of the protein with two per subunit on the ends of the cylinder-like structure (SI Figure S2.10), likely leading to stochastic decoration of the exterior of RPE with $[Ru(bpy)_3]^{2+}$. The NHS-ester derivative of $[Ru(bpy)_3]^{2+}$ was chosen as the catalyst because of its commercial availability and the historical prevalence of $[Ru(bpy)_3]^{2+}$. Purification by centrifugal filtration and FPLC afforded the hybrid in high purity (SI Section 1).

Intact mass spectrometry (MS) data was obtained for both free RPE and purified RPE-$(Ru)_n$ to confirm conjugation (SI Figure S2.7). RPE is a hexameric protein in which alpha (α) and beta (β) subunits form an $(\alpha\beta)_6$ quarternary structure. The MS of RPE showed the α and β subunits at masses of 18,889 Da and 20,308 Da, respectively, both in agreement with the literature.[159] Compared to free RPE, RPE-$(Ru)_n$ exhibited modifications of 610 Da in its mass spectrum, corresponding to the molecular weight of the $[Ru(bpy)_3]^{2+}$ catalyst. The α subunit showed equally abundant peaks (1:1:1) for no modification, one modification, and two modifications. The β subunit showed unequally abundant peaks (1:1:0.2) for no modification, one modification, and two modifications, respectively. A weighted average of this data was used to estimate that ten $[Ru(bpy)_3]^{2+}$ catalysts per one RPE were retained under the MS conditions.

The absorption and emission spectra of the conjugated hybrid are overlaid with its individual components in Figure 2A. RPE-$(Ru)_n$ had an absorption spectrum similar to the free protein due to the significantly larger molar absorptivity coefficient (10^2-times) of RPE compared to $[Ru(bpy)_3]^{2+}$. The similar profile of the absorption spectra before and after conjugation also confirmed that integrity of the protein was maintained. As expected, RPE-$(Ru)_n$ showed additional absorbance in the region around the $[Ru(bpy)_3]^{2+}$ ^{1}MLCT states centered at 459 nm. Additionally,

the peak in the RPE-(Ru)$_n$ spectrum corresponding to the energy of the [Ru(bpy)$_3$]$^{2+}$ bipyridine ligand $\pi \rightarrow \pi^*$ transition (285 nm) increased in intensity relative to the free protein (SI Figure S2.8). Finally, the sum of the component spectra matched well with the spectrum of the purified RPE-(Ru)$_n$ with a 1:8 ratio, similar to the results from MS and confirming conjugation (SI Figure S2.8).

The steady state fluorescence emission spectra of free RPE and RPE-(Ru)$_n$ are also shown. The spectral profiles were essentially the same due to the much lower level of photoluminescence emission from [Ru(bpy)$_3$]$^{2+}$. The integrated fluorescence intensity decreased by ~60% for RPE-(Ru)$_n$ compared to RPE, providing further evidence of successful conjugation and indicating the presence of energy transfer.
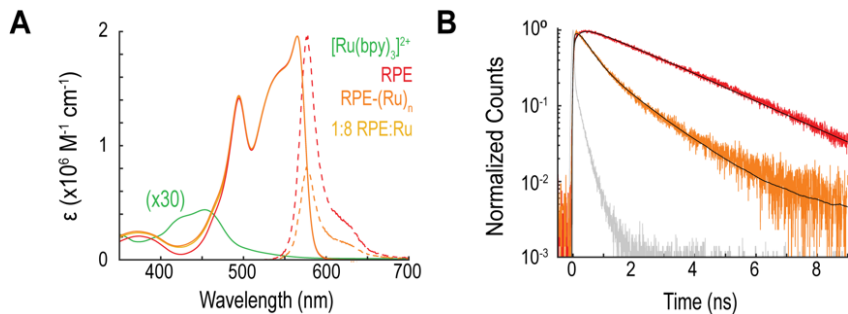
Figure 2.2: Steady-state absorption and time resolved fluorescence. (A) Absorption spectra of [Ru(bpy)$_3$]$^{2+}$, RPE, a mixture of RPE: [Ru(bpy)$_3$]$^{2+}$ in a 1:8 molar ratio, and RPE-(Ru)$_n$ with the relative fluorescence emission spectra of RPE and RPE-(Ru)$_n$. (B) Nanosecond fluorescence decays of RPE and RPE-(Ru)$_n$ with the IRF (gray).

2.2.2 Characterization of the Excited-State Dynamics

Time-resolved spectroscopy was used to characterize the photophysics of the biohybrid. The fluorescence lifetime was measured for both the free protein and biohybrid structure. The RPE fluorescence emission (Figure 2.2B) showed a monoexponential decay with a timescale of 2.63 ns, in agreement with literature values of 2.3-3.1 ns.[119,120] In contrast, the RPE-(Ru)$_n$ emission showed a multi-exponential decay profile, which was best fit with a tri-exponential function. The

two fast timescales were ~0.039 ns and ~0.368 ns, each with an amplitude of ~40%. The slower timescale was 1.70 ns. The average lifetime was 0.384 ns, which gave an overall energy transfer efficiency of 85%. The fitting parameters for all samples are summarized in SI Tables S2.2 and S2.3.As discussed above, although each RPE-$(Ru)_n$ contains on average ten $[Ru(bpy)_3]^{2+}$, the sample is a heterogeneous mixture with $[Ru(bpy)_3]^{2+}$ attached to RPE in a variety of stoichiometries and conjugation sites. We assign the two fast timescales to uphill energy transfer from RPE to $[Ru(bpy)_3]^{2+}$ in RPE-$(Ru)_n$ with a large number of conjugated $[Ru(bpy)_3]^{2+}$ and/or $[Ru(bpy)_3]^{2+}$ well-positioned for energy transfer. Consistent with this assignment, the timescale of energy transfer for RPE-$(Ru)_n$ with ten $[Ru(bpy)_3]^{2+}$ was calculated to be 0.409 ns using Förster theory (SI Section 3). These calculations also predict an 78% energy transfer efficiency, close to the experimental value. Förster energy transfer is governed by the spectral overlap and distance between the donor and acceptor. Due to the small spectral overlap, each energy transfer pathway is inefficient. However, they give an overall high energy transfer efficiency from the combined contributions of the ten energy transfer pathways from RPE to $[Ru(bpy)_3]^{2+}$ (SI Section 3B). Despite the uphill nature of the energy transfer step, rapid trapping of the excitation by intersystem crossing on $[Ru(bpy)_3]^{2+}$ likely limited back transfer. We assign the slow timescale to energy transfer in the small population of RPE-$(Ru)_n$ only bearing conjugated $[Ru(bpy)_3]^{2+}$ that are poorly positioned for energy transfer.

Transient absorption (TA) spectroscopy was used to monitor the excited-state dynamics, including transitions into non-emissive states. To probe the photophysical pathways with high temporal resolution, ultrafast TA measurements were performed on both RPE and RPE-$(Ru)_n$ with excitation at 540 nm, which overlaps with the RPE absorption peak. For free RPE (Figure 2.3A, left), initial excitation gave rise to a ground state bleach (GSB)/stimulated emission (SE) signal

across the absorption spectrum. As shown in Figure 2.3B, the GSB/SE signal at the low-energy state of RPE decayed on 54 ps and 2.2 ns (1.56 ns average) timescales, similar to previously observed values.[119] For RPE-(Ru)n (Figure 2.3A, right), the GSB/SE signal decayed more quickly across the spectrum, likely as a result of energy transfer to $[Ru(bpy)_3]^{2+}$. As shown in Figure 2.3B, the signal at the low energy state decayed on 36 ps and 170 ps (137 ps average lifetime) timescales, consistent with the fluorescence lifetime measurements and calculations of the energy transfer timescale from RPE to $[Ru(bpy)_3]^{2+}$.

To more directly probe $[Ru(bpy)_3]^{2+}$ sensitization upon RPE excitation, we employed nanosecond TA spectroscopy on RPE-(Ru)n, $[Ru(bpy)_3]^{2+}$, and an unconjugated mixture of RPE and $[Ru(bpy)_3]^{2+}$. The prompt transient spectra are shown for all three samples in Figure 2.3C. For $[Ru(bpy)_3]^{2+}$ excited at 450 nm, the characteristic GSB at 450 nm and ESA at 380 nm were observed, consistent with previous reports.[160] For the unconjugated mixture, after excitation of RPE at 540 nm, a component of the RPE GSB/SE persisted while spectral features of excited $[Ru(bpy)_3]^{2+}$ were absent. For the RPE-(Ru)n conjugate, a similar GSB/SE component was present in the RPE spectral region, but the spectral features of $[Ru(bpy)_3]^{2+}$ also appeared, signaling successful energy transfer to the photocatalyst. Excitation further toward the red, at 580 nm, also demonstrated energy transfer to the photocatalyst (SI Figure S2.22). Energy transfer is expected to populate the charge transfer bands of $[Ru(bpy)_3]^{2+}$ almost exclusively for excitation wavelengths above 500 nm, as the catalytically deleterious triplet metal centered state is higher in energy.[146,161] Although these experiments provide spectral evidence that energy transfer occurs, the signals of energy transfer appear within the 8 ns instrument response function, so the timescale of energy transfer cannot be discerned from this experiment (SI Section 4C). These results do, however, provide direct experimental evidence of the assignment to energy transfer, as electron transfer

would have resulted in the spectra of the oxidized or reduced form of $[Ru(bpy)_3]^{2+}$ in the RPE-$(Ru)_n$ sample.[135]
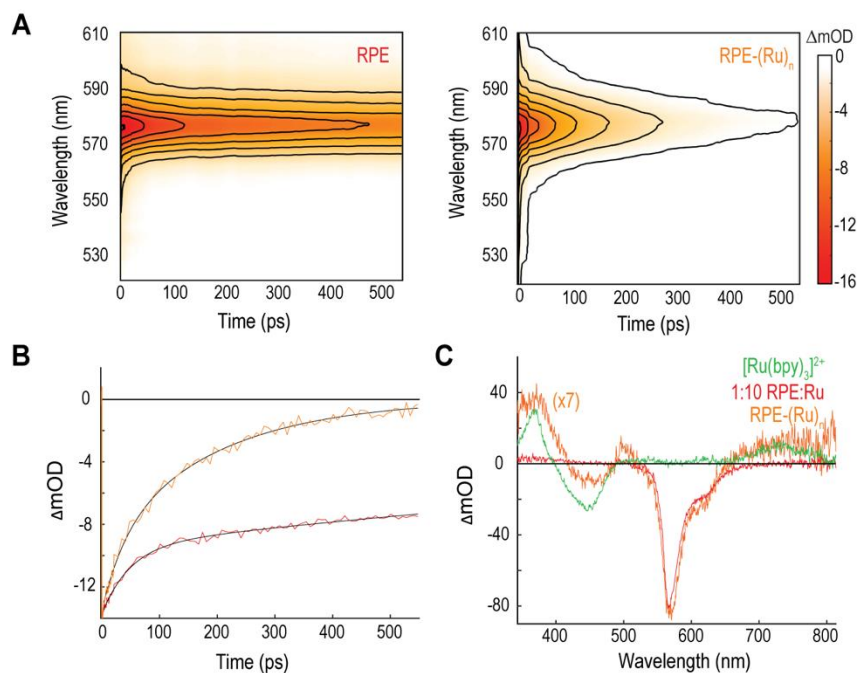
Figure 2.3: Transient absorption of RPE-Ru biohybrid. (A) Ultrafast transient absorption spectra of RPE (left) and RPE-$(Ru)_n$ (right). The ground state bleach shows a faster decrease for the hybrid as compared to the free protein. (B) Kinetic traces of both samples at 570 nm. (C) Nanosecond transient absorption spectra of $[Ru(bpy)_3]^{2+}$, RPE-$(Ru)_n$, and a mixture of RPE and Ru.

2.2.3 Demonstration of Enhanced Catalysis Using the Biohybrid

To establish the catalytic ability of RPE-$(Ru)_n$, we assessed product yields for two radical initiation reactions previously reported in literature, a thiol-ene coupling and a cysteinyl desulfurization.[162,163] The goal of this proof-of-concept study is to identify an enhancement in catalytic performance and, for radical chain reactions, differences in the photodriven initiator formation can be easily observed in the final product yields. While the sequential nature of the propagation means that the improvement in the photodriven process cannot be straightforwardly quantified, these reactions allow for clear qualitative comparison of yields. Performance in the presence of RPE-$(Ru)_n$ was compared to $[Ru(bpy)_3]^{2+}$, RPE, and an unconjugated mixture of RPE

and $[Ru(bpy)_3]^{2+}$ as controls at three LED wavelengths (blue, 459 nm; green, 513 nm; red, 630 nm). Full experimental details, including all yields, substrates, and product NMR characterization are included in the SI Sections 5 and 6.

We first investigated the effectiveness of RPE-$(Ru)_n$ in the thiol-ene reaction, a widely adopted bioconjugation strategy extended to photoredox catalysis by Yoon and co-workers.[162,164,165] Relative to small molecule $[Ru(bpy)_3]^{2+}$, coupling of glutathione (**1**) and allyl alcohol (**3**) under RPE-$(Ru)_n$ catalysis presented improved yields under red, green, and blue light irradiation (Figure 2.4, SI Section 5). Most notably, RPE-$(Ru)_n$ afforded product **2** in 89% yield under red light irradiation, whereas no product formation was observed with $[Ru(bpy)_3]^{2+}$. Under green irradiation, which corresponds to the maximum of the RPE absorbance, **2** was generated in ~10% yield with $[Ru(bpy)_3]^{2+}$ alone and with the unconjugated $[Ru(bpy)_3]^{2+}$ and RPE mixture. By contrast, RPE-$(Ru)_n$ catalyzed the reaction in 70% yield. The yields with RPE-$(Ru)_n$ under both green and red irradiation were higher than the yield with $[Ru(bpy)_3]^{2+}$ alone under blue irradiation at the maximum of its absorbance (10%, in agreement with previous literature reports[165]). To demonstrate the generality of the observed enhancement, four additional substrates (**4-7**) were evaluated. In all cases, product yields under green or red irradiation surpassed yields achieved by $[Ru(bpy)_3]^{2+}$ alone or by the unconjugated $[Ru(bpy)_3]^{2+}$/RPE mixture, even reaching quantitative yields for glycosylation (**7**). The ability to catalyze the reaction at red wavelengths is afforded by uphill energy transfer utilizing thermal energy to account for differences in activation energy (SI Section 3C).[166,167] Furthermore, both product yields and photostability of RPE-$(Ru)_n$ increased under low irradiance, indicating that optimal operation may require the photon absorption rate to be empirically matched to the catalytic cycle. These results demonstrate the ability of RPE-$(Ru)_n$ to improve catalytic performance and enable operation under irradiation at any visible wavelength.
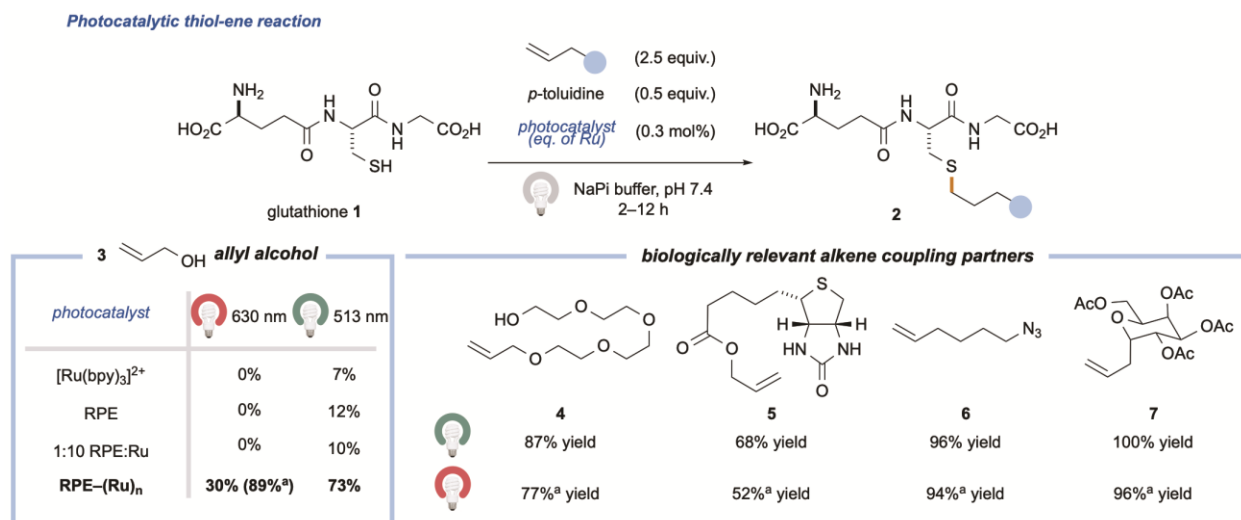
Figure 2.4. Photocatalytic radical thiol-ene reaction. RPE-(Ru)$_n$ enables or enhances yields at red and green wavelengths. Reaction times are 2 h except where denoted. [a]12 h reaction time. Note: "eq. of Ru" refers to the fact that all reactions were performed with catalyst loadings normalized to [Ru(bpy)$_3$]$^{2+}$.

To determine the versatility of our RPE-(Ru)$_n$, we also investigated its performance in a cysteinyl desulfurization method developed by Guo and co-workers in 2016.[163] The original reaction, which employs 5 mol% of [Ru(bpy)$_3$]$^{2+}$, converted glutathione (**1**) to product **8** with 85% yield under blue light irradiation. With our RPE-(Ru)$_n$ biohybrid, the desulfurization proceeds with similarly high efficiencies under red or green light irradiation (78% and 100%, respectively) using 0.3 mol% of the catalyst. Notably, control reactions with [Ru(bpy)$_3$]$^{2+}$, RPE, or the unconjugated mixture of the two species showed no reactivity across both irradiation wavelengths (Figure 2.5). The reduced catalyst loading of 0.3 mol% under conditions relevant to this manuscript compared to the previously reported value of 5 mol% also demonstrates the synthetic competency of the biohybrid.[163] Furthermore, the large RPE appendage with a mass of 240 kDa allowed for facile catalyst recovery through centrifugal filtration with a 50 kDa MWCO filter. Biohybrid reusability was screened by resubjecting RPE-(Ru)$_n$ to fresh reagents, affording 83% yield under green light irradiation and 65% yield under red light irradiation. Thus, along with improvements to product

yields, the biohybrid serves as a homogeneous catalyst with the key reusability advantage of heterogeneous catalysis.[168,169]

photocatalyst	630 nm [a]	513 nm [b]	459 nm [b]
$[Ru(bpy)_3]^{2+}$	0%	0%	85% [c]
RPE	0%	0%	–
1:10 RPE:Ru	0%	0%	–
RPE–(Ru)$_n$	**78%**	**100%**	–
RPE–(Ru)$_n$ reuse	**65%**	**83%**	–
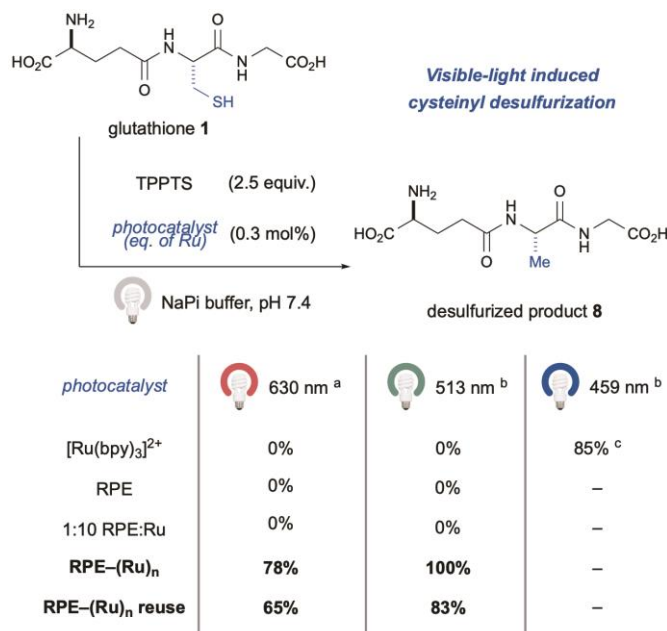
Figure 2.5. **Visible-light induced cysteinyl desulfurization.** [a]36 h irradiation, [b]12 h irradiation, [c]Literature-reported yield.[163] TPPTS: 3,3′,3″-phosphanetriyltris trisodium salt.

2.3 CONCLUSION

A biohybrid catalyst consisting of the photosynthetic light-harvesting protein RPE and multiple conjugated $[Ru(bpy)_3]^{2+}$ photocatalysts has been synthesized, characterized, and shown to improve catalytic efficiency. Energy transfer from RPE to $[Ru(bpy)_3]^{2+}$ improved yields and enabled reactivity even at red wavelengths. The biohybrid photocatalyst is also environmentally sustainable as it operates in aqueous conditions, exhibits activity under low-energy irradiation, and is easily reused. These initial demonstrations lay the groundwork for the development of photocatalysts with distinct light harvesting and reactive components as seen in photosynthesis, which, as illustrated here, allows robust and reliable reactivity.

2.4 EXPERIMENTAL PROCEDURES

2.4.1 Sample Preparation

R-phycoerythrin (RPE; Agilent, Cat. No. PB-32) was dialyzed against phosphate buffer (0.1 M sodium phosphate, pH = 7.5, filter sterilized and degassed) and refrigerated until needed. Bis(2,2′-bipyridine)-4′-methyl-4-carboxybipyridine-ruthenium (II) N-succinimidyl ester bis(hexafluorophosphate) ([Ru(bpy)$_3$]$^{2+}$-NHS ester, Sigma-Aldrich Cat. No. 96631) and dimethyl sulfoxide (DMSO) were used as received. Bioconjugation of the [Ru(bpy)$_3$]$^{2+}$-NHS ester to RPE was performed by reacting R-phycoerythrin (250 µL of 1 mg/mL in phosphate buffer) with [Ru(bpy)$_3$]$^{2+}$-NHS ester (50 µL of 20 mg/mL in DMSO, ~950x molar excess of catalyst).[170] Multiple small-scale (300 µL) reactions were performed in parallel to allow [Ru(bpy)$_3$]$^{2+}$-NHS ester to easily mix with phycobiliproteins without hydrolysis of the NHS ester. The reaction mixtures were placed on an incubator shaker (1100 RPM) at room temperature for 1 h. After incubation, the small-scale reaction mixtures were combined, placed into a 50 kDa molecular weight cut-off centrifugal filter (Millipore, Cat. No. UFC9050) and centrifuged at 4° and 4000 rpm (3220 rcf) for 15-20 min. Further purification was performed using fast protein liquid chromatography (FPLC) with a NGC chromatography system (Bio-Rad) on a Superose® 6 10/300 GL column (Cytiva Life Sciences) at a flow rate of 0.5-0.75 mL/min at 4° in phosphate buffer. Fractions of the peak eluting at 16.2 mL for RPE were collected and centrifuge concentrated using the same parameters as described above. All reactions and spectroscopic studies were performed in phosphate buffer (0.1 M sodium phosphate, pH = 7.5, filter sterilized and degassed). Further details on conjugation and purification are provided in the SI section 1.

2.4.2 Steady-state Absorption and Fluorescence Measurements

Linear absorbance spectra were acquired using a Shimadzu UV-2401PC spectrophotometer. Fluorescence emission spectra were obtained using a Varian Cary Eclipse with 565 nm excitation at the maximum absorbance of RPE.

2.4.3 Fluorescence Lifetime Measurements

Fluorescence lifetime measurements were performed using a supercontinuum generated in a nonlinear photonic crystal fiber (FemtoWhite 800, NKT photonics) pumped by a Ti:sapphire oscillation (Mai Tai, Spectra Physics). Full details on the laser setup are in the SI Section 4. The excitation wavelength was selected using a 550 nm, 15 nm FWHM bandpass filter (Chroma Technology Corp ET550/15x) and the emission wavelength was selected using a 580 nm, 10 nm FWHM bandpass filter (Thor Labs FB580-10). The excitation laser pulse was focused on a 1 cm x 2 mm pathlength quartz cuvette (Hellma Analytics 108.002F-QS) to a spot size of 0.66 μm^2 and with a pulse energy of 0.027 nJ per pulse. The instrument response function (IRF) was measured using a scatter solution containing a 1:100 v:v mixture of HS-40 colloidal silica (Sigma-Aldrich) and phosphate buffer with a width of 75-95 ps (FWHM). Fluorescence lifetime decay curves were individually fitted to a mono- or tri-exponential function using iterative reconvolution with the IRF.

2.4.4 Intact Mass Spectrometry (Intact MS)

RPE and RPE-(Ru)$_n$ were loaded onto a Thermo MAbPac RP column using an Agilent1100 HPLC system. Further details on chromatography elution parameters can be found in SI Section 2A. MS data was acquired in profile mode with a Thermo QE mass spectrometer at 17,000 resolution, and analyzed using ThermoBioPharma Finder[TM] 3.2 ReSpect with default settings.

2.4.5 Transient Absorption (TA) Studies

Femtosecond transient absorption studies were conducted using a broadband white light source, the complete details of which are described in SI Section 4B. Briefly, pulses were obtained using the output of a Ti:sapphire regenerative amplifier (Coherent Libra, 5 kHz, 1.1 mJ, 40 fs pulse, λ_c=800 nm). White light was generated using an argon gas chamber (20 psi) and filtered for a center wavelength of 540 nm. Spectra were collected by measuring the probe laser for each pulse using a line CCD (e2v) and chopping the pump laser at 2.5 kHz.[171] Samples were prepared at an OD of 0.3 in a 1 mm path cuvette, flowed with a peristaltic pump to prevent photodegradation and re-excitation, and chilled to 8° C throughout the measurement. Linear absorption spectra were collected before and after TA to confirm sample integrity was retained.

Nanosecond transient absorption spectra were acquired on an Edinburgh Instruments LP 920 spectrometer outfitted with a liquid nitrogen equipped temperature controller (Unisoku CoolSpeK). Samples were excited using the output of a tunable OPO (Opotek Vibrant 355) operating at 1 Hz. The excitation source was kept to less than 2.5 mJ/pulse ($\sim$5 mJ/cm^2). The probe source of the LP 920 (a xenon arc lamp) was also filtered through two long-pass filters (290 nm and 320 nm) to prevent the UV component of the probe light from degrading the sample. Samples were prepared in quartz 1 cm cuvettes with aqueous phosphate buffer solutions, stirred, and kept at 8 °C for the duration of the experiment. To capture the transient absorption signals for the bound ruthenium chromophores, which have small excited-state-induced changes in molar absorptivity relative to the protein, sample absorbances of 0.6-0.9 at 565 nm were used. The pulse duration was 8 ns (see note in final paragraph of SI Section 4C).

2.4.6 Synthetic Reactions

Thiol-ene coupling[162] and cysteinyl desulfurization[163] reactions were performed as described in the literature, with modifications due to the requirements of RPE-(Ru)$_n$. The reactions were performed in phosphate buffer, at the reduced scale dictated by the protein, without agitation to prevent aggregation, and with reduced light intensity due to the greater absorbance of the protein. Reactions were replicated and screened at three LED illuminations (blue, green, red) for the $[Ru(bpy)_3]^{2+}$, RPE, RPE-(Ru)$_n$, and an unconjugated mixture of the two components, and examined for enhanced yields using ^{1}H NMR against an external standard. Quantum yield measurements were performed on both test reactions using ferrioxalate actinometry. We also screened RPE-(Ru)$_n$ reusability after recovery via size-exclusion centrifugal filtration. Full experimental details are described in the SI Sections 5 and 6.

2.5 SUPPLEMENTARY INFORMATION
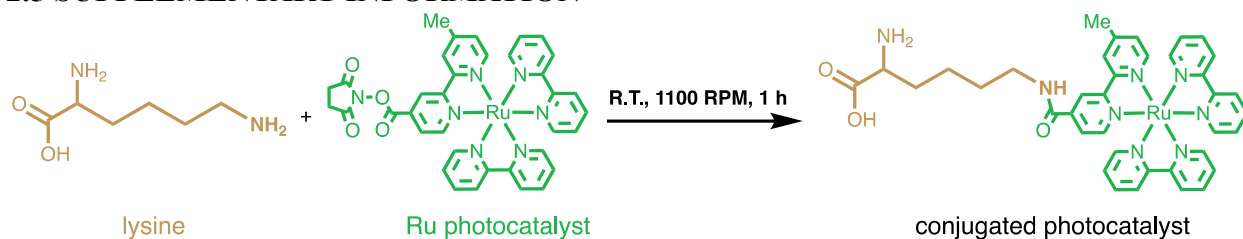
Figure S2.3: Conjugation Strategy Conjugation of NHS ester Ru(bpy)$_3$ (green) to the lysine residues (gold) of a phycobiliprotein.

1. **Construction and Purification of RPE-(Ru)$_n$**

   Purchased RPE was placed in 3.5 kDa dialysis tubing against several (4-6) changes of phosphate buffer over the course of 2-3 days and stored in a 4 °C refrigerator until needed. Purchased NHS ester Ru(bpy)$_3$ was stored at -20 °C and used within one month to prevent NHS ester hydrolysis. Figure S2.1 illustrates the conjugation reaction components and conditions. Purification of the biohybrid photocatalysts was performed using fast protein liquid chromatography (FPLC) and centrifugation (described in the main text and below). Characterization of successful conjugation was performed using intact mass spectrometry and linear absorption measurements (ESI Section 2), and characterization of energy transfer was performed using fluorescence lifetime measurements and transient absorption spectroscopies (ESI Section 4).
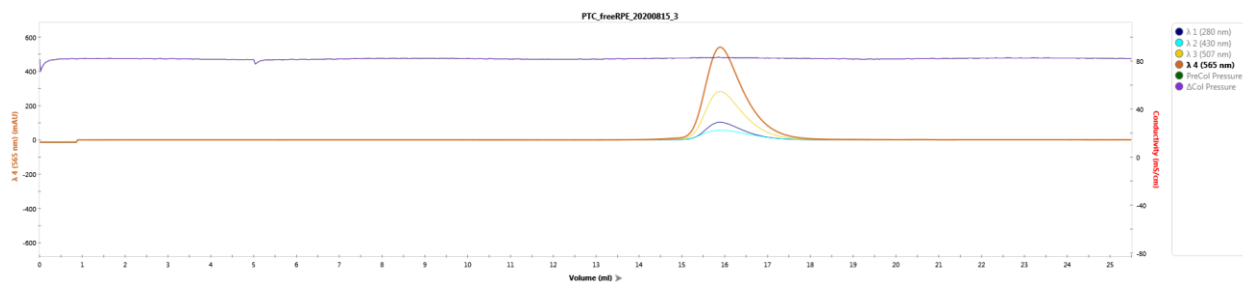
Figure S2.2: RPE chromatograph. FPLC chromatograph of RPE, exhibiting a single eluted peak at 15.9 mL on average.
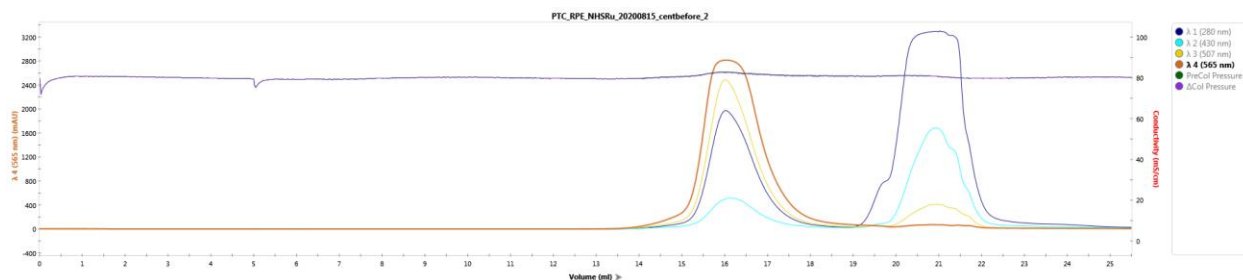
Figure S2.3: RPE-(Ru)ₙ chromatograph. FPLC chromatograph of RPE-(Ru)$_n$, exhibiting elution of the biohybrid at 16.2 mL on average, and excess NHS ester Ru(bpy)$_3$ elution beginning at 20 mL.

FPLC was performed using a 250 μL sample inject line. Four-wavelength (280, 430, 507, 565 nm) UV-visible absorption detection identified product peaks, with 565 nm as the RPE diagnostic absorption. Free RPE eluted at 15.9 mL (Figure S2). For RPE-(Ru)$_n$, two bands, one pink (signifying RPE) and one yellow (signifying [Ru(bpy)$_3$]$^{2+}$), were visible on the column itself. Fractions eluting at 16.2 mL (Figure S2.3) were collected and centrifuge concentrated using the parameters described in the main text. The biohybrid eluted at very similar volume to RPE because of their small mass difference (each conjugated [Ru(bpy)$_3$]$^{2+}$ constitutes only 0.25% the protein weight). The second peak in the biohybrid chromatogram, eluting at 20 mL (λ_{max}=280 nm), consisted of excess unreacted NHS ester Ru(bpy)$_3$ (Figure S2.3). The NHS ester Ru(bpy)$_3$ peak was broad and frequently saturated the detector, a result of the large molar excess of free catalyst.

A. Stability Experiments on RPE-(Ru)ₙ and RPE

Optimal light and agitation conditions for RPE-(Ru)$_n$ in screening reactions were found by monitoring the UV-visible absorption spectrum of RPE-(Ru)$_n$ over time.[172] We tested four green LED light conditions: no light (dark), bench light, minimum LED intensity (minLED), and maximum LED intensity (maxLED). We observed protein aggregation upon stirring, so we did not agitate the sample. RPE-(Ru)$_n$ remained in the cuvette throughout the experiment, and UV-vis absorption spectra were obtained at 0 h

(before any irradiation), 1 h, 2 h, 3 h, 4 h, 5 h, 6 h, 9 h, 12 h, and 24 h. We tested one red and one blue LED condition (minLED) and spectra were obtained at 0 h (before any irradiation), 3 h, 6 h, 9 h, and 24 h. We also performed a control experiment on free RPE under the same green light conditions and on $[Ru(bpy)_3]^{2+}$ at 0 h (before any irradiation), 3 h, 6 h, 9 h, and 24 h.

We performed spectral decomposition to analyze the photodegradation and scattering components of RPE and RPE-$(Ru)_n$ for each time point. Briefly, each spectrum could be fit by the equation below:

$$A_{RPE-Ru}(\lambda) = X\left(A_{RPE-Ru_{0h}}(\lambda)\right) + \log_{10}\frac{1}{1 - C\lambda^{-1}} + \log_{10}\frac{1}{1 - D\lambda^{-4}}$$

where the first term represents the amount of photodegradation and the second two terms represent the amount of scattering.[173] A_{RPE-Ru} is the absorption at t>0 h, A_{RPE-Ru_0h} is the initial spectrum, X represents the fraction of the initial spectrum present at t>0 h, and C and D are constants used to capture the scattering component. The fitted values at 565 nm, the maximum RPE absorption, for the photodegradation and scattering components were separately used to calculate the percent composition of the spectrum at each point in time. The results show that the most stable reaction conditions for RPE and RPE-$(Ru)_n$ are minimum LED light without stirring. The same experiments repeated in the presence of the starting material for our test reactions, glutathione, showed no appreciable difference.
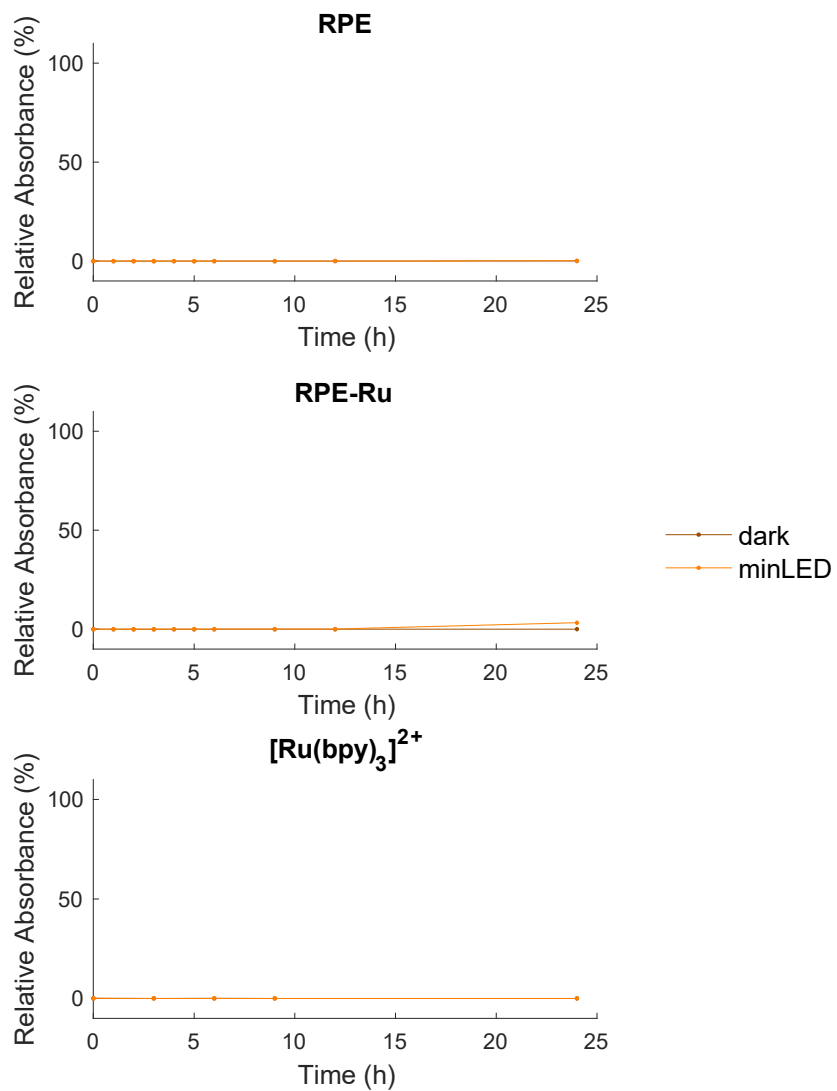
Figure S2.4: Scattering component of RPE, RPE-(Ru)$_n$, and [Ru(bpy)$_3$]$^{2+}$. The percent absorbance of the fitted scattering component in RPE, RPE-(Ru)$_n$, and [Ru(bpy)$_3$]$^{2+}$.
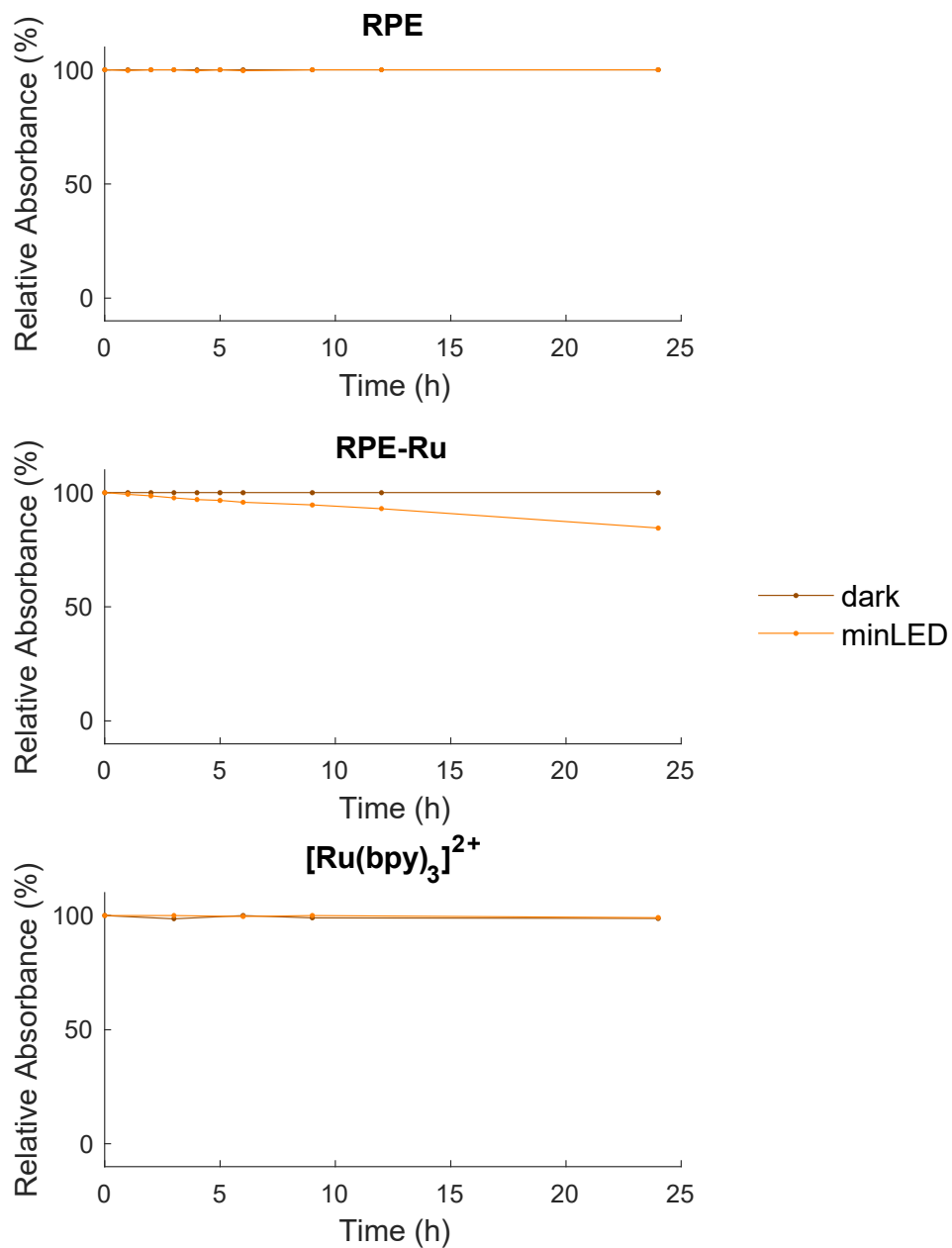
Figure S2.5: Photodegradation component of RPE, RPE-(Ru)ₙ, and [Ru(bpy)₃]²⁺. The percent absorbance of the fitted photodegradation component in RPE, RPE-(Ru)ₙ, and [Ru(bpy)₃]²⁺.
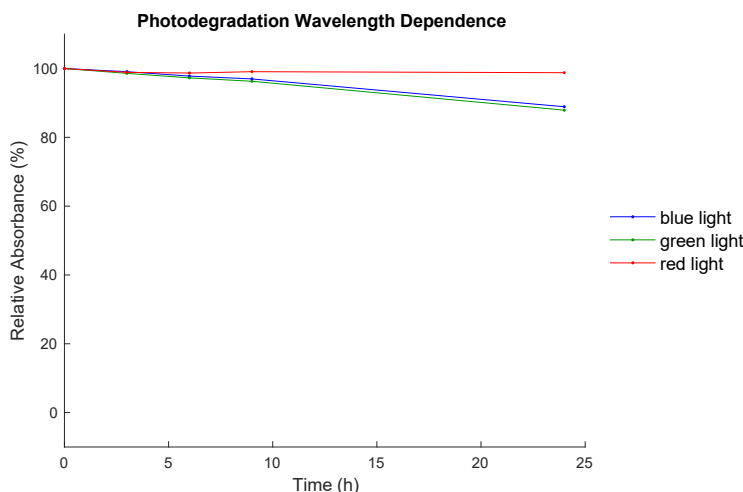
Figure S2.6: Excitation wavelength dependence of RPE-Ru stability. The percent absorbance of the fitted photodegradation component under blue, green, and red irradiance.

2. Determination of Successful Conjugation

A. Intact Mass Spectrometry

LC/MS Analysis: 10 pmol of protein was loaded onto a Thermo MAbPac RP column (1 mm x 100 mm) using an Agilent1100 HPLC system with Buffer A: water + 0.1% formic acid and Buffer B: acetonitrile + 1% formic acid. The flow rate was 100 μL/min throughout the LC gradient. The proteins (RPE and RPE-(Ru)$_n$, respectively) were loaded at 10% B, after which the gradient increased to 20% B for 1 min, to 45% for 14 min, to 90% for 1 min and was held at 90% for 4 min after which the column was re-equilibrated at 10% B.

The data was acquired in profile mode with a Thermo QE mass spectrometer at 17,000 resolution, scanning from m/z 600-4000, AGC target was set at 3 x 10^6, Maximum IT at 200 ms and microscans at 5. The data was analyzed by ThermoBioPharma Finder^{TM} 3.2 ReSpect with default settings. RPE-(Ru)$_n$ (Figure S2.7, top) is shown with the free RPE mass spectra (Figure S2.7, bottom).
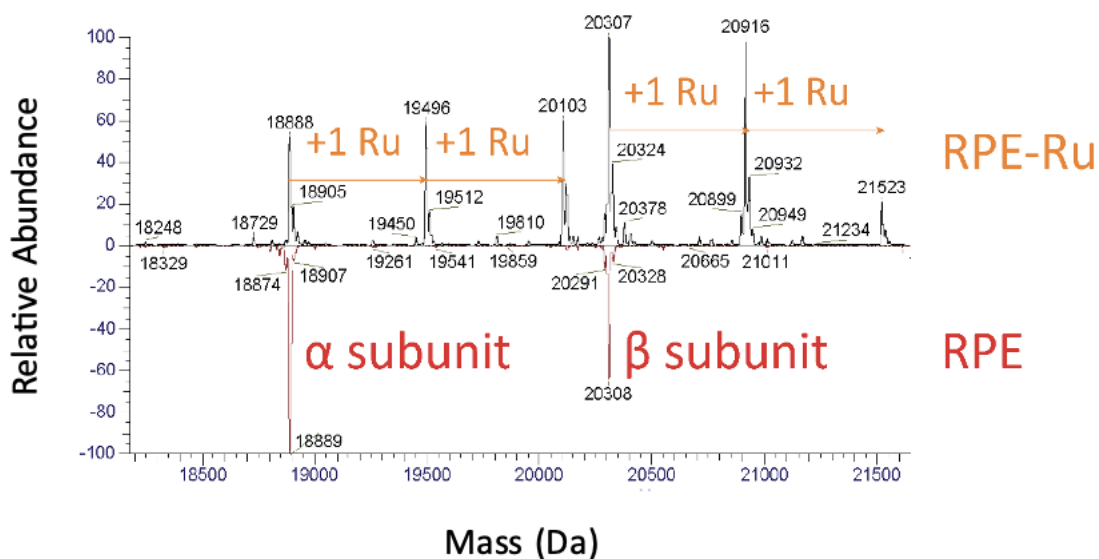
Figure S2.7: Intact MS of RPE and RPE-(Ru)$_n$. Intact MS spectra of free RPE (bottom) and the RPE-(Ru)$_n$ biohybrid (top).

B. UV-Visible Absorption and Steady State Fluorescence Experiments

Linear absorbance spectra were acquired using a Shimadzu UV-2401PC spectrophotometer. Fluorescence emission spectra were obtained using a Varian Cary Eclipse with excitation determined by R-phycoerythrin (565 nm). All spectra were acquired at room temperature in phosphate buffer. Spectra were acquired using a 1 cm x 2 mm path length quartz cuvette (Hellma Analytics 108.002F-QS).

The linear absorbance spectra were normalized to uniform concentration by using the maximum absorbance and molar absorptivity of RPE. After scaling, linear decomposition was obtained using the equation below:

$$A_{RPE-Ru} = A_{RPE} + X(A_{Ru})$$

with A_{RPE-Ru} the absorption spectrum of RPE-(Ru)$_n$, A_{RPE} the absorption spectrum of RPE, A_{Ru} the absorption spectrum of $[Ru(bpy)_3](PF_6)_2$, and X the fitted molar equivalents of $[Ru(bpy)_3]^{2+}$ per RPE. The individual component absorption spectra, biohybrid absorption

spectrum, and fitted spectrum (black line) is shown in Figure S2.8. The X value (X=8 here) matches well with the predicted equivalents from Intact MS.

Fluorescence emission spectra (λ_{em}=578 nm) of the phycobiliprotein was used to determine the FRET overlap integral, described further in ESI Section 3. 2.5 nm excitation and emission slit widths were used in obtaining emission spectra. The integrated fluorescence intensity of RPE and RPE-(Ru)$_n$ also provided initial evidence of energy transfer, as described in the main text and shown in Figure S2.9 below.
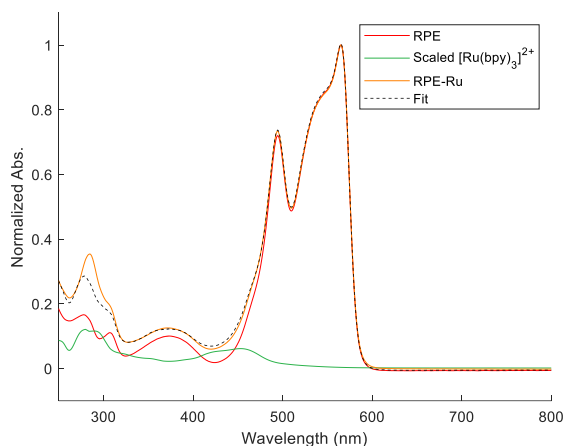
Figure S2.8: Simple sum absorption spectra of biohybrid components. Linear absorbance of RPE-(Ru)$_n$ and its individual components, with a linear sum of the components shown in black.
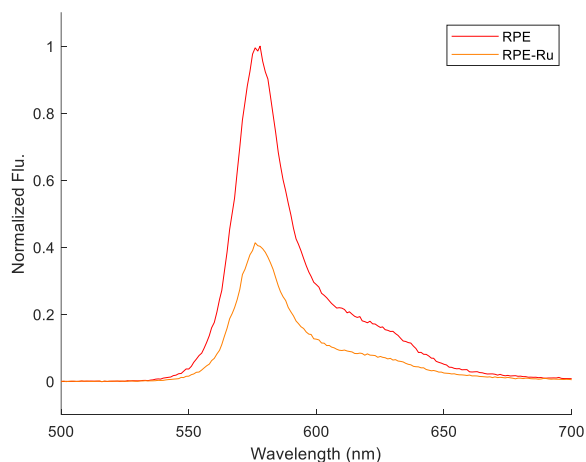
Figure S2.9: Steady-state fluorescence of RPE and RPE-(Ru)$_n$. The integrated steady-state fluorescence intensity of RPE-(Ru)$_n$ is 57% less than free RPE.

3. FRET Calculations

A. Determination of Number of Surface-Accessible Lysines and Relevant Distances

The number of surface accessible lysine residues within 2.5 Å^2 for RPE from *Agarophyton chilense* (PDB: 1EYX)[174] was identified using the open source findSurfaceResidues in Pymol. A total of 72 accessible lysine residues on RPE were found and are shown in Figure S2.10. Centroid to centroid distances for the emitting four inner phycoerythrobilin (PEB) pigments and 24 accessible lysine residues present in an $(\alpha\beta)_2$ dimer were also determined (Figure S2.11, Table S2.1). The γ-subunit of RPE was not considered because it is buried within the $(\alpha\beta)_6$ hexamer structure.[175]

Pigment-$[Ru(bpy)_3]^{2+}$ distances were determined by adding the pigment-lysine distances determined above to the lysine-$[Ru(bpy)_3]^{2+}$ distance, calculated using ChemDraw3D (Figure S2.12). We chose to use the theoretically most stretched conformation of the lysine side chain to obtain a lower limit to FRET calculations. This structure was energy minimized using the internal MM2 function, and the lysine-$[Ru(bpy)_3]^{2+}$ distance was found to be 12.4 Å.

RPE Distances - pigments to lysine residues

$(\alpha\beta)_2$ has 24 lysine residues and 4 inner PEB pigments

Lys/Pigment	1	2	3	4
1	11.8	5.0	12.2	5.0
2	20.0	8.2	20.2	8.1
3	27.8	15.8	27.9	15.4
4	30.9	16.7	31.0	16.6
5	32.8	18.6	32.7	18.3
6	33.5	20.5	33.6	20.4
7	34.8	25.1	34.5	25.2
8	39.3	25.9	39.4	25.9
9	39.7	32.0	40.2	31.3
10	40.9	39.5	40.9	39.6
11	42.4	40.3	41.9	40.2
12	43.8	42.3	43.9	42.4
13	44.1	44.1	44.2	44.6
14	46.6	44.8	46.7	44.7
15	50.4	45.3	50.2	45.9
16	50.6	49.4	50.5	49.2
17	50.6	60.5	50.8	60.3
18	52.0	60.5	51.8	60.6
19	55.3	62.4	55.0	62.4
20	56.5	70.8	56.6	70.7
21	58.9	71.7	58.9	71.9
22	59.6	72.6	60.2	72.7
23	61.9	74.9	62.0	74.8
24	64.1	79.1	64.4	79.8

Table S2.1: Tabulated pigment to lysine distances of RPE. Pigment to lysine residue distances listed in order of increasing distance in units of Angstroms.
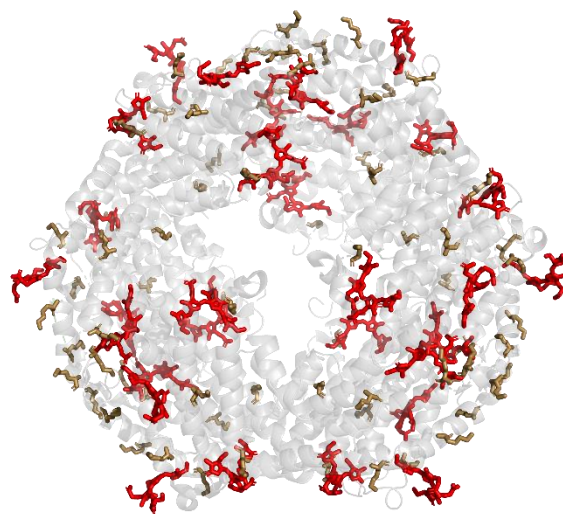
Figure S2.10: RPE exterior lysine residues. Pymol calculations reveal 72 surface accessible residues (gold) present on RPE. Pigments are highlighted in red.
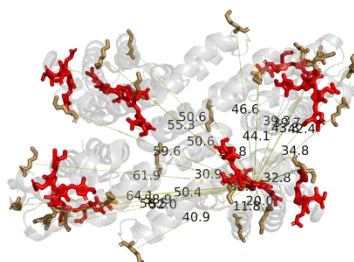
Figure S2.11: RPE pigment to lysine distances. Pymol calculations are used to find the RPE inner PEB pigment to lysine centroid to centroid distances for FRET calculations.
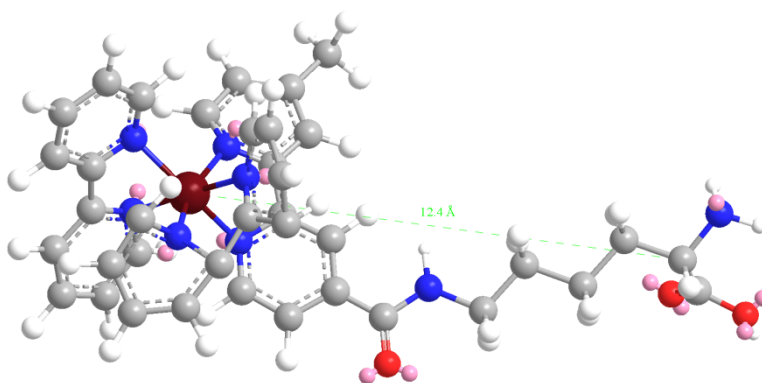
Figure S2.12: Lysine to [Ru(bpy)$_3$]$^{2+}$ distance. Lysine (left) to [Ru(bpy)$_3$]$^{2+}$ (right) linker distance calculated using the MM2 minimized structure given by ChemDraw3D.
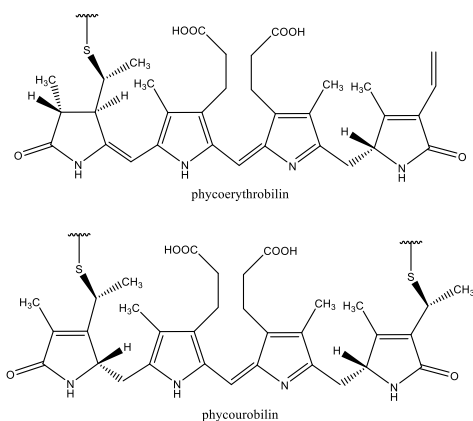
Figure S2.13: Pigments covalently bound in protein of RPE. Phycoerythrobilin, the 530 nm and 565 nm absorbing pigment (top), and phycourobilin, the 495 nm absorbing pigment (bottom).

B. FRET Rate Calculations:

We performed Förster Resonance Energy Transfer (FRET) calculations to estimate the energy transfer rate between RPE pigments and $[Ru(bpy)_3]^{2+}$.[44] Here, the pigments of the protein represent the donor, D, and the $[Ru(bpy)_3]^{2+}$ represents the acceptor, A. FRET is the non-emissive excitation of A by an excited D, shown below:

$$D^* + A \rightarrow D + A^*$$
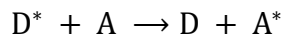
The FRET rate equation is:

$$k_{ET}(r) = \frac{1}{\tau_D}\left(\frac{R_0}{r}\right)^6$$

where $k_{ET}(r)$ is the energy transfer rate, τ_D is the natural emissive lifetime of the donor, r is the donor-acceptor distance, and R_0 is the Förster distance, described by the equation:

$$R_0^6 = Q_D \kappa^2 \frac{9000\,(\ln 10)}{128\,\pi^5\,N\,n^4}\,J$$

where Q_D is the natural quantum yield of the donor (0.82 for RPE), κ is a factor describing the spatial orientation of the transition dipoles (assumed here to be isotropic, $\kappa = 2/3$), N is

Avogadro's number (6.022×10^{23} mol^{-1}), n is the refractive index of the medium (1.33 for water), and J is the spectral overlap integral of the donor and acceptor, given by:

$$J = \int_0^\infty F_D(\lambda)\varepsilon_A(\lambda)\lambda^4 d\lambda$$

where $F_D(\lambda)$ is the area-normalized fluorescence spectrum of the donor, $\varepsilon_A(\lambda)$ is the extinction coefficient of the acceptor, and λ includes the overlap wavelength range. Donor emission and acceptor absorption spectra were measured as described in Section 2B, above. The light harvesting pigments of RPE are shown in Figure S2.13 and the FRET overlap is shown in Figure S2.14. J was found to be 1.14×10^{14} nm^4 M^{-1} cm^{-1}, R_0 was found to be 32.4 Å and a 1:1 RPE:[Ru(bpy)$_3$]$^{2+}$ FRET efficiency curve is shown in Figure S2.15.
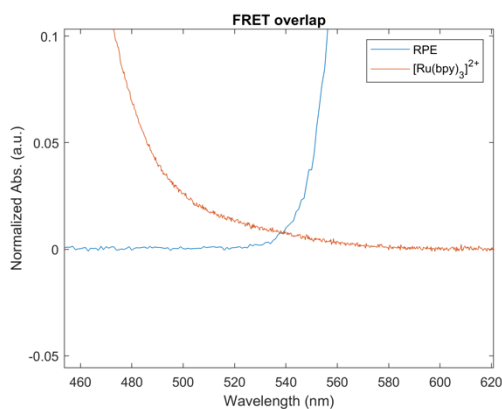
Figure S2.14: FRET overlap of RPE and [Ru(bpy)$_3$]$^{2+}$
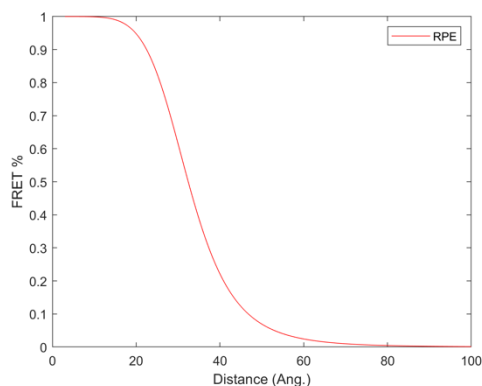
Figure S2.15: 1:1 RPE:[Ru(bpy)$_3$]$^{2+}$ FRET efficiency curve.
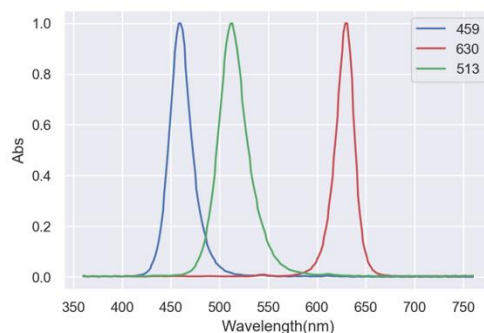
Figure S2.16: LED spectra.

The individual FRET rates for all 96 possible pigment-$[Ru(bpy)_3]^{2+}$ distances were determined. Ten of these rates were chosen at random, determined by the experimentally predicted number of $[Ru(bpy)_3]^{2+}$ per RPE, and used to calculate the total FRET rate, $k_{ET, tot}$.

$$k_{ET,tot} = \sum_{i=1}^{10} k_{ET,i}$$

where $k_{ET,i}$ represent the individual FRET rates. This process was repeated 100x and averaged to obtain the predicted ensemble lifetime of 409 ps, which then provided the predicted ensemble FRET efficiency of 78%, calculated using the below equation.[176]

$$E_{ET} = \frac{k_{ET,tot}}{k_{ET,tot} + \dfrac{1}{\tau_D}}$$

C. Energetics of $[Ru(bpy)_3]^{2+}$ Excitation under Red Irradiation

FRET from RPE to $[Ru(bpy)_3]^{2+}$, even under red irradiation, is enabled by uphill energy transfer. For red irradiation, the bandwidth of the LEDs was ~50 nm in the 95% confidence interval (600 nm–650 nm) as shown in Figure S16. Excitation at 600 nm corresponds to an energy of 47.7 kcal/mol. The triplet state energy is 48.9 kcal/mol and 47.0 kcal/mol in

aqueous solution for $[Ru(bpy)_3]^{2+}$ and $[Ru(4,4'-Me_2bpy)_3]^{2+}$, respectively,[9] which are the lowest energy states on the catalyst. The NHS-ester variant of $[Ru(bpy)_3]^{2+}$ used is expected to have a triplet state energy between the two tabulated values as the NHS-ester ligand is similar in structure to 4,4'-Me$_2$bpy. With the addition of thermal energy at room temperature ($k_BT=0.592$ kcal/mol), the $[Ru(bpy)_3]^{2+}$ states are accessible upon red irradiation.

4. Determination of Energy Transfer

A. Fluorescence Lifetime Experiments

Fluorescence lifetime measurements were performed on a Spectra Physics Mai Tai Ti:sapphire laser. The laser output (centered at 800 nm, 6 nm FWHM, 80 MHz repetition rate) was converted to a broadband supercontinuum (430-1000 nm) through the use of a nonlinear photonic crystal fiber (FemtoWhite 800, NKT Photonics). The excitation wavelength was selected with a 550 nm, 15 nm FWHM bandpass filter (Chroma Technology Corp. ET550/15x) to excite RPE (Figure S2.17). The excitation laser pulse was focused on a 1 cm x 2 mm pathlength quartz cuvette (Hellma Analytics) with a pulse energy of 0.027 nJ and a spot size of 0.66 μm^2. The emission wavelength was selected with a 580 nm, 10 nm FWHM bandpass filter (Thor Labs FB580-10) for RPE (Figure S2.18).[10] Emitted signal was detected with an avalanche photodiode (PDM Series, Micro Photon Devices) and arrival times were recorded by a time-correlated single photon counting module (PicoHarp 300, PicoQuant Inc.). The fluorescence intensity of the samples was monitored to ensure that no photodegradation occurred during the experiment. We observed no singlet-singlet annihilation at three different excitation powers (222.3 μW, 700 μW, and 2301 μW). The instrument response function (IRF) was measured using a scatter

56

solution containing phosphate buffer and HS-40 colloidal silica (Sigma-Aldrich) and determined to have a 75 ps FWHM. Fluorescence lifetime decay curves were individually fitted to a mono- or tri-exponential function using iterative reconvolution with the IRF. RPE-(Ru)$_n$'s strongly multi-exponential kinetics were able to be captured by tri-exponential fits. The fitted lifetime intensities were of the general form $I(t) = W + \sum_n A_n e^{-t/\tau_n}$, where W is a baseline offset term, which includes the microsecond $[Ru(bpy)_3]^{2+}$ photoluminescence, A_n is the amplitude for the nth component, τ_n is the time constant for the nth component, t is the time, I(t) is the intensity as a function of time, and the sum is over all n components contributing to the lifetime. The fitted parameters for RPE and RPE-(Ru)$_n$ are summarized in Tables S2.2 and S2.3.
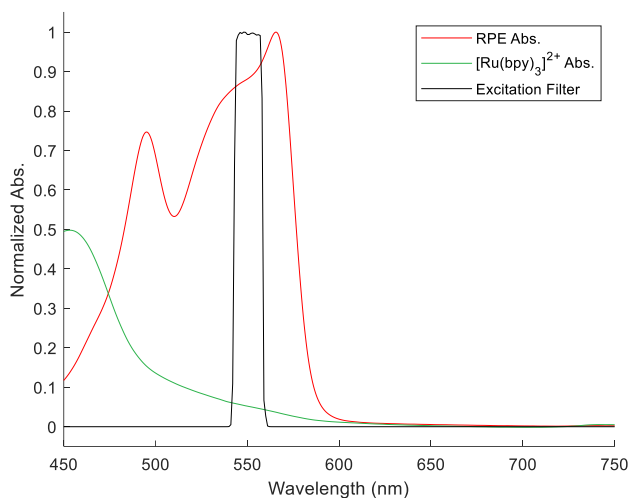
Figure S2.17: Excitation filter overlap with biohybrid components. Spectral overlap between the 550 nm excitation filter applied for fluorescence lifetime measurements and the individual biohybrid components.
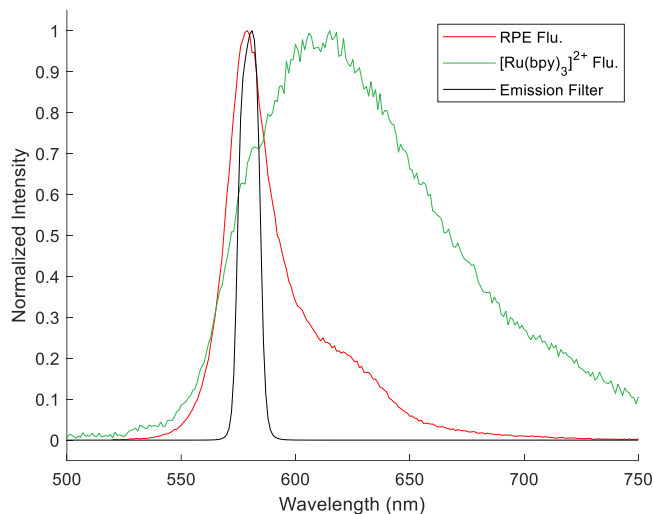
Figure S2.18: Emission filter overlap with biohybrid components. Spectral overlap between the 580 nm emission filter applied for fluorescence lifetime measurements and the individual biohybrid components.

Offset	A	τ (ns)
43.972	1	2.384
45.318	1	2.236
51.951	1	2.432
42.401	1	2.742
61.658	1	3.153
80.881	1	2.290
141.409	1	2.777
51.727	1	3.207
63.224	1	2.478
Average:		*2.633*
Standard Deviation:		*0.339*

Table S2.2: Fluorescence lifetime fitting parameters for RPE. Monoexponential fitting parameters for the free RPE protein, including the average lifetime obtained.

Offset	A_1	τ_1	A_2	τ_2	A_3	τ_3	Avr. Lifetime
67.097	0.000	0.000	0.758	0.227	0.242	1.562	0.549
81.606	0.801	0.000	0.178	0.212	0.021	0.993	0.059
78.888	0.755	0.000	0.202	0.187	0.043	0.768	0.071
73.792	0.000	0.000	0.704	0.290	0.296	1.367	0.608
103.588	0.479	0.191	0.379	0.594	0.141	1.758	0.565
137.165	0.000	0.000	0.749	0.365	0.251	1.395	0.623
134.798	0.444	0.000	0.334	0.333	0.222	0.956	0.323
96.754	0.000	0.000	0.986	0.524	0.014	8.093	0.627
101.076	0.920	0.000	0.040	0.454	0.040	1.889	0.093
83.065	0.439	0.000	0.362	0.174	0.200	0.676	0.198
53.292	0.000	0.000	0.771	0.228	0.229	0.665	0.328
136.660	0.380	0.229	0.487	0.631	0.133	1.812	0.635
124.435	0.205	0.000	0.495	0.304	0.300	1.026	0.459
105.644	0.886	0.000	0.056	0.368	0.058	0.778	0.066
100.273	0.423	0.168	0.463	0.622	0.114	1.760	0.560
Average:	*0.382*	*0.039*	*0.464*	*0.368*	*0.153*	*1.700*	0.384
Standard Deviation:	*0.330*	*0.079*	*0.274*	*0.155*	*0.098*	*1.761*	0.225

Table S2.3: Fluorescence lifetime fitting parameters for RPE-(Ru)$_n$. Triexponential fitting parameters for the RPE-(Ru)$_n$ biohybrid catalysts, including the average lifetime for each biohybrid sample as well as the average component lifetimes.

B. Ultrafast Transient Absorption Experiments

White light was generated from the 800 nm Ti:sapphire fundamental by focusing 2.8 W to a 1 m tube of argon gas pressurized to 20 psi for super continuum generation.[177] An 805 nm cut-off dichroic filter (Thorlabs) was used to attenuate the remaining intensity at the fundamental frequency. The pulse was compressed using two sets of chirped mirrors (Ultrafast Innovations GmbH, -40 fs^2/mm GVD compensation per double bounce[178]), and reduced in diameter from 6 mm to 3 mm using 2 concave mirrors (Newport). The compressed pulse was filtered to a center wavelength of 540 nm using a Schott® glass filter (Thor Labs FGB39), and subsequently split into two paths for the pump and probe arms using a 1 mm thick ultrafast beam splitter (Layertec). A 1 mm fused silica compensating window was used in the reflected beam path for comparable dispersion between both the pump and probe arms. The time delay between the pump and probe arms

was controlled using an Aerotech translational stage with a mounted retroreflector. The pulse duration was measured to be 290 fs as characterized by a second harmonic generation frequency resolved optical gating experiment (SHG-FROG) in which both the pump and probe pulses were combined in a barium borate (BBO) crystal (Figure S19). A 2.5 kHz optical chopper (model 3502, New Focus), was placed in the pump arm and coupled to the 5 kHz laser SDG (synchronization and delay generator) to allow for acquisition of sample spectra with the "pump on" and "pump off". A spherical mirror was used to focus both the pump and probe pulses to a 100 μm beam diameter in a non-collinear geometry. Pump and probe energies of 5 nJ and 8 pJ, respectively, were used for the free and conjugated RPE experiments. Power dependence of both the free and conjugated RPE sample kinetics are shown in Figure S2.20. The transient absorption signal was detected using a homebuilt spectrometer. Spectral dispersion was achieved using a holographic grating (450 grooves/mm, Wasatch Photonics), and spectra were collected on a 2048 pixel line-scan CCD (e2v Aviiva EM4-BA8). Spectra were collected at time delays stepped every 333 fs from -5.853 to 2.813 ps, 667 fs from 2.813 ps to 21.480 ps, and 6.667 ps from 21.480 ps to 728.147 ps to obtain kinetic traces.
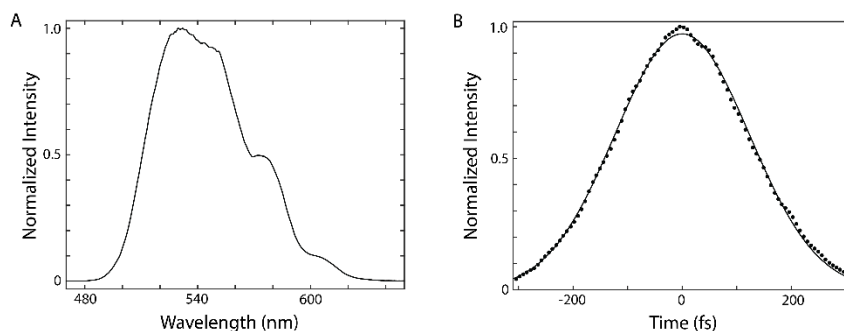
Figure S2.19: Transient absorption pulse characterization. (A) Pump pulse spectrum derived from a transient grating frequency resolved optical gating experiment. (B) Pump-probe overlap temporal profile from a second harmonic generation frequency resolved optical gating experiment (FWHM = 410 fs).
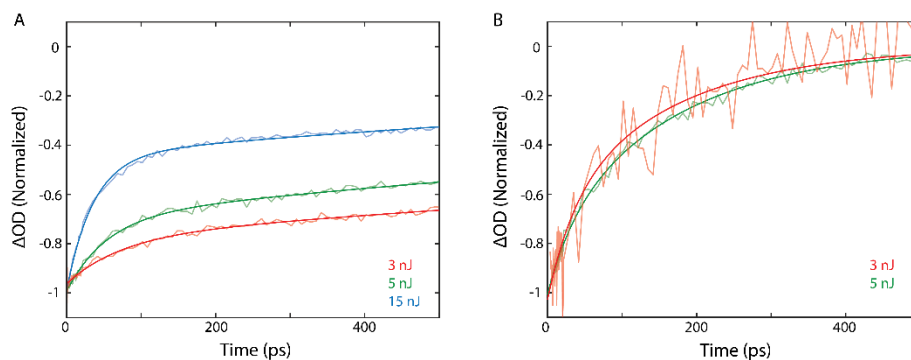
Figure S2.20: RPE and RPE-(Ru)ₙ power dependent dynamics. (A) 570 nm dynamics for RPE at 15 nJ, 5 nJ, and 3 nJ. (B) 570 nm dynamics for RPE-(Ru)ₙ at 5 nJ and 3 nJ.

Sample	Power (nJ)	A_1	τ_1 (ns)	A_2	τ_2 (ns)
RPE	15	0.55	0.036	0.45	1.6
RPE	5	0.30	0.054	0.70	2.2
RPE	3	0.20	0.073	0.80	3.3
RPE-Ru	5	0.24	0.034	0.76	0.17
RPE-Ru	3	0.36	0.036	0.64	0.167

Table S2.4: RPE and RPE-(Ru)ₙ power dependent dynamics. Kinetic parameters for 570 nm GSB/SE biexponential decays for RPE and RPE-(Ru)ₙ at varying excitation densities.

Figure S2.20 shows the power dependent dynamics for the RPE and RPE-(Ru)ₙ stimulated emission/ground state bleach at 570 nm. The decrease in biexponential lifetime (Table S2.4) on the picosecond and nanosecond timescales at high powers is likely due to exciton annihilation frequently present in multichromophoric systems.[179] The data collected at 5 nJ is shown in the main text owing to the sufficient signal to noise ratio for both the RPE and RPE-(Ru)ₙ samples, as well as the quantitative agreement between the nanosecond component of the transient absorption signal and the emission lifetime for RPE at this power. While we note that some exciton annihilation could be present at 5 nJ, the large difference in transient absorption decay timescales between the RPE and RPE-(Ru)ₙ samples at both 3 nJ and 5 nJ supports the emission lifetime measurements in highlighting energy transfer from RPE to $[Ru(bpy)_3]^{2+}$.
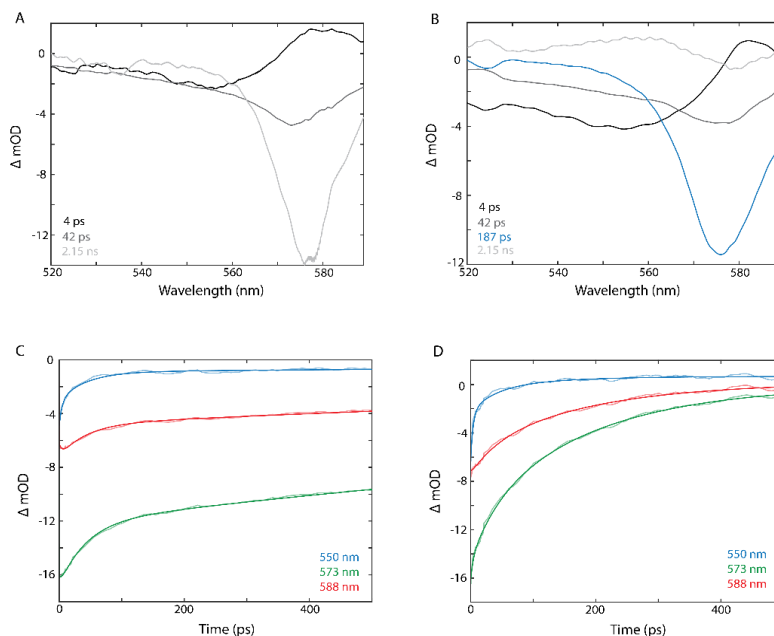
Figure S2.21: Global Analysis of RPE and RPE-(Ru)$_n$ transient absorption dynamics. (A) Decay associated spectra for RPE. (B) Decay associated spectra for RPE-(Ru)$_n$. (C) Traces of transient absorption signal (transparent) and global analysis fit (opaque) at selected wavelengths for RPE. (D) Traces of transient absorption signal (transparent) and global analysis fit (opaque) at selected wavelengths for RPE-(Ru)$_n$.

Global Analysis: In efforts to highlight the difference in timescales for the RPE and RPE-(Ru)$_n$ samples, we globally analyzed the transient absorption data. Owing to the large number of degenerate pigments, we used a global analysis for independent decays to identify the timescales of spectral evolution components. We used the graphical user interface Glotaran to analyze the spectra from 520 to 590 nm.[180] Figure S2.21 shows the decay associated spectra and agreement between the transient absorption data and model fit for both RPE and RPE-(Ru)$_n$. We fit the RPE data to a 3-component mode. The 4 ps component corresponded to either a Stokes shift or energy transfer between the pigments on the α and β subunits, the 42 ps component likely corresponds to energy migration between α β monomers within the hexameric structure, and the 2.15 ns component corresponds to the excited state emissive lifetime.[181] We fit the RPE-(Ru)$_n$ data to four

components with three of those constrained by the 4 ps, 42 ps, and 2.15 ns timescales of

RPE. The fourth component had a large GSB/SE signal with a timescale of 187 ps, which

we assigned to energy transfer from RPE to $[Ru(bpy)_3]^{2+}$. This value is also in qualitative

agreement with the transient absorption and emission lifetime biexponential kinetics, as

well as the predicted FRET timescale for the RPE-$(Ru)_n$ system.

Sample	A_1	τ_1 (ns)	A_2	τ_2 (ns)
RPE	0.7	0.023	0.3	1.2
RPE-Ru	1.0	0.040	-	-

Table S2.5: RPE and RPE-$(Ru)_n$ dynamics at 554 nm. Kinetic parameters for 554 nm GSB/SE decays for RPE (biexponential) and RPE-$(Ru)_n$ (monoexponential).
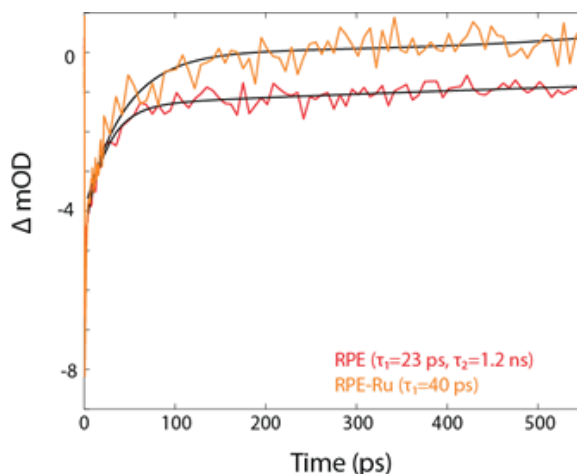
Figure S2.22: 554 nm transient absorption dynamics. GSB and ESA dynamics for RPE and RPE-$(Ru)_n$ at 554 nm (5 nJ).

Wavelength Dependent Transient Absorption Dynamics: Figure S2.22 and Table

S2.5 show the rapid decay in the SE/GSB signal for both RPE and RPE-$(Ru)_n$, suggesting

fast redistribution to lower energy pigments within the RPE complex. The RPE displays

two timescales, the 23 ps likely corresponding to energetic redistribution, while the long-

timescale component corresponds to the excited state lifetime. The RPE-$(Ru)_n$ is fit well

by only the short time component (40 ps) corresponding to energy redistribution within the

protein. The lack of a long-time component in the RPE-(Ru)$_n$ arises from the suppressed excited state lifetime due to energy transfer from the phycobiliprotein to the nearby [Ru(bpy)$_3$]$^{2+}$.

C. Nanosecond Transient Absorption Experiments

The basic details of the nanosecond TA (nsTA) are described in the text. Some additional details of sample preparation and data analysis are included here.

The unconjugated mixture was prepared in a 1:10 ratio of RPE and [Ru(bpy)$_3$]Cl$_2$. This ratio was selected to match the number of bound ruthenium chromophores on the RPE-(Ru)$_n$ as determined from intact mass spectrometry. The absorption spectra of the RPE-(Ru)$_n$ sample and the RPE and Ru mixture, shown in Figure S2.23, displays good qualitative overlap, suggesting that the relative stoichiometries of RPE and ruthenium catalyst are similar in the two samples.

Evidence for sensitization of the bound ruthenium chromophore was seen at wavelengths red of the 540 nm excitation wavelength used to generate the data shown in Figure 2.3C. The sample could be excited as red as 580 nm to generate a spectrum showing diagnostic [Ru(bpy)$_3$]$^{2+}$ ground state bleaches and excited state absorbances (Figure S2.24). Excitation further to the red of this was not possible due to the diminishing absorbance of the sample and decreasing intensity of the OPO output.

In this manuscript, the transient absorption spectra are described as prompt signals because, at the short delay used (5 ns), the dynamics are blurred by convolution with the gaussian pulse duration of the excitation source (8 ns FWHM) (Fig S2.25). To mitigate this effect in the case of the RPE-(Ru)$_n$ and unconjugated mixture spectra in Figure 2.3C, samples were run consecutively to ensure as comparable a time delay as possible.
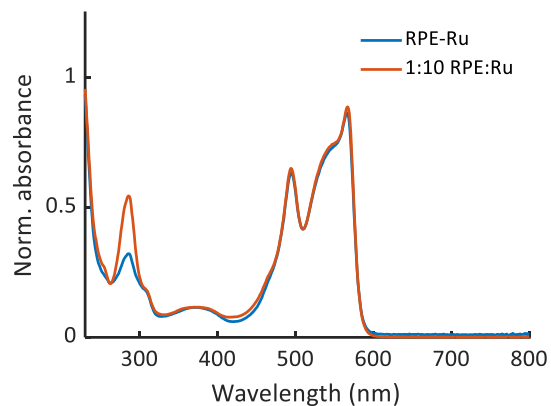
Figure S2.23: nsTA sample absorption. Normalized sample absorption of RPE-(Ru)$_n$ and RPE and Ru mixtures for nanosecond transient absorption.
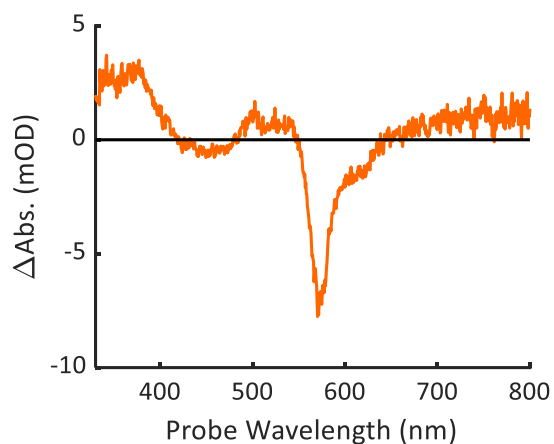
Figure S2.24: Red-excited RPE-(Ru)$_n$ nanosecond transient absorption. Prompt TA spectrum of RPE-(Ru)$_n$ collected after excitation with 1.6 mJ pulses of 580 nm light.
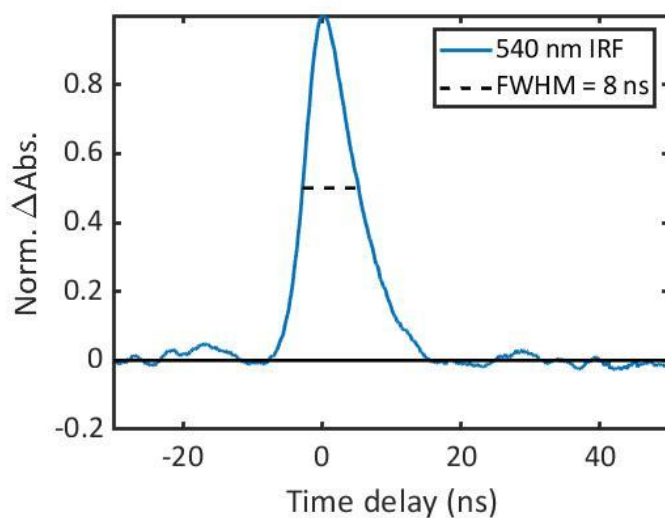
Figure S2.25: Nanosecond TA instrument response. Kinetic trace acquired at 560 nm of 540 nm excitation pulse. 8 ns FWHM indicated as a dashed line.

5. Synthetic Reactions

A. General information

Reagents. All commercial reagents and buffer salts were used as received without further purification.

Air-free reaction conditions. To maximize reproducibility by eliminating molecular oxygen, all reactions are prepared in an MBraun LABstar Pro Glovebox Workstation. Water and buffers were degassed by N_2 sparging for >30 min. RPE and RPE-(Ru)$_n$ solutions were degassed by spontaneous gas exchange in a water-saturated cold box inside the glovebox (>24 h).

Photoredox light set-up. All photoredox reactions are performed in a recrystallization dish lined with SMD 5050 LED strip lights powered with an LX1206 12V 6A power adaptor. Reactions are placed 10 mm away from the light source. The set-up is maintained at room temperature (23 °C) by an overhead fan unit.

NMR spectroscopy. Assay yields were collected by ^{1}H NMR against an external standard. ^{1}H NMR spectra were collected on Bruker UltraShield Plus Advance III 500 MHz. All products synthesized were previously reported in literature and are referenced throughout.

UV-Vis spectroscopy. UV-Vis absorbance spectra were recorded on SpectraMax iD5 Multi-Mode Microplate Reader, at room temperature, using Corning 96-well Flat Clear Bottom Polystyrene TC-treated Microplates.

B. Thiol-ene Coupling Reaction[182]
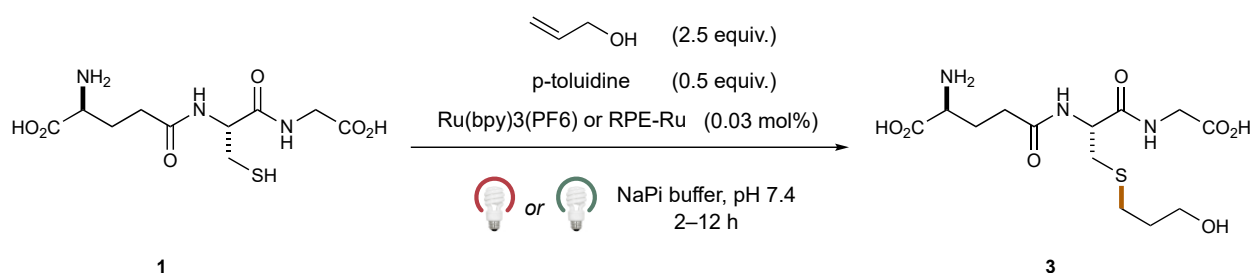
((R)-1-((carboxymethyl)amino)-3-((3-hydroxypropyl)thio)-1-oxopropan-2-yl)-*L*-glutamine (3) Glutathione (**1**, 10 μmol, 3.1 mg) was weighed out in a glass HPLC vial insert (spring bottom, 300 μL). The insert and a screw-top 2-mL HPLC vial were both brought into the glovebox for subsequent set up. Sparged allyl alcohol (25 μmol, 1.7 μL, neat) and *p*-toluidine (5 μmol, 1 μL of 5 M stock solution in DMSO) were added via a micropipette. Depending on the reaction conditions, [Ru(bpy)$_3$](PF$_6$)$_2$ (0.03 μmol, 1.5 μL of 20 mM stock solution in DMSO), RPE-(Ru)$_n$ (3 nmol, 240 kDa, 40 μL of 2 mg/mL stock solution in 100 mM sodium phosphate buffer, pH = 7.4), and/or RPE (3 nmol, 240 kDa, 40 μL of 2 mg/mL stock solution in 100 mM sodium phosphate buffer, pH = 7.4) were added via a micropipette. Additional phosphate buffer was added to adjust the total reaction volume to 50 μL. The insert was capped into the HPLC vial, sealed with parafilm, and brought outside the glovebox. It was irradiated for 2 or 12 hours inside a recrystallization dish lined with LED light strips, with green or red lights, respectively. Each vial was 10 mm away from

an LED light. Fans were cooling directly on top of the dish to maintain room temperature reactions conditions. After irradiation, 10 µL of 1 M maleic acid in H_2O was added to the reaction mixture. 10 µL of the resulting mixture was diluted with 550 µL of D_2O for ^1H NMR analysis. ^1H NMR (400 MHz, D_2O) δ 7.38 (d, $J = 7.8$ Hz, 1H), 7.32 (d, $J = 8.2$ Hz, 1H), 4.65 – 4.56 (m, 1H), 3.93 (s, 2H), 3.81 (d, $J = 6.5$ Hz, 1H), 3.69 (d, $J = 6.8$ Hz, 2H), 3.11 (dd, $J = 14.3, 5.4$ Hz, 1H), 2.95 – 2.87 (m, 1H), 2.68 (d, $J = 7.5$ Hz, 2H), 2.61 – 2.50 (m, 2H), 2.39 (s, 1H), 2.25 – 2.13 (m, 2H), 1.84 (p, $J = 6.1$ Hz, 2H).
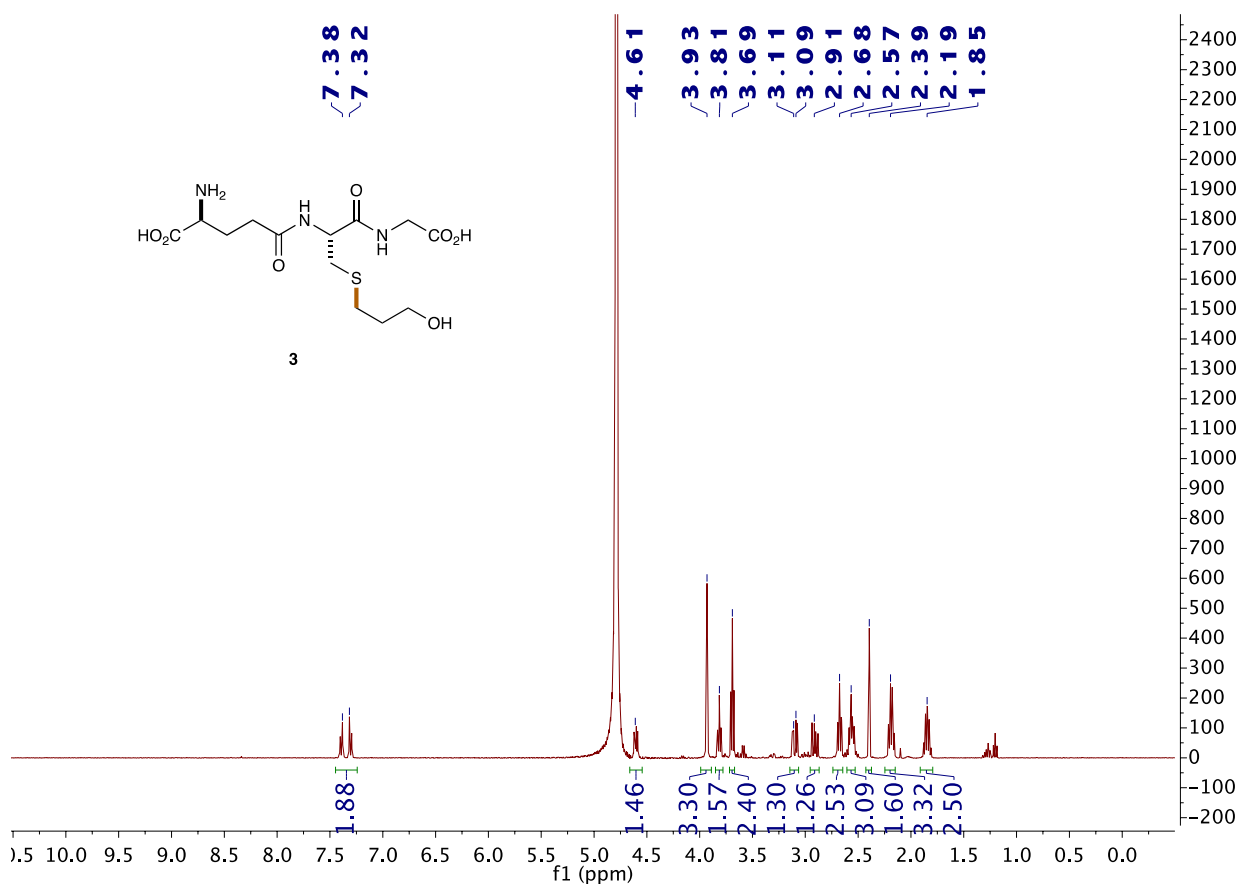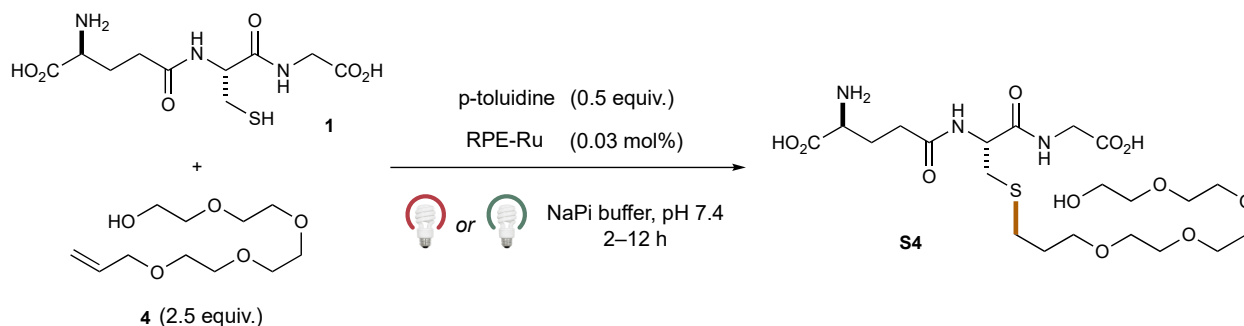
(*18R*,*23S*)-23-Amino-18-((carboxymethyl)carbamoyl)-1-hydroxy-20-oxo-3,6,9,12-tetraoxa-16-thia-19-azatetracosan-24-oic Acid (S4) Glutathione (**1**, 10 μmol, 3.1 mg) was weighed out in a glass HPLC vial insert (spring bottom, 300 μL). The insert and a screw-top 2-mL HPLC vial were both brought into the glovebox for subsequent set up. Degassed allyl(tetra)ethylene glycol[183] **5** (25 μmol, 5.2 μL, neat) and *p*-toluidine (5 μmol, 1 μL of 5 M stock solution in DMSO) were added via a micropipette. RPE-(Ru)$_n$ (3 nmol, 240 kDa, 40 μL of 2 mg/mL stock solution in 100 mM sodium phosphate buffer, pH = 7.4) was added via a micropipette. Additional phosphate buffer was added to adjust the total reaction volume to 50 μL. The insert was capped into the HPLC vial, sealed with parafilm, and brought outside the glovebox. It was irradiated for 2 or 12 hours inside a recrystallization dish lined with LED light strips, with fans directly on top of the dish. Each vial was 10 mm away from an LED light. After irradiation, 10 μL of 1 M maleic acid in H$_2$O was added to the reaction mixture. 10 μL of the resulting mixture was diluted with 550 μL of D$_2$O for ^{1}H NMR analysis. The shifts and spectra were previously reported by Yoon and coworkers.[182] A crude ^{1}H NMR is included below, actual yields are adjusted based on exact substrate amount.

(2*S*)-2-Amino-5-(((2*R*)-1-((carboxymethyl)amino)-1-oxo-3-((3-((4-((4*S*)-2-oxohexahydro-1H-thieno[3,4-d]imidazol-4-yl)-butanoyl)oxy)propyl)thio)propan-2-yl)amino)-5-oxopentanoic Acid (S5) Glutathione (**1**, 10 μmol, 3.1 mg) and allyl biotin[184] **6** (25 μmol, 7.1 mg) were weighed out in a glass HPLC vial insert (spring bottom, 300 μL). The insert and a screw-top 2-mL HPLC vial were both brought into the glovebox for subsequent set up. Degassed *p*-toluidine (5 μmol, 1 μL of 5 M stock solution in DMSO) was added via a micropipette. RPE-(Ru)$_n$ (3 nmol, 240 kDa, 40 μL of 2 mg/mL stock solution in 100 mM sodium phosphate buffer, pH = 7.4) was added via a micropipette. Additional phosphate buffer was added to adjust the total reaction volume to 100 μL. The insert was capped into the HPLC vial, sealed with parafilm, and brought outside the glovebox. It was irradiated for 2 or 12 hours inside a recrystallization dish lined with LED light strips, with fans directly on top of the dish. Each vial was 10 mm away from an LED light. After irradiation, 10 μL of 1 M maleic acid in H_2O was added to the reaction mixture. 10 μL of the resulting mixture was diluted with 550 μL of D_2O for ^{1}H NMR analysis. The shifts and spectra were previously reported by Yoon and coworkers.[182] A crude ^{1}H NMR is included below, actual yields are adjusted based on exact substrate amount.

p-toluidine (0.5 equiv.)

RPE-Ru (0.03 mol%)

NaPi buffer, pH 7.4
2–12 h

1

6 (2.5 equiv.)

S6

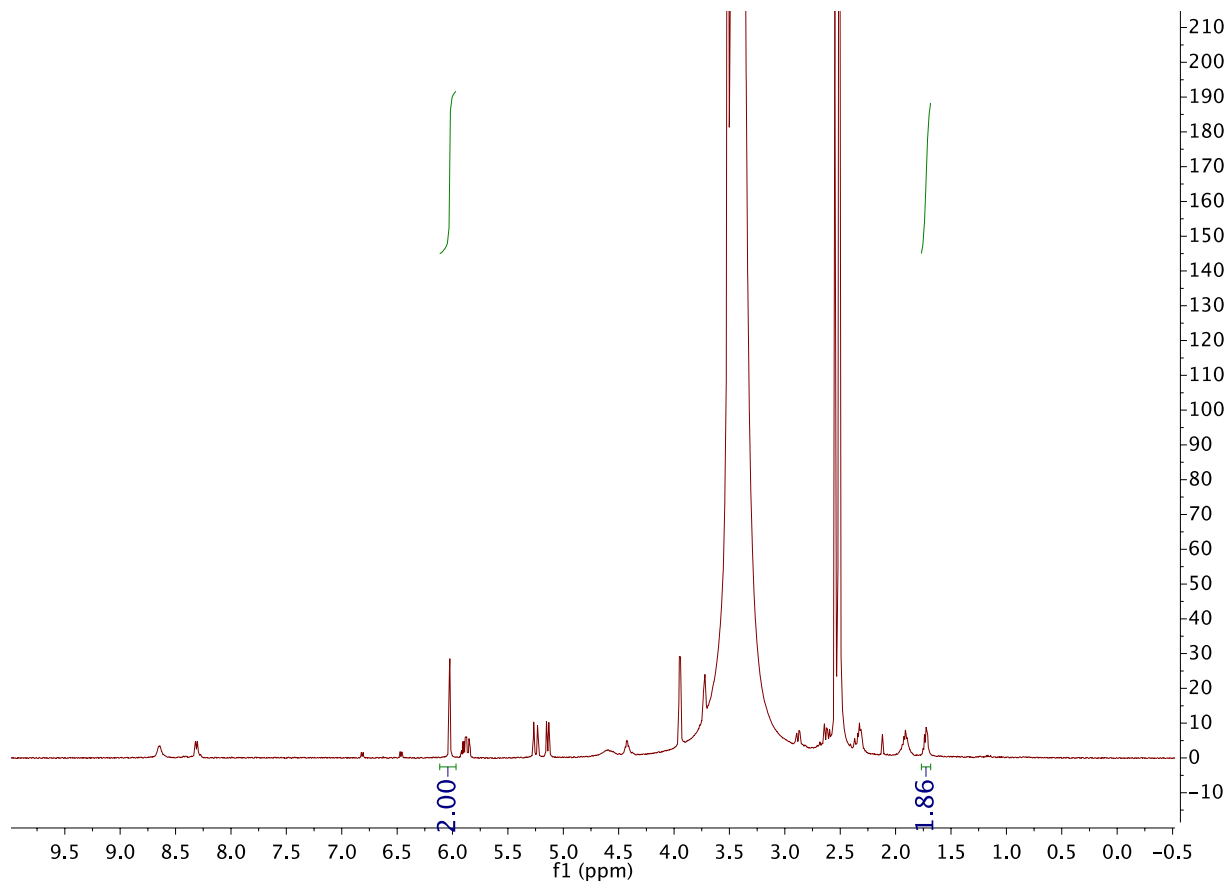**(*S*)-2-Amino-5-(((*R*)-3-((6-azidohexyl)thio)-1-((carboxymethyl)amino)-1-oxopropan-2-yl)amino)-5-oxopentanoic acid (S6)** Glutathione (**1**, 10 μmol, 3.1 mg) was weighed out in a glass HPLC vial insert (spring bottom, 300 μL). The insert and a screw-top 2-mL HPLC vial were both brought into the glovebox for subsequent set up. Degassed azide[185] **7** (25 μmol, 3.4 μL, neat) and *p*-toluidine (5 μmol, 1 μL of 5 M stock solution in DMSO) were added via a micropipette. RPE-(Ru)$_n$ (3 nmol, 240 kDa, 40 μL of 2 mg/mL stock solution in 100 mM sodium phosphate buffer, pH = 7.4) was added via a micropipette. Additional phosphate buffer was added to adjust the total reaction volume to 50 μL. The insert was capped into the HPLC vial, sealed with parafilm, and brought outside the glovebox. It was irradiated for 2 or 12 hours inside a recrystallization dish lined with LED light strips, with fans directly on top of the dish. Each vial was 10 mm away from an LED light. After irradiation, 10 μL of 1 M maleic acid in H_2O was added to the reaction mixture. 10 μL of the resulting mixture was diluted with 550 μL of D_2O for ^{1}H NMR analysis. The shifts and spectra were previously reported by Yoon and coworkers.[182] A crude ^{1}H NMR is included below, actual yields are adjusted based on exact substrate amount.

(S)-2-Amino-5-(((R)-1-((carboxymethyl)amino)-1-oxo-3-((3-((2R,3S,4R,5S,6R)-3,4,5-triacetoxy-6-(acetoxymethyl)-tetrahydro-2H-pyran-2-yl)propyl)thio)propan-2-yl)amino)-5-oxopentanoic Acid (S7) Glutathione (**1**, 10 μmol, 3.1 mg) and allylated tetraacetate galactose[186] **6** (25 μmol, 9.3 mg) were weighed out in a glass HPLC vial insert (spring bottom, 300 μL). The insert and a screw-top 2-mL HPLC vial were both brought into the glovebox for subsequent set up. Degassed *p*-toluidine (5 μmol, 1 μL of 5 M stock solution in DMSO) was added via a micropipette. RPE-(Ru)$_n$ (3 nmol, 240 kDa, 40 μL of 2 mg/mL stock solution in 100 mM sodium phosphate buffer, pH = 7.4) was added via a micropipette. Additional phosphate buffer was added to adjust the total reaction volume to 100 μL. The insert was capped into the HPLC vial, sealed with parafilm, and brought outside the glovebox. It was irradiated for 2 or 12 hours inside a recrystallization dish lined with LED light strips, with fans directly on top of the dish. Each vial was 10 mm away from an LED light. After irradiation, 10 μL of 1 M maleic acid in H$_2$O was added to the reaction mixture. 10 μL of the resulting mixture was diluted with 550 μL of D$_2$O for ^{1}H NMR analysis. The shifts and spectra were previously reported by Yoon and coworkers.[182] A crude ^{1}H NMR is included below, actual yields are adjusted based on exact substrate amount.
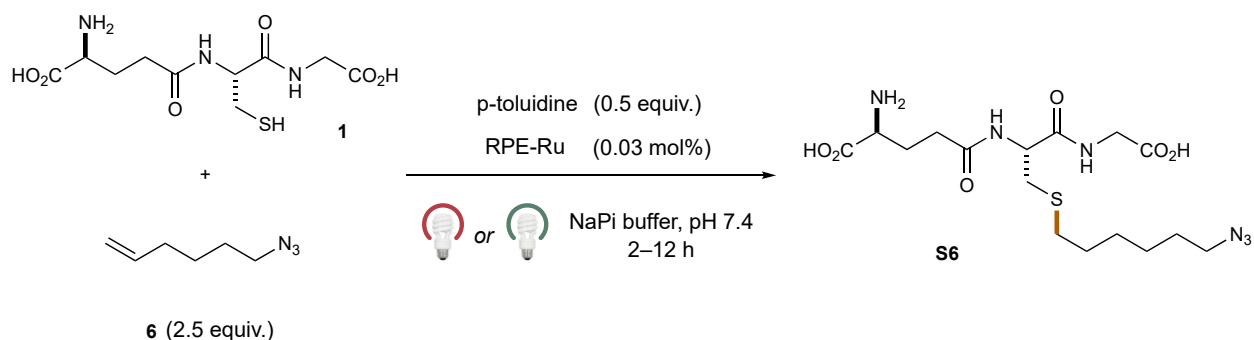
C. Cysteinyl Desulfurization Reaction[187]
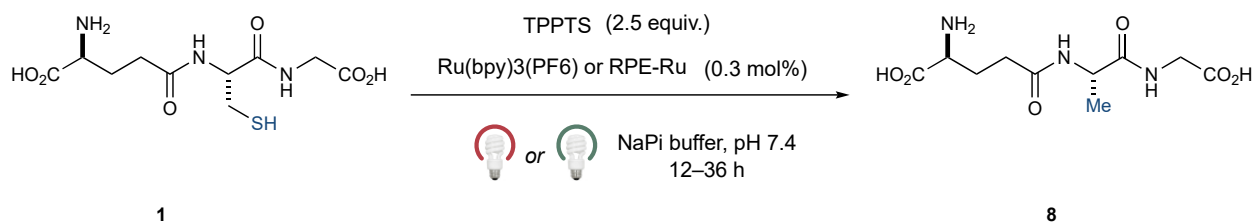
Glutathione (**1**, 1 µmol, 5 µL of 200 mM stock in 100 mM sodium phosphate buffer, pH = 7.4), 3,3′,3″-phosphanetriyltris trisodium salt (TPPTS, 2.5 µL, 5 µL of 500 mM stock in NaPi buffer) was added was a glass HPLC vial insert 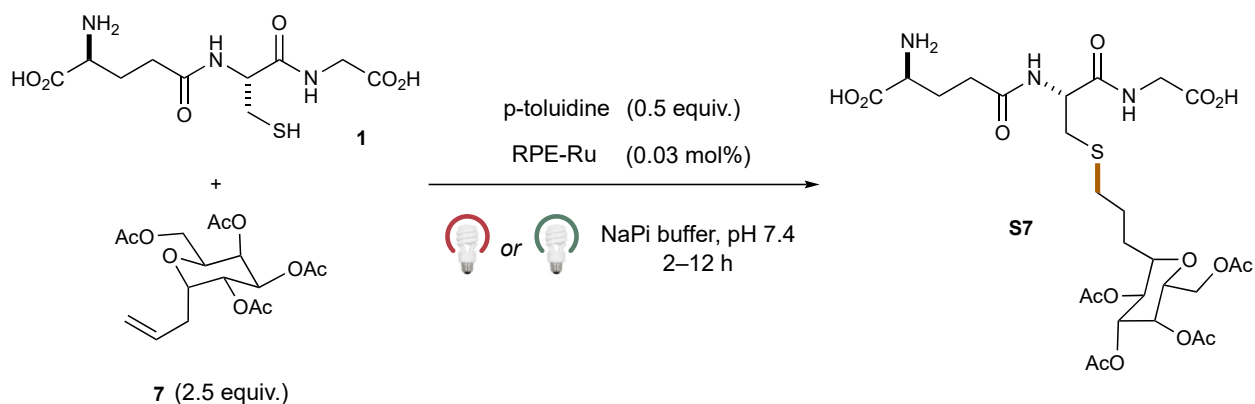(spring bottom, 300 µL) under inert atmosphere. Depending on the reaction conditions, $[Ru(bpy)_3](PF_6)_2$ (0.03 µmol, 1.5 µL of 20 mM stock solution in DMSO), RPE-$(Ru)_n$ (3 nmol, 240 kDa, 40 µL of 2 mg/mL stock solution in NaPi buffer), and/or RPE (3 nmol, 240 kDa, 40 µL of 2 mg/mL stock solution in NaPi buffer) were added via a micropipette. Additional phosphate buffer was added to adjust the total reaction volume to 100 µL. The insert was capped into the HPLC vial, sealed with parafilm, and brought outside the glovebox. It was irradiated for 12 or 36 hours inside a recrystallization dish lined with LED light strips, with fans directly on top of the dish. Each vial was 10 mm away from an LED light. After irradiation, 10 µL of 1 M maleic acid in H_2O was added to the reaction mixture. 10 µL of the resulting mixture was diluted with 550 µL of D_2O for ^1H NMR analysis. The shifts and spectra for product **8** were previously reported by Guo and coworkers.[187]

To compare our RPE-Ru catalyst to literature reports, the desulfurization reaction was further evaluated at the literature-reported 5 h irradiation time under blue, green, and red light irradiation. The reactions are analyzed by ^1H NMR analysis and the results are summarized in the table below. Guo and coworkers report 85% yield under blue light irradiation after 5 hours. We attribute the discrepancy in yield to the difference in reaction set up, light source, and scale.

photocatalyst	time	459 nm	513 nm	630 nm
[Ru(bpy)$_3$](PF$_6$)$_2$	5 h	59%	0%	0%
RPE-Ru conjugate	5 h	67%	38%	11%

D. Biohybrid catalyst recovery

The desulfurization reaction was performed at 10 µmol scale and 500 µL reaction volume, irradiated for 12 hours under green and red LEDs. 10 µL of reaction was removed for ^{1}H NMR analysis. The remaining volume was desalted with Amicon Ultra centrifugal filter units with fresh NaPi buffer (30 kDa molecular weight cut off, 0.5 mL size, 3 x 10 min at 6000 g, 4 °C). The repurified catalyst was degassed by spontaneous gas exchange and reconstituted to 400 µL again with degassed buffer. The prepared catalyst solution was resubjected to desulfurization reaction conditions at 1 µmol scale.

6. Quantum Yield Evaluation of the Thiol-Ene Coupling and Desulfurization Reactions

Quantum yields of the thiol-ene reactions under green light irradiation was determined via actinometry. The ferrioxalate actinometer (K$_3$[Fe(C$_2$O$_4$)$_3$]) and phenanthroline-based developing solutions were made using a previously published method.[188] Briefly, a 0.15 mM ferrioxalate solution in 0.01 N sulfuric acid was prepared for 510 nm irradiation. 50 µL aliquots of the actinometric solution were irradiated in the same manner as the reported thiol-ene coupling reactions (5 – 120 min, time points in triplicate). 5 µL of each irradiated sample was added to 195 µL of the spectrometric solution (6 mM 1,10-phenanthroline in acidic NaOAc buffer). The samples were aged for at least 30 min in the dark, then absorbance was measured at 510 nm. The Fe^{2+}

concentration was back calculated from an $Fe(SO_4)_2$ concentration calibration curve (using the Beer-Lambert Law).

Experiment set up timepoints

$$y = 0.0009x + 0.0437$$
$$R^2 = 0.9867$$

Fe2+ calibration curve

$$y = 0.0066x + 0.004$$
$$R^2 = 0.9998$$
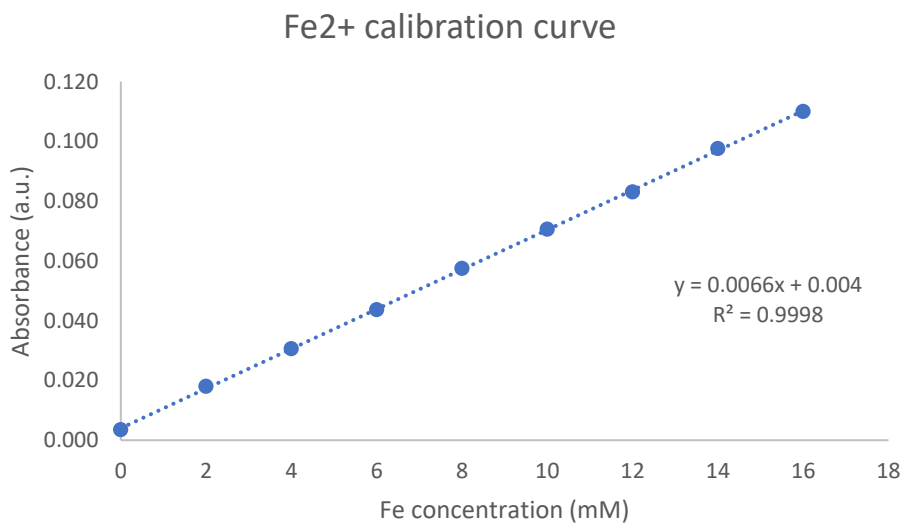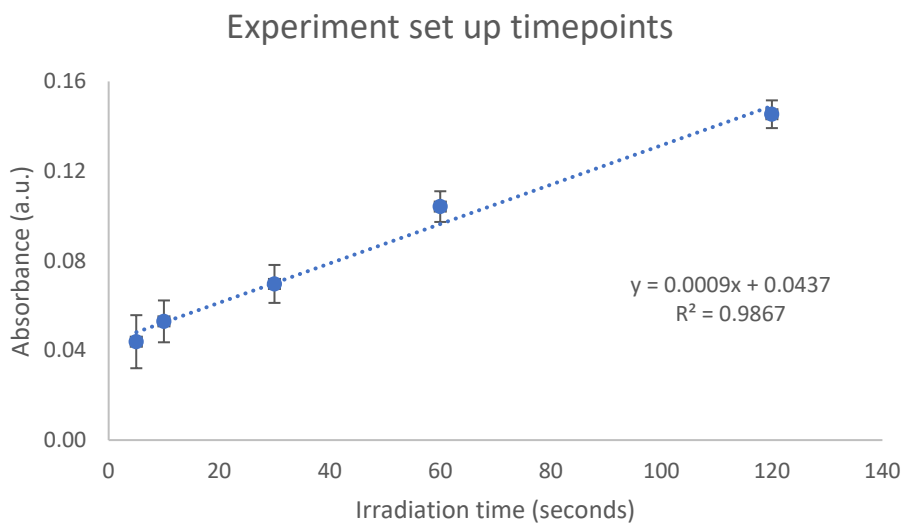
The number of photons absorbed by the system was calculated to be 1.71×10^{-10} einstein/sec. The ferrioxalate $\rightarrow$ Fe^{2+} quantum yield is 0.86 at 510 nm irradiation at room temperature. The quantum yields of the thiol-ene click coupling reaction is reported below:

photocatalyst	reaction	wavelength	QY
$[Ru(bpy)_3](PF_6)_2$	thiol-ene	510 nm	4081
RPE-Ru conjugate	thiol-ene	510 nm	42559
$[Ru(bpy)_3](PF_6)_2$	desulfurization	510 nm	0
RPE-Ru conjugate	desulfurization	510 nm	2215

The high quantum yield values (>1) support a radical chain mechanism.[189]

CHAPTER 3:
TOWARDS GENERALITY – PHOTOENZYMATIC CATALYSIS IN A NEW LIGHT: *GLUCONOBACTER* 'ENE'-REDUCTASE CONJUGATES POSSESSING HIGH-ENERGY REACTIVITY WITH TUNABLE, LOW-ENERGY EXCITATION

3.1 INTRODUCTION

Enzymes are ideal catalysts for chemical synthesis because they can precisely control reactive intermediates to provide unparalleled levels of stereoselectivity. However, they cannot be broadly applied to synthetic challenges because they are often assumed to be limited to their native functions.[190–197] We recently demonstrated that flavin-dependent 'ene'-reductases (EREDs), when irradiated with visible light, can catalyze non-natural free radical reactions. This strategy has proven general and enabled EREDs to solve selectivity challenges in free radical chemistry that are not easily addressed using small molecule catalysts.[198–204]

A central challenge associated with this reactivity is the need for high intensity cyan light to achieve the desired reaction. The photoactive intermediate, an enzyme-templated charge-transfer complex formed between the alkyl halide substrate and the hydroquinone oxidation state of the flavin cofactor (FMN_{hq}),[205,206] only has a small absorption window at the blue edge of the visible spectrum (λ_{max} = 494 nm). While the benchmark photoenzyme for these studies, the ERED from *Gluconobacter* (GluER-T36A), already has a low molar absorption coefficient of 1.14 x 10^4 $M^{-1}cm^{-1}$ in the oxidized state, the catalytically active charge-transfer complex the enzyme forms has an even lower molar absorption coefficient of ~3,600 $M^{-1}cm^{-1}$.[198,207] Enzymes from this family were chosen for their reactivity and selectivity and so lack the light-harvesting prowess required for efficient capture of photoenergy. In photosynthesis, nature overcame the challenge of

simultaneously optimizing for two functions by evolving separate protein machinery for reactivity and light-harvesting.[113,115,208–212] While small-molecule catalytic systems have been developed to mimic this approach,[147,151,154,213–216] strategies for synthetic photoenzymes are unknown. Introducing this separation to photoenzymes has the potential to increase the capacity of photoenzymes across a range of transformations while maintaining the stereoselectivity intrinsic to enzymatic catalysis.

Here, we conjugated a light-harvesting moiety, a strongly absorbing fluorophore with a molar absorption coefficient of $\sim 1 \times 10^5$ M^{-1}cm^{-1}, to GluER-T36A, an enzyme mutated to enable non-natural reactivity in high yield and stereoselectivity. The separation of light harvesting and reactivity led to increased yields and the introduction of reactivity for intramolecular and intermolecular hydroalkylation of alkenes, respectively. Remarkably, separation of these functions also enabled photoactivity under green irradiation, opening the door to biological manipulations and other applications that require low energy irradiation (Figure 3.1).
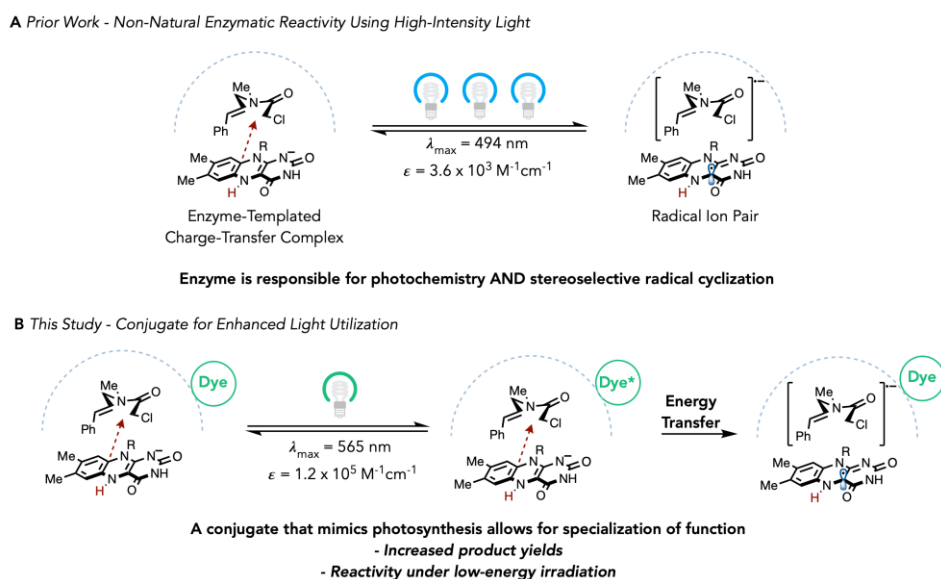
Figure 3.4: Approach to enhanced light utilization. (A) Photoenzymes performing both light-harvesting and reactivity need high-energy, high-intensity light for productive chemistry. (B) Conjugated ATTO dyes which transfer their absorbed energy to the photoenzyme enable low-energy, low-intensity light to catalyze reactions.

3.2 RESULTS AND DISCUSSION

3.2.1 Conjugation and Structural Characterization

A series of conjugates were synthesized by covalently linking the photoenzyme GluER-T36A to fluorescent dyes and a fluorescent protein. The photoenzyme GluER-T36A and its progeny exhibit non-natural photoreactivity that enables formation of products with high stereoselectivity and yields. Establishing the conjugate strategy on GluER-T36A allows for straightforward extension to other GluER variants or ERED homologs. The fluorescent dyes, ATTO 495, 520, 565, and 590 (named for their absorption maximum; SI Figure S3.1), exhibit molar absorption coefficients of $8.0 \times 10^4 - 1.2 \times 10^5$ M^{-1}cm^{-1}, approximately two orders of magnitude above that of the photoenzymatically active GluER-T36A charge-transfer state. The dyes also have absorption bandwidths ~100 nm broader than GluER-T36A, which allows for the use of green light irradiation. GluER-T36A possesses 15 surface-exposed lysine residues around the enzyme (SI Figure S3.8). All ATTO conjugates were constructed using direct coupling of lysine side chains to dyes containing an *N*-hydroxysuccinimide (NHS) ester moiety. The fluorescent protein, R-phycoerythrin (RPE), is a natural light-harvesting protein from red algae with an extremely high molar absorption coefficient of 1.96×10^6 M^{-1}cm^{-1} and an additional ~150 nm of absorption bandwidth, further extending the absorption to allow red irradiation. The RPE-GluER-T36A conjugate was synthesized by first modifying the proteins individually. The lysine residues of RPE reacted with *N*-succinimidyl-*S*-acetylthioacetate (SATA), which upon deacetylation with hydroxylamine reveals a nucleophilic thiol. Concurrently, lysines on GluER-T36A were reacted with succinimidyl iodoacetate (SIA). The modified proteins were then combined and crosslinked via a substitution reaction to obtain the product (SI Section II-1).

To confirm conjugation of the ATTO dye to GluER-T36A, we performed intact mass spectrometry (MS), absorption spectroscopy, and steady-state fluorescence spectroscopy. The photoenzyme alone exhibited a single prominent MS peak at 40,034 Da, in agreement with prior literature,[11] while the conjugate samples exhibited multiple peaks at higher molecular weights (SI Section I-1A). Gradations between peaks were consistent with the mass of the ATTO dyes (333 Da, 349 Da, 492 Da, and 573 Da for ATTO 495, 520, 565, and 590, respectively). A weighted average of these peaks led to the assignment of an average of five, five, six, and five dyes conjugated per GluER-T36A for ATTO 495, 520, 565, and 590, respectively.

The absorption spectrum of the ATTO 565-GluER-T36A conjugate is shown in Figure 3.2A. Due to the large molar absorption coefficient of the dyes, the GluER-T36A absorption features were completely obscured (Figure 3.2A, SI Figure S3.6). The absorption spectrum of the ATTO dyes develops a double peak structure upon protein conjugation, and all of the GluER-T36A conjugates exhibited this spectral feature, indicative of successfully bound ATTO dye.[217] Absorption spectra were also recorded for the remaining unconjugated dye to determine the amount of unreacted ATTO dye. This value was subtracted from the amount initially added to the reaction to obtain labeling ratios. These ratios were similar to those determined through MS (SI Section I-1B). Finally, while GluER-T36A is non-emissive, the purified conjugates exhibited fluorescence maxima equivalent to the ATTO dyes (Figure 3.2A, SI Figure S3.6), confirming the presence of conjugated ATTO dyes.

For the purified RPE-GluER-T36A conjugates, decomposition of the absorption spectra into the two components showed 1-3 GluER-T36A per RPE, indicating successful conjugation. Similarly, fluorescence of RPE was observed after purification of the conjugate from the reaction mixture (SI Figure S3.19).
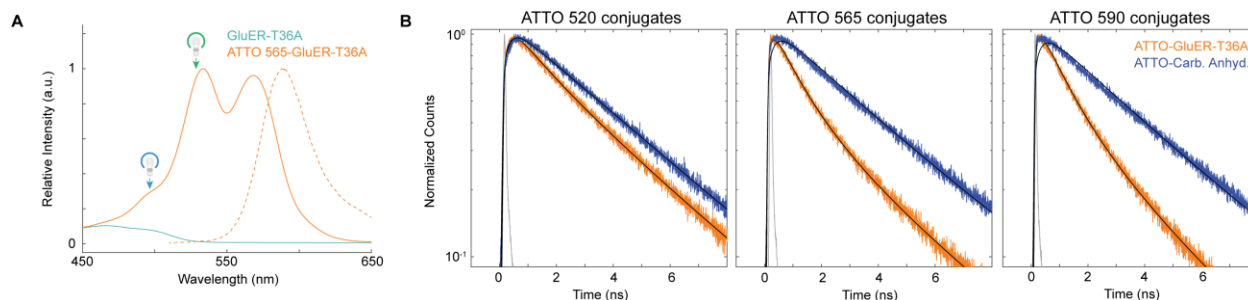
Figure 3.5: Spectroscopic characterization of conjugation and energy transfer. (A) Absorption spectra of GluER-T36A (teal) and absorption (solid orange) and emission (dashed orange) spectra of an ATTO 565-GluER-T36A conjugate. (B) Nanosecond fluorescence decays of GluER-T36A conjugates (orange) as compared to carbonic anhydrase conjugates (blue). The IRF is shown in gray.

3.2.2 Characterization of Energy Transfer between Components

Time-resolved fluorescence measurements were used to characterize energy transfer efficiency in the conjugates (Figure 3.2B, SI Section I-2C). The reduction in fluorescence lifetime in the presence of GluER-T36A reports on the timescale, and thus efficiency, of energy transfer to the enzyme cofactor. To ensure that changes in ATTO lifetime were due to energy transfer to the cofactor, ATTO conjugates were also prepared with carbonic anhydrase. Carbonic anhydrase has a similar molecular weight (30 kDa) and number of surface-exposed lysines (18) to GluER-T36A but lacks the flavin cofactor. The ATTO-carbonic anhydrase conjugates exhibited the same ATTO absorption features that were observed with the GluER-T36A conjugates (SI Figure S3.6).

Fluorescence lifetimes were measured for the ATTO-carbonic anhydrase and ATTO-GluER-T36A conjugates. The fluorescence decay curves of the ATTO-carbonic anhydrase conjugates were fit with a mono-exponential function that gave lifetimes of 3.82 (±0.05) ns, 3.75 (±0.24) ns, and 3.60 (±0.03) ns for ATTO 520, ATTO 565, and ATTO 590 conjugates, respectively. The ATTO 495 conjugates were not measured owing to their low predicted energy transfer efficiency and instrumental limitations. The ATTO-carbonic anhydrase average lifetimes match well with the values of the free dyes (SI Tables S3.3 and S3.4). The decay curves of the ATTO-

85

GluER-T36A conjugates were best fit with a stretched mono-exponential function, which captures the heterogeneous lifetimes owing to variation in the number and location of conjugated dyes from the stochastic nature of the reaction.[218] The fits gave a β value of ~0.5 for all ATTO-GluER-T36A samples and lifetimes of 2.30 ($\pm$0.55) ns, 0.630 ($\pm$0.38) ns, and 0.985 ($\pm$0.21) ns for ATTO 520, ATTO 565, and ATTO 590 conjugates, respectively. The lifetime reductions for the ATTO-GluER-T36A samples as compared to the ATTO-carbonic anhydrase samples indicate the presence of successful energy transfer from the dyes to the enzyme cofactor. Consistently, 0.5 is the theoretical β value for three-dimensional systems of multiple identical donors that transfer energy to a single acceptor.[34]

The reduction in lifetime for the GluER-T36A conjugates corresponds to energy transfer efficiencies of 40%, 83%, and 73% for ATTO 520, ATTO 565, and ATTO 590 conjugates, respectively. To investigate the microscopic origin of the energy transfer, theoretical efficiencies were calculated by using Förster theory to describe transfer from the ATTO dyes to the GluER-T36A oxidized flavin state averaged over all possible conjugation sites (SI Section I-2). Energy transfer efficiencies of 72%, 74%, and 71% were predicted for ATTO 520, ATTO 565, and ATTO 590 conjugates, respectively. For all dye conjugates, the spectral overlap between the dye emission and photoenzyme absorption constitutes only 0.03-0.04% of the total spectrum (SI Section I-2), meaning efficient energy transfer is attained despite limited overlap. The high efficiency comes from the short distance (<3.2 nm) between the dye and the flavin cofactor for all conjugates, as energy transfer depends inversely on distance to the sixth power.[218] Owing to these factors, efficient energy transfer can be achieved for a wide range of dye spectra, thereby allowing selection of a desired excitation wavelength. The predicted efficiencies for the ATTO 565 and ATTO 590 conjugates have good agreement with the experimental values. The predicted efficiency for the

ATTO 520 conjugates, however, is higher than the experimental value. The ATTO 520 conjugates exhibited a larger dispersity in dye stoichiometry (SI Section I-1A), likely from the shorter reaction time of this dye.[219] The conjugates with low labelling stoichiometry may have dyes conjugated to inefficient (more exposed) residues far from the active site, leading to lower overall energy transfer. Even with this lower value, relatively high energy transfer efficiencies were achieved for the broad range of spectral characteristics, demonstrating that this approach is robust to a variety of photophysical properties.

To quantify energy transfer for the RPE construct, the lifetime of the RPE was compared for RPE alone and for the RPE-GluER-T36A conjugates. The lifetime decreased from 2.34 ns for RPE to 1.92 ns for RPE-GluER-T36A. All samples exhibited mono-exponential kinetics. The reduction corresponds to an energy transfer efficiency of 18%, consistent with theoretical predictions of 17% for the oxidized flavin state. The lower efficiency is a result of the longer distance between the RPE chromophores and the flavin cofactor due to the size of the protein structure. Although the efficiency is low, the presence of energy transfer demonstrates an entirely protein-based light-harvesting-enhanced photoenzyme.

3.2.3 Demonstration of Photoenzymatic Activity

To show the enhanced synthetic activities of the GluER-T36A conjugates, we compared the reactivity of the GluER-T36A conjugates to free GluER-T36A under cyan (490 nm), green (530 nm), and/or red (630 nm) LED irradiation (SI Section I-3, II-5). We first examined the model cyclization of an α-chloroamide to afford a β-chiral lactam.[198] In the previous study, high intensity irradiation with cyan light was needed for the reaction to produce product in 92% yield and a 94:6 enantiomeric ratio using GluER-T36A. We hypothesized that similar yields could be achieved

using lower intensity and lower energy light with the ATTO 565-GluER-T36A conjugate due to its enhanced light-harvesting properties.

Pleasingly, we were able to achieve an 85% yield of the β-chiral lactam and an increased enantiomeric ratio of 96:4 using dim green LEDs and the ATTO 565-GluER-T36A conjugate (Figure 3.3A). There was comparatively low background reactivity and diminished enantiomeric ratios (19% yield and 92:8 enantiomeric ratio) using free GluER-T36A. The measured power at the reaction distance for the green LED was 310 μW, three orders of magnitude lower than the cyan LED used in the original report (152 mW), although the reaction setups have different spatial geometries between the reaction vial and LED, precluding a direct comparison (SI Figure S3.14). The use of ATTO 565-GluER-T36A also allowed the catalyst loading to be decreased by half (0.25 mol % rather than 0.5 mol %) while maintaining high product yields. A 48 h reaction time was selected based on previous optimization with GluER variants at low enzyme loading.[14] We also characterized the dependence of product yield on light intensity and excitation wavelength for the lactam cyclization using ATTO 565-GluER-T36A and GluER-T36A (Figure 3.3B, Table S3.6). Under green irradiation near the maximum of the ATTO 565 absorption, the obtained product yields for GluER-T36A increased from 4% to 22% with an increase in LED power from 52 μW to 417 μW. The product yields for the ATTO 565-GluER-T36A conjugate for the same LED powers ranged from 35% to 85%, which is a 3- to 9-fold increase as compared to GluER-T36A alone. We assign the increase in product yields to the presence of light harvesting, suggesting that the reaction with GluER-T36A alone was light limited consistent with our previous conclusion.[9] At the highest LED power, the product yield decreased from the maximum value of 85% down to 60% for the conjugate. The decrease in product yield may be due to multiple factors: an 8% increase in the amount of conjugate photodegradation (SI Section I-1B); photo-induced aggregation, which was

observed as a whitish-pink precipitate in the reaction vial under maximum intensity light; and/or

unwanted photochemistry at powers beyond the capacity of the photoenzymatic reactions.
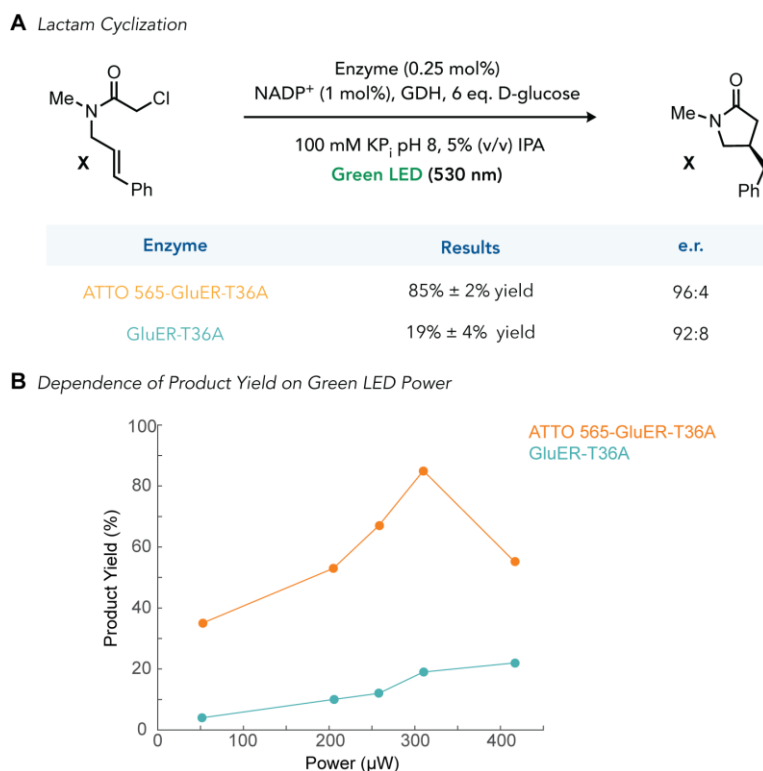
Figure 3.3: Synthetic competency and dependence on LED power. (A) Percent product yield for the lactam cyclization reaction using GluER-T36A and ATTO 565-GluER-T36A at the optimized reaction conditions. (B) Dependence of product yields for the lactam cyclization reaction upon changing LED power.

We also performed reactions under cyan irradiation near the absorption maximum of the

GluER-T36A charge-transfer complex (Figure S3.15, Table S3.7), although the dye absorption

dominates at both excitation wavelengths for the ATTO 565-GluER-T36A conjugate owing to its

larger molar absorption coefficient. Under dim cyan LED irradiation (<2 mW), only trace product

yields were obtained using GluER-T36A, whereas up to 35% yields were obtained using the ATTO

565-GluER-T36A conjugate. Under high power cyan irradiation (152 mW), we obtained higher

yields (52% yield with ATTO 565-GluER-T36A conjugate and 35% yield with GluER-T36A) at

the cost of degradation of the ATTO 565-GluER-T36A conjugate through photo-induced aggregation. We believe photodamage from high-energy irradiation competes with the reaction, lowering the yields. These results establish that low intensity and low photon energy irradiation can be used to obtain synthetically viable yields with the increased light capture provided by the dye.

To evaluate the possibility of performing the intramolecular hydroalkylation under red light irradiation, we examined the performance of the RPE-GluER-T36A conjugate, which has a molar absorption coefficient an order of magnitude larger than the ATTO dyes across the visible spectrum. Under red light irradiation, we obtained 3% product yield using the RPE-GluER-T36A conjugate, enabling photoenzymatic catalysis at even lower-energy wavelengths for the same reactivity. Trace yields were obtained using GluER-T36A alone. We believe this result may increase with further reaction optimization, as the large absorbing strength of the RPE may currently act as an optical filter. Such a strongly absorbing conjugate could lead to high yields with even further reduction of catalyst loading.

This reactivity was extended to other kinds of enzyme-templated charge-transfer states (Figure 3.4). Previously, we reported a hydroalkylation of alkenes that involved an enzyme-templated ternary complex between the flavin cofactor, an α-chloroamide, and an α-methylstyrene.[15] This charge-transfer complex also has an absorption maximum at around 494 nm. Using 0.25 mol% of the ATTO 565-GluER-T36A conjugate, we were able to furnish the alkylated product in 51% yield with trace background reactivity using free GluER-T36A. Although the yield decreased from the original publication (>99% yield), the enantiomeric ratio was unchanged. These results highlight the synthetic usefulness of the enhanced light-harvesting properties of the

ATTO 565-GluER-T36A conjugate (SI Section I-2B), as they allow relatively high yields to be maintained under low energy light with decreased enzyme loading.
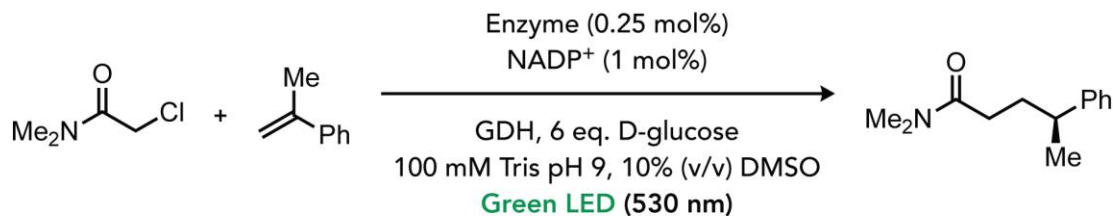
Figure 3.4: Synthetic competency for the intermolecular hydroalkylation reaction. Percent product yields using GluER-T36A and ATTO 565-GluER-T36A at the optimized reaction conditions.

3.3 CONCLUSION

We established a conjugate strategy that increases the efficacy of a synthetic photoenzyme without altering its intrinsic stereoselectivity. Using the modular design of photosynthesis, we introduced a separate light-harvesting system that efficiently transferred energy to the photoenzyme, even with minimal spectral overlap. The introduction of light harvesting led to reactivity under low energy illumination, decreased catalyst loading, and enhanced product yields. The ability to separately optimize and control light capture provides efficient excitation and minimal overlap with substrates or cocatalysts. In future applications, the modularity of this approach will allow a plug-and-play strategy in which the light harvester and photoenzyme can be individually selected for a target reaction in a range of different conditions.

3.4 EXPERIMENTAL SECTION

3.4.1 Sample Preparation

GluER-T36A was prepared using a previously published method, and stored frozen at -20°C. When needed, it was defrosted and buffer exchanged into phosphate buffered saline (PBS, 0.1 M sodium phosphate, 0.1 M sodium chloride, pH = 7.5, filter sterilized and degassed) using centrifugal filtration through 10 kD filters (Millipore, Cat. No. UFC501096). All reactions and spectroscopic studies were performed in PBS. ATTO NHS ester derivatives were purchased from Millipore-Sigma and used as received – ATTO 495 NHS ester (Cat. No. 00379), ATTO 520 NHS ester (Cat. No. 77810), ATTO 565 NHS ester (Cat. No. 72464), and ATTO 590 NHS ester (Cat. No. 79636). Bioconjugation of each respective ATTO-NHS ester to GluER-T36A was performed by reacting GluER-T36A (270 μL of ~23.4 mg/mL [dependent on loss in incurred by centrifugal filtration] in PBS) with ATTO NHS ester (30 μL of 3.3 mg/mL in DMSO, ~6-8x molar excess of dye dependent on identity). Multiple small-scale (300 μL) reactions were performed in parallel to allow ATTO NHS ester to easily react without hydrolysis of the NHS ester. The reaction mixtures were placed on an incubator shaker (300 RPM) at room temperature for 1 h for ATTO 495 and ATTO 520 conjugates or 18 h for ATTO 565 and ATTO 590 conjugates due to their greater hydrophobicity. After incubation, the small-scale reaction mixtures were combined up to 1 mL volume and placed into PD-10 Sephadex G25 desalting columns (Millipore-Sigma, Cat. No. GE17-0851-01) pre-equilibrated with 5 CV (25 mL) PBS. The conjugates eluted first in a visible band, and PBS was continually added to elute the remaining free ATTO dye, roughly until the column was colorless. RPE conjugate crosslinking and analysis procedures are fully described in SI Section II.

3.5 SUPPLEMENTARY INFORMATION

I.   ATTO dye-GluER-T36A Conjugates

Figure S1 shows the chemical structures of the four ATTO dyes used in this study (ATTO 495, ATTO 520, ATTO 565, and ATTO 590, respectively).
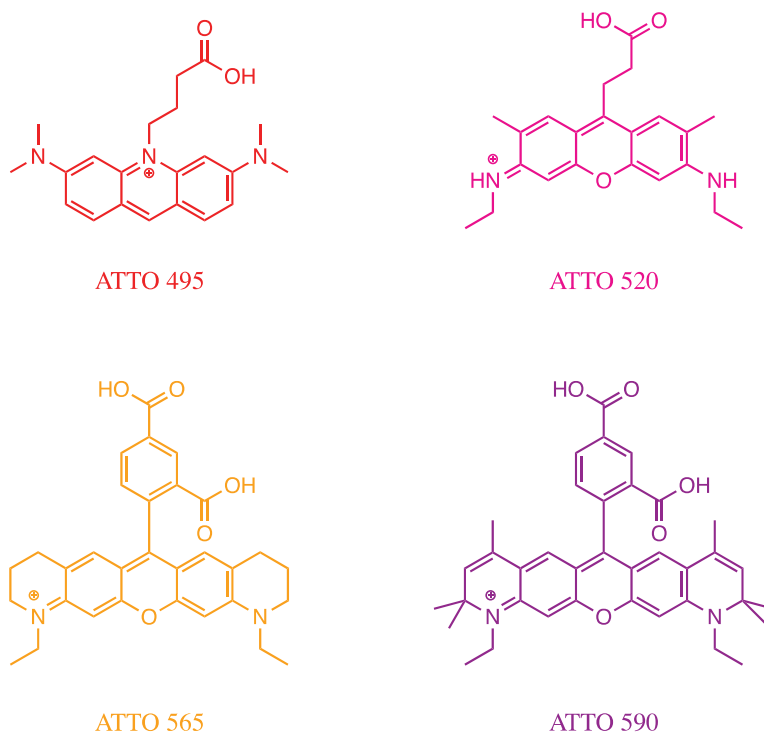
Figure S3.6: ATTO dye chemical structures

1. Determination of Successful Conjugation

C. Intact Mass Spectrometry

GluER-T36A and its ATTO conjugates were loaded onto a Thermo MAbPac RP column using an Agilent1100 HPLC system. MS data was acquired in profile mode with a Thermo QE mass spectrometer at 17,000 resolution, and analyzed using ThermoBioPharma Finder[TM] 3.2 ReSpect with default settings.

The data in Figures S3.2-S3.5 show GluER-T36A compared to the denoted ATTO dye-GluER T36A conjugate. Unmodified GluER T36A exhibited a single strong peak with a mass of 40,034 Da.[220] For the conjugate samples, only peaks with relative abundance >10% were considered in averaging to find the labeling ratio. ATTO 495-GluER-T36A exhibited higher molecular weight peaks spaced every 333 Da with a ratio of 1:0.1:0.25:0.1 representing 4, 5, 6, and 7 ATTO 495 per GluER-T36A, leading to an average labeling ratio of 5 ATTO 495 per GluER-T36A. ATTO 520-GluER-T36A exhibited higher molecular weight peaks spaced every 349 Da with a ratio of 1:0.25:0.1 representing 3, 5, and 8 ATTO 520 per GluER-T36A, leading to an average labeling ratio of 5 ATTO 520 per GluER-T36A. ATTO 565-GluER-T36A exhibited higher molecular weight peaks spaced every 492 Da with a ratio of 0.1:0.3:0.5:1:0.8:0.6:0.3:0.1 representing 2, 3, 4, 5, 6, 7, 8, and 9 ATTO 565 per GluER-T36A, leading to an average labeling ratio of 6 ATTO 565 per GluER-T36A. ATTO 590-GluER-T36A exhibited higher molecular weight peaks spaced every 573 Da with a ratio of 0.9:0.9:1:0.8:0.1 representing 3, 4, 5, 6, and 7 ATTO 565 per GluER-T36A, leading to an average labeling ratio of 5 ATTO 565 per GluER-T36A. These data agree with the findings of UV-vis spectroscopy labeling ratios and are further discussed in the main text.
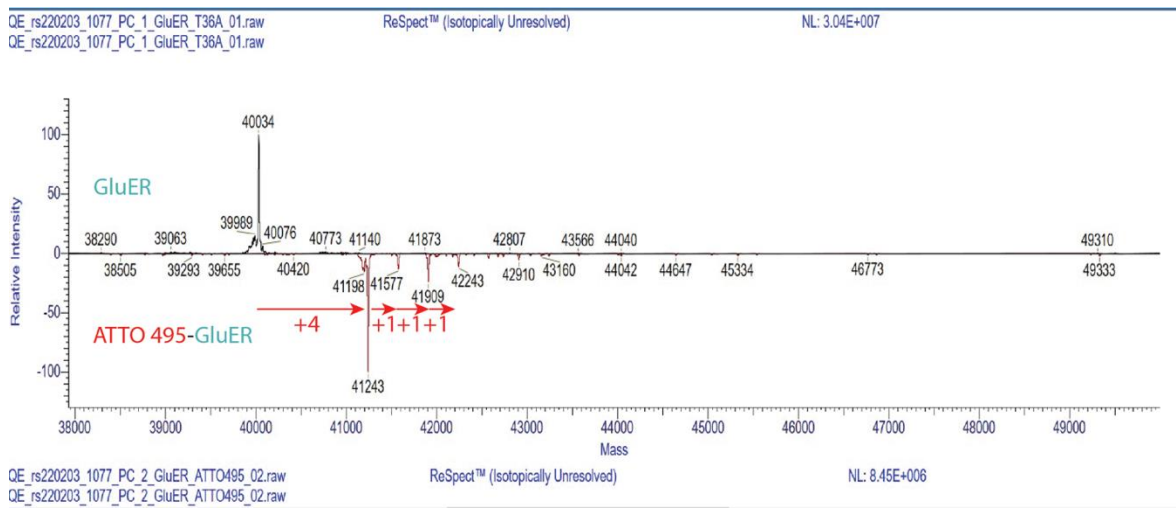
Figure S3.2: Intact MS spectrum of ATTO 495-GluER-T36A compared to GluER-T36A alone.

Figure S3.3: Intact MS spectrum of ATTO 520-GluER-T36A compared to GluER-T36A alone.

Figure S3.4: Intact MS spectrum of ATTO 565-GluER-T36A compared to GluER-T36A alone.

Figure S3.5: Intact MS spectrum of ATTO 590-GluER-T36A compared to GluER-T36A alone.

D. UV-Visible Absorption, Relative Stability, and Steady State Fluorescence Experiments

Linear absorbance spectra were acquired using an Agilent Cary 5000 UV-vis-NIR spectrophotometer. Fluorescence emission spectra were obtained using a Varian Cary Eclipse with excitation at the maximum absorbance of the respective ATTO dye. All spectra were acquired at room temperature in PBS using a 10 mm x 2 mm path length quartz cuvette (Hellma Analytics 108.002F-QS). Due to the change in the molar absorption coefficient of the ATTO dyes upon conjugation, labeling ratios were determined by calculating the amount of reacted dye from UV-visible absorption spectroscopy. This is performed by subtracting the amount of leftover dye (diluted in PBS from the remaining dye stock after size exclusion chromatography to an A ≤ 0.04 at 1 cm path length to eliminate as much aggregation as possible) from the amount of deployed dye (diluted from the DMSO stock in acidified ethanol – 0.1% v/v trifluoroacetic acid in ethanol – to prevent aggregative affects) and then dividing this by the amount of reacted protein (diluted from the stock in PBS). We obtained labeling ratios of 9, 5, 2, and 4 for ATTO 495, 520, 565, and 590 conjugates of carbonic anhydrase and labeling ratios of 8, 4, 2, and 3 for ATTO 495, 520, 565, and 590 conjugates of GluER-T36A, respectively. An absorption spectrum of the charge-transfer state of GluER-T36A is shown in Figure S3.7.
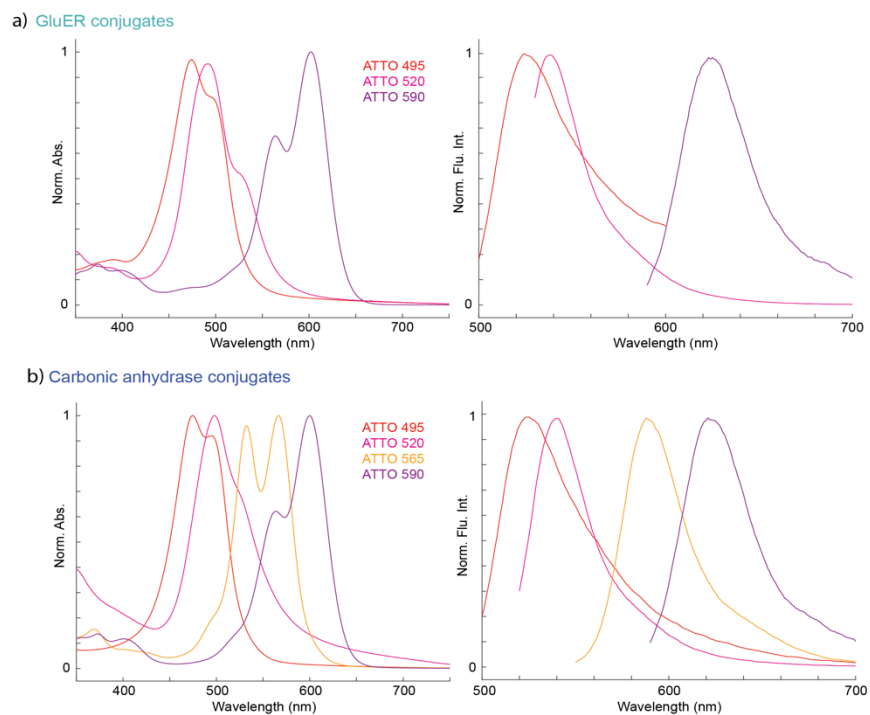
Figure S3.6: Steady-state spectra of conjugates. UV-visible absorption spectra and fluorescence spectra of (a) ATTO 495, ATTO 520, and ATTO 590-GluER-T36A conjugates and (b) ATTO 495, ATTO 520, ATTO 565, and ATTO 590-Carbonic Anhydrase conjugates.
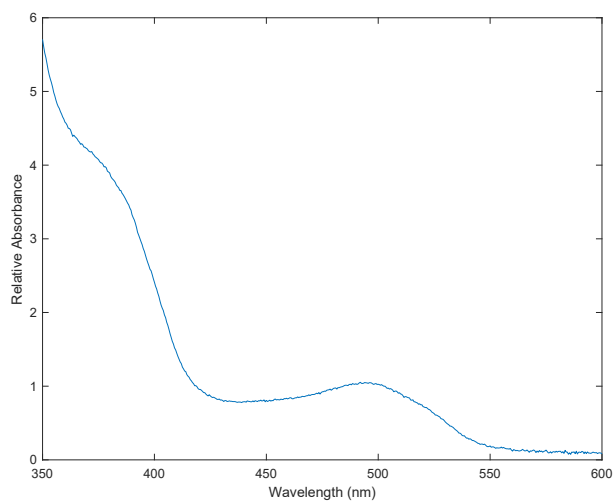
Figure S3.7: Normalized absorption spectrum of the photoactive charge-transfer state of GluER-T36A.

Relative Stability Experiments for ATTO 565-GluER-T36A

We monitored the UV-visible absorption spectrum of the ATTO 565-GluER-T36A conjugate over time to determine its relative stability under maximum green LED intensity with stirring set at 200 RPM. This provides a lower limit to the stability of the conjugate over time, as we used lower intensity light in the test reactions. ATTO dye-GluER T36A samples remained in the cuvette throughout the experiment, and UV-vis absorption spectra were obtained at 0 h (before any irradiation), 3 h, 6 h, 9 h, and 24 h. We performed spectral decomposition to analyze the photodegradation and scattering components for each time point, as follows:

$$A_{Xh}(\lambda) = X(A_{0h}(\lambda)) + \log_{10}\frac{1}{1 - C\lambda^{-1}} + \log_{10}\frac{1}{1 - D\lambda^{-4}}$$

where the first term represents the amount of photodegradation and the second two terms represent the amount of scattering.[173] A_{Xh} is the absorption at t>0 h, A_{0h} is the initial spectrum, X represents the fraction of the initial spectrum present at t>0 h, and C and D are constants used to capture the scattering component. We consider the percent remaining of the initial spectrum to be a reporter of photodegradation, and the amount of scattering in each spectrum at Xh to be a reporter of scattering. Table S3.1 provides stability data after 24 h for varying green LED power.

Table S3.1: Relative stability of ATTO 565-GluER-T36A under green LED irradiation.		
LED power (mW)	% of initial spectrum remaining at 24 h	% scatter at 24 h
52	76	6
205	70	1
310	66	2
417	58	4

2. FRET Calculations

A. Determination of Number of Surface-Accessible Lysines and Relevant Distances

The number of surface accessible lysine residues within 2.5 Å^2 for GluER-T36A (PDB: 6MYW[220]) was identified using the open source findSurfaceResidues in Pymol. A total of 15 accessible lysine residues were found and are shown in Figure S8. Centroid to centroid distances for the flavin cofactor and accessible lysine residues were also determined (Table S3.2). Flavin-ATTO dye distances were determined by adding the flavin-lysine distances determined above to the lysine-ATTO dye distance, assumed as 6 Å.

The findSurfaceResidues script was also used to identify the 18 accessible lysine residues present in carbonic anhydrase from bovine erythrocytes (PDB: 1V9E[221], purchased from Millipore-Sigma Cat. No. C7025).

Table S3.2: GluER T36A Flavin-Lysine Distances	
Lys Num.	Distance (Å)
1	11.5
2	15
3	16.3
4	16.5
5	18.6
6	20
7	21
8	22.3
9	22.3
10	23.1
11	23.6
12	24.9
13	25.4
14	25.8
15	26
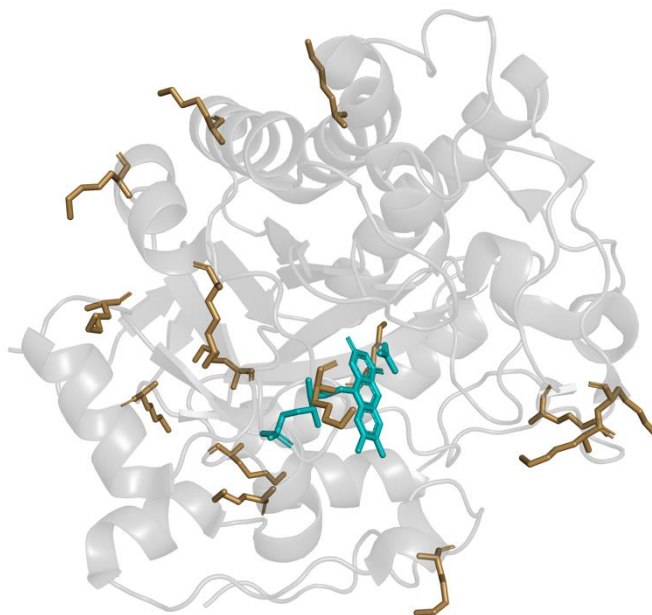
Figure S3.8: GluER-T36A accessible lysine residues. Accessible lysine residues are shown in gold, and the flavin cofactor is shown in teal.

B. FRET Rate Calculations:

We performed Förster Resonance Energy Transfer (FRET) calculations to estimate the energy transfer rate between ATTO dyes and GluER-T36A. Here, the ATTO dyes represent the donor, D, and the flavin represents the acceptor, A. FRET is the non-emissive excitation of A by an excited D, shown below[44]:
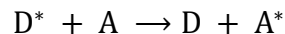
$$D^* + A \longrightarrow D + A^*$$

The FRET rate equation is:

$$k_{ET}(r) = \frac{1}{\tau_D}\left(\frac{R_0}{r}\right)^6$$

where $k_{ET}(r)$ is the energy transfer rate, τ_D is the natural emissive lifetime of the donor, r is the donor-acceptor distance, and R_0 is the Förster distance, described by the equation:

$$R_0^6 = Q_D \kappa^2 \frac{9000\,(\ln 10)}{128\,\pi^5\,N\,n^4}\,J$$

where Q_D is the natural quantum yield of the donor, κ is a factor describing the spatial orientation of the transition dipoles (assumed here to be isotropic, $\kappa^2 = 2/3$), N is Avogadro's number (6.022 x 10^{23} mol^{-1}), n is the refractive index of the medium (1.33 for water), and J is the spectral overlap integral of the donor and acceptor, given by:

$$J = \int_0^\infty F_D(\lambda)\varepsilon_A(\lambda)\lambda^4 d\lambda$$

where $F_D(\lambda)$ is the area-normalized fluorescence spectrum of the donor, $\varepsilon_A(\lambda)$ is the molar absorption coefficient of the acceptor, and λ includes the overlap wavelength range. The donor lifetimes were measured on the ATTO-Carbonic Anhydrase conjugates (Table S3.4) for the ATTO 520, 565 and 590 samples. The ATTO 495 conjugate lifetimes were not able to be measured. Donor emission spectra are provided on the supplier's website (ATTO-TEC). We performed two sets of calculations – one where the donor excites the oxidized flavin, relevant to the fluorescence lifetime measurements performed, and one where the donor excites the GluER-T36A charge-transfer state, relevant to the test reactions. The GluER-T36A oxidized flavin absorption spectra were obtained, and the GluER-T36A oxidized flavin molar absorption coefficient of 11,400 M^{-1}cm^{-1} was obtained from a previously published value.[220] J was found to be 1.43 x 10^{14} nm^4 M^{-1} cm^{-1} for ATTO 495, 9.99 x 10^{13} nm^4 M^{-1} cm^{-1} for ATTO 520, 9.76 x 10^{13} nm^4 M^{-1} cm^{-1} for ATTO 565, and 1.11 x 10^{14} nm^4 M^{-1} cm^{-1} for ATTO 590. We quantified the percent of the GluER-T36A absorption spectrum that overlaps with the ATTO dye emission spectra by integrating both the spectral overlap region and the full absorption spectrum with respect to wavelength and taking a ratio of these two values. The spectral overlap region represents 0.039% of the absorption spectrum for the ATTO 495 conjugate, 0.027% for the ATTO 520 conjugate, 0.027% for the ATTO 565 conjugate, and 0.030% for the ATTO 590 conjugate. R_0 was found to be 26.6 Å for ATTO 495, 32.2 Å for ATTO 520, 32.1 Å for ATTO 565, and 32.2 Å for ATTO 590. The GluER-T36A charge-transfer state absorption

101

spectra were obtained previously,[220] and the GluER-T36A charge-transfer state molar absorption coefficient of 3,600 $M^{-1}cm^{-1}$ was obtained from a previously published value.[222,223] The FRET overlap is shown in Figure S3.9 for ATTO 565 and the GluER-T36A charge-transfer state. J was found to be 1.00 x 10^{14} nm^4 M^{-1} cm^{-1} for ATTO 495, 8.08 x 10^{13} nm^4 M^{-1} cm^{-1} for ATTO 520, 4.04 x 10^{13} nm^4 M^{-1} cm^{-1} for ATTO 565, and 3.95 x 10^{13} nm^4 M^{-1} cm^{-1} for ATTO 590. R_0 was found to be 25.1 Å for ATTO 495, 31.1 Å for ATTO 520, 27.7 Å for ATTO 565, and 27.1 Å for ATTO 590. Representative single donor-single acceptor efficiency and timescale graphs are shown for ATTO 565-GluER-T36A in Figures S3.10 and S3.11 for the charge-transfer state as the acceptor.

The individual FRET rates for all 15 possible ATTO dye-GluER-T36A flavin distances were determined. One of these rates was chosen at random and used to calculate the FRET rate, k_{ET}. As these are multi donor-single acceptor systems, only one donor per complex is likely to be excited at a given time.[176,224] This process was repeated 100x and averaged to obtain the predicted ensemble energy transfer timescales and efficiencies. For the oxidized flavin state, the energy transfer timescales were 2.49 ns for ATTO 495, 3.27 ns for ATTO 520, 2.30 ns for ATTO 565, and 2.83 ns for ATTO 590, which then provided the predicted ensemble FRET efficiencies of 34% for ATTO 495, 72% for ATTO 520, 74% for ATTO 565, and 71% for ATTO 590. For the charge-transfer state, the energy transfer timescales were 0.889 ns for ATTO 495, 0.519 ns for ATTO 520, 0.855 ns for ATTO 565, and 0.785 ns for ATTO 590, which then provided the predicted ensemble FRET efficiencies of 42% for ATTO 495, 68% for ATTO 520, 55% for ATTO 565, and 51% for ATTO 590. Energy transfer is calculated using the below equation.

$$E_{ET} = \frac{k_{ET}}{k_{ET} + \dfrac{1}{\tau_D}}$$

The absorption spectrum of Carbonic Anhydrase is shown in Figure S3.12. It contains only A_{280} and A_{215} contributed by amino acids (non-chromophoric), and tapers to baseline by 350 nm. Therefore, the spectral overlap integral, J, is predicted to be negligible, and there is no acceptor to excite, so FRET to Carbonic Anhydrase is assumed null.
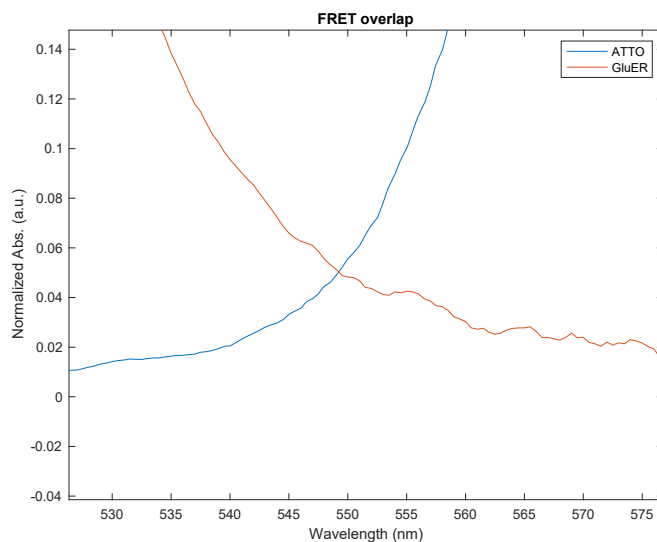
Figure S3.9: FRET overlap. The overlap of the absorption spectrum of the charge-transfer state of GluER-T36A and the fluorescence spectrum of ATTO 565.
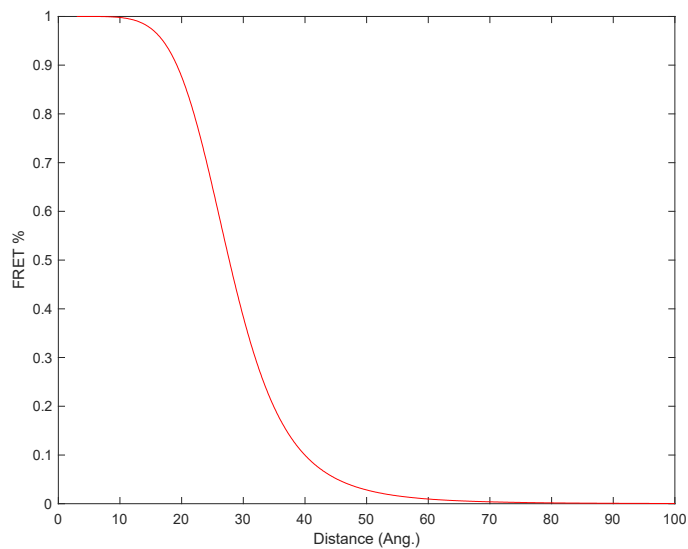
Figure S3.10: FRET efficiency % for ATTO 565-GluER-T36A.
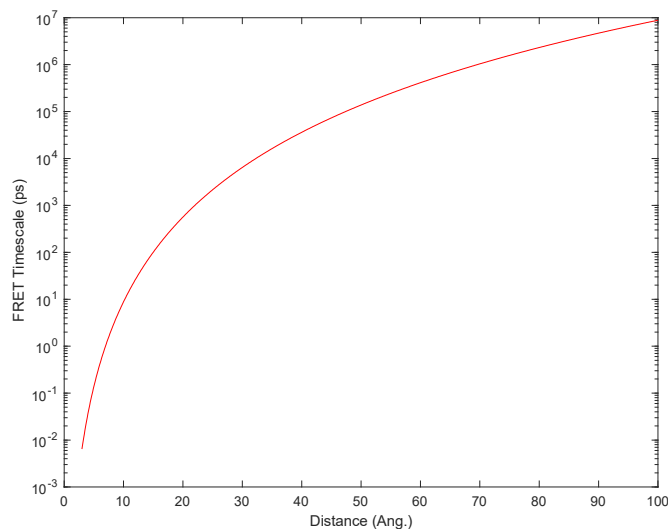
Figure S3.11: FRET timescale for ATTO 565-GluER-T36A.
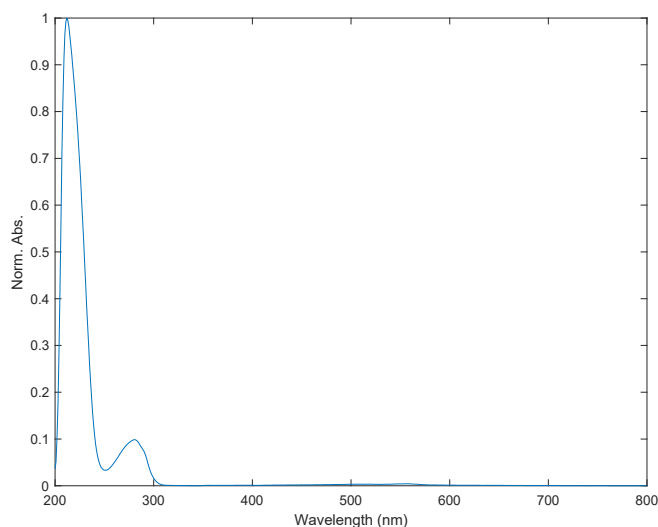
Figure S3.12: Absorption spectrum of carbonic anhydrase.

C. Determination of Energy Transfer - Fluorescence Lifetime Experiments

Fluorescence lifetime measurements were performed on a Spectra Physics Mai Tai Ti:sapphire laser. The laser output (centered at 800 nm, 6 nm FWHM, 80 MHz repetition rate) was converted to a broadband supercontinuum (430-1000 nm) through the use of a nonlinear photonic crystal fiber (FemtoWhite 800, NKT Photonics). The excitation wavelength was selected dependent on the ATTO dye using a 520 nm, 10 nm FWHM bandpass filter (ThorLabs FB520-10, ATTO 520),

550 nm, 15 nm FWHM bandpass filter (Chroma Technology Corp ET550/15x, ATTO 565), and 580 nm, 10 nm FWHM bandpass filter (ThorLabs FB580-10, ATTO 590). The emission wavelength was selected dependent on the ATTO dye using a 550 nm, 15 nm FWHM bandpass filter (Chroma Technology Corp ET550/15x, ATTO 520), 580 nm, 10 nm FWHM bandpass filter (Thor Labs FB580-10, ATTO 565), and 600 nm, 10 nm FWHM bandpass filter (ThorLabs FB600-10, ATTO 590). Filter overlaps with the free ATTO dye absorption and emission spectra are shown in Figure S3.13. Emitted signal was detected with an avalanche photodiode (PDM Series, Micro Photon Devices) and arrival times were recorded by a time-correlated single photon counting module (PicoHarp 300, PicoQuant Inc.). The excitation laser pulse was focused on a 1 cm x 2 mm pathlength quartz cuvette (Hellma Analytics 108.002F-QS) to a spot size of 0.66 μm^2 and with a pulse energy of 1.37 pJ per pulse for the 460 nm excitation filter, 2.46 pJ per pulse for the 520 nm excitation filter, 6.66 pJ per pulse for the 550 nm excitation filter, and 5.48 pJ per pulse for the 580 nm excitation filter. The fluorescence intensity of the samples was monitored to ensure that no photodegradation occurred during the experiment. The instrument response function (IRF) was measured using Ludox HS-40 colloidal silica (Sigma-Aldrich) and determined to be within 100 ps FWHM for all filter setups.

Fluorescence lifetime decay curves were individually fitted to stretched mono- or mono-exponential functions using iterative reconvolution with the IRF. The fitted lifetime intensities were of the general form $I(t) = W + A\,e^{-(t/\tau)^{\beta}}$, where W is a baseline offset term, A is the amplitude, τ is the time constant, t is the time, and I(t) is the intensity as a function of time. β is an empirical term valued between zero and one which describes stretched mono-exponential functions ($\beta = 1$ returns a mono-exponential function). Stretched mono-exponential functions are employed to describe distributions of closely valued decays, as would be expected for energy

transfer among a collection of identical chromophores. The fitted parameters are summarized in

Tables S3.3, S3.4, and S3.5.
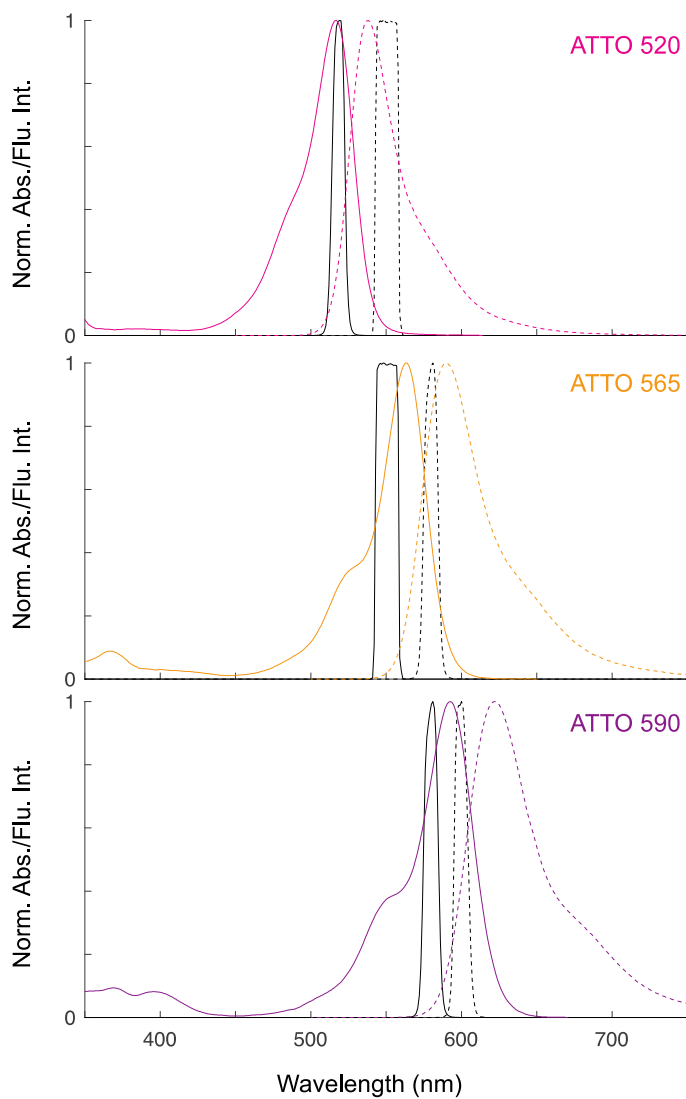
Figure S3.13: Excitation and emission filter overlap. Denoted unconjugated ATTO dye absorption (solid) and emission (dashed) spectra overlaid with the excitation (black, solid) and emission (black, dashed) filters used in TCSPC.

Table S3.3: Fitted parameters for ATTO-GluER (3 replicates).				
	Offset	**A**	τ	**β**
ATTO 520-GluER-T36A				
average	*-0.650*	*1*	*2.300*	*0.743*
standard deviation	*0.152*	*0*	*0.553*	0.083
ATTO 565-GluER-T36A				
average	*-0.259*	*1*	*0.630*	*0.482*
standard deviation	*0.038*	*0*	*0.383*	0.088
ATTO 590-GluER-T36A				
average	*-0.245*	*1*	*0.985*	*0.574*
standard deviation	*0.171*	*0*	*0.211*	0.023

Table S3.4: Fitted parameters for ATTO-Carbonic Anhydrase (3 replicates).				
	Offset	**A**	τ	**β**
ATTO 520-Carbonic Anhydrase				
average	*-0.257*	*1*	*3.821*	*N/A*
standard deviation	*0.144*	*0*	*0.048*	*N/A*
ATTO 565-Carbonic Anhydrase				
average	*0.316*	*1*	*3.749*	*N/A*
standard deviation	*0.454*	*0*	*0.236*	*N/A*
ATTO 590-Carbonic Anhydrase				
average	*0.494*	*1*	*3.603*	*N/A*
standard deviation	*0.062*	*0*	*0.030*	*N/A*

Table S3.5: Fitted parameters for ATTO dyes (3 replicates).				
	Offset	**A**	τ	**β**
ATTO 520				
average	*-0.537*	*1*	*3.800*	*N/A*
standard deviation	*0.033*	*0*	*0.022*	*N/A*
ATTO 565				
average	*-0.001*	*1*	*3.783*	*N/A*
standard deviation	*0.035*	*0*	*0.029*	*N/A*
ATTO 590				
average	*-0.442*	*1*	*4.061*	*N/A*
standard deviation	*0.040*	*0*	*0.034*	*N/A*

3. Synthetic Reactions

A. General information

Reagents: All commercial reagents and buffer salts were used as received without further purification. All reactions were prepared and run in an MBraun LABstar Pro Glovebox Workstation. Buffers and solvents were freeze-pump-thawed prior to being brought into the glovebox. GluER-T36A and ATTO dye-GluER-T36A conjugates were degassed in a water saturated cold box inside the glovebox prior to use. If not bought, substrates and product standards were obtained using previously reported methods.[220,225] All spectra matched the literature values. GluER-T36A was expressed and purified using previously reported methods.[220]

The photoenzymatic reactions were performed in a recrystallization dish lined a single time with 3528 SMD RGB LED strip lights connected to a 12V 5A power supply. One 750 μL shell vial was affixed to the recrystallization dish right in front of the green LED. The reactions were set up in PCR tubes placed in the vial such that the light shined directly. The reactions were shaken at the 3.5 setting on a Titer plate shaker from Lab Line Instruments. A fan was placed on top of the recrystallization dish to minimize protein degradation due to heat.

Assay yields were obtained using a calibration curve using 1,3,5-tribromobenzene as an internal standard.

B. Lactam Cyclization[220]
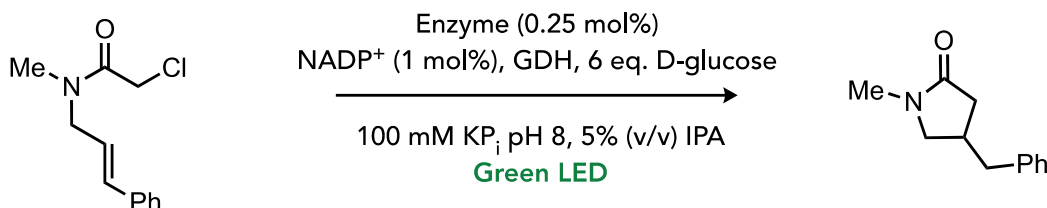
The amide, NADP+, GDH and glucose were weighed outside of the glove box and brought in along with PCR tubes. The PCR tube was "charged" with 6 equivalents of glucose in dissolved in

100 mM KP$_i$ pH 8 such that the final concentration of the substrate after all the reagents were added was 18 mM. A 10 mg/mL stock solution of GDH was made using 100 mM KP$_i$ pH 8 and 5 μL of this solution was added to the PCR tube. A 5 mg/mL stock solution of NADP$^+$ was made using 100 mM KP$_i$ pH 8 and 1.34 μL of this solution was added to the PCR tube. Then 0.25 mol% of GluER-T36A or the ATTO dye-GluER-T36A conjugate was added. A 0.2 mg/2uL (0.9 μmol) solution of the substrate was made using isopropanol and 2 μL was added to the PCR tube. The PCR tube was capped and placed in a quarter dram shell vial in the recrystallization dish. It was then irradiated with green LEDs on the 3rd brightest LED setting (power = 310 mW) for 48 hours with shaking and a fan placed on top (Figure S3.14, left).

When screening the brightness levels of the LED, the above procedure was used and the brightness was changed accordingly using the remote provided with the LED strip. The five brightness levels reported are level 1 (52 mW, minimum), level 4 (205 mW), level 5 (258 mW), level 6 (310 mW, optimized conditions), and level 8 (417 mW, maximum).

The above protocol was also used for reactions irradiated with cyan LED light, but the reaction was placed in a one dram shell vial and capped with a septa to ensure anaerobic conditions outside the glove box. These reactions were not shaken, but optimization showed shaking had minimal effect. The setup consisted of a cyan LED light source (50 W Chanzon high-power LED chip, 490 nm) placed 10 cm from the reaction vessel and a fan to ensure room temperature (Figure S3.14, right). For reactions performed at reduced intensity, the vessel was surrounded by a box built of neutral density (ND) absorptive filters and cardboard to modulate intensity and prevent stray light from entering. The four brightness levels reported are ND = 2.7 (0.3 mW), ND = 2 (1.5 mW), ND = 1.9 (2 mW), and the unshielded LED (152 mW) (Figure S3.15).

After the reaction was completed, the protein was crashed out with 300 μL of acetonitrile and 25 μL of a 2 mg/mL solution of 1,3,5-tribromobenzene was added as an internal standard. Yields were then analyzed by calibration curve using an LC-MS (Figure S3.16). To confirm the enantiomeric ratio, four reactions were pooled together and diluted with water and extracted with equal volume of ethyl acetate twice. The ethyl acetate was removed *in vacuo* and the crude residue was resuspended in 1:1 IPA/hexanes. This solution was passed through a filter and a sodium sulfate plug and subjected to Chiral HPLC analysis using a 20% IPA in hexanes method on the AS-H column from ChiralPak.

Figure S3.14: Reaction setups. Green LED (left) and cyan LED (right).
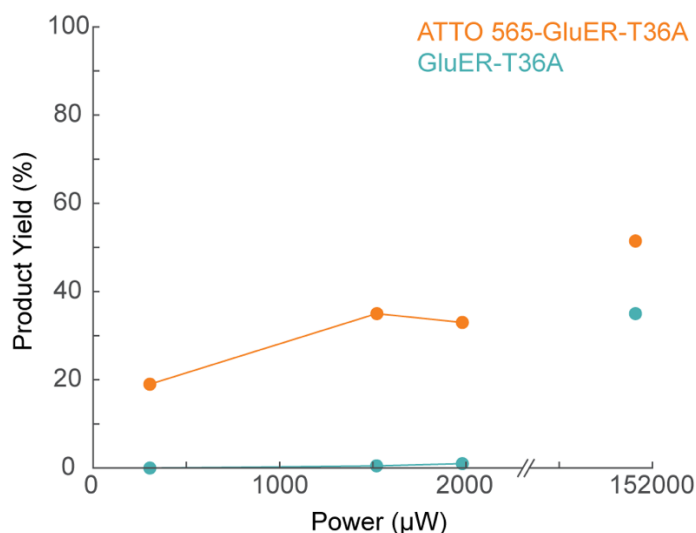
Figure S3.15: Product yields under cyan LED irradiation. Product yields for the lactam cyclization reaction at varying intensity of cyan LED light.
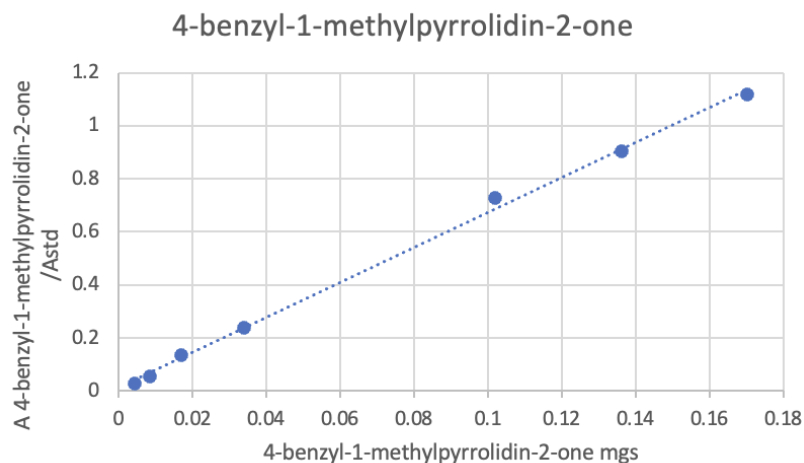
Figure S3.16: Yield calibration curve.

Table S3.6: Product yields for the lactam cyclization reaction under green LED irradiation.		
LED power (mW)	Yield using ATTO 565-GluER-T36A Conjugate (%)	Yield using GluER-T36A (%)
52	35	4
205	53	10
258	67	12
310	85 ± 2 (e.r. 96:4)	19 ± 4 (e.r. 92:8)
417	55	22

Table S3.7: Product yields for the lactam cyclization reaction under cyan LED irradiation.		
LED power (mW)	Yield using ATTO 565-GluER-T36A Conjugate (%)	Yield using GluER-T36A (%)
0.3	19	0
1.5	35	0.5
2	33	1
152	52	35

Chiral HPLC Traces:
Racemic:

#	Time	Type	Area	Height	Width	Area%	Symmetry
1	25.507	MM	316.4	7.6	0.6947	49.970	1.047
2	28.532	MM	316.8	6.8	0.7718	50.030	1.012
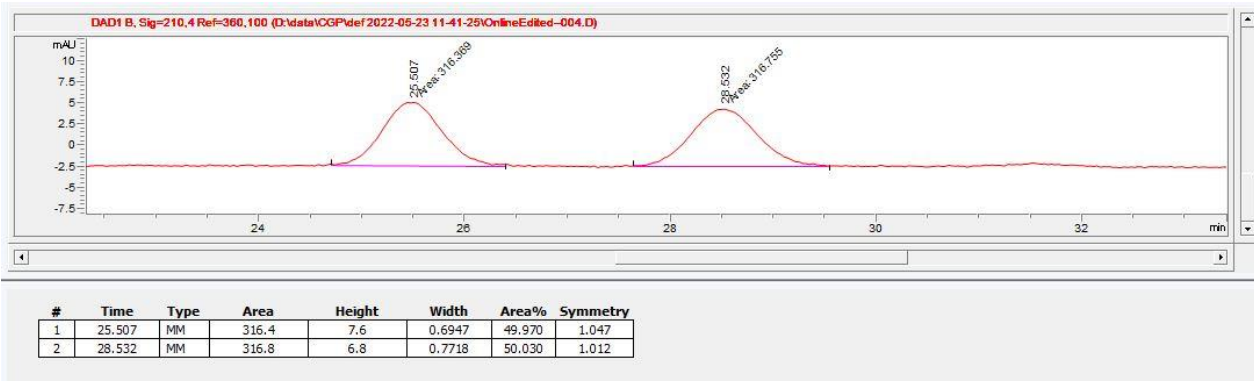
With 0.25 mol% GluER T36A-ATTO 565

#	Time	Type	Area	Height	Width	Area%	Symmetry
1	24.921	BB	49107.4	929.9	0.7901	95.732	0.405
2	28.515	BB	2189.4	47.6	0.681	4.268	0.848

With 0.25 mol% GluER T36A:

#	Time	Type	Area	Height	Width	Area%	Symmetry
1	26.877	PP	9226.6	202.2	0.7606	92.120	0.699
2	30.262	MM	789.3	16.5	0.7977	7.880	0.882
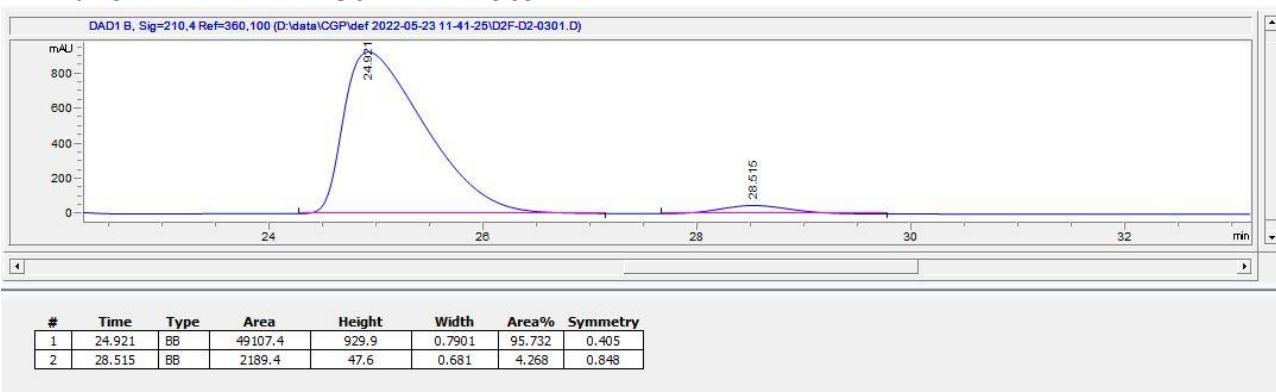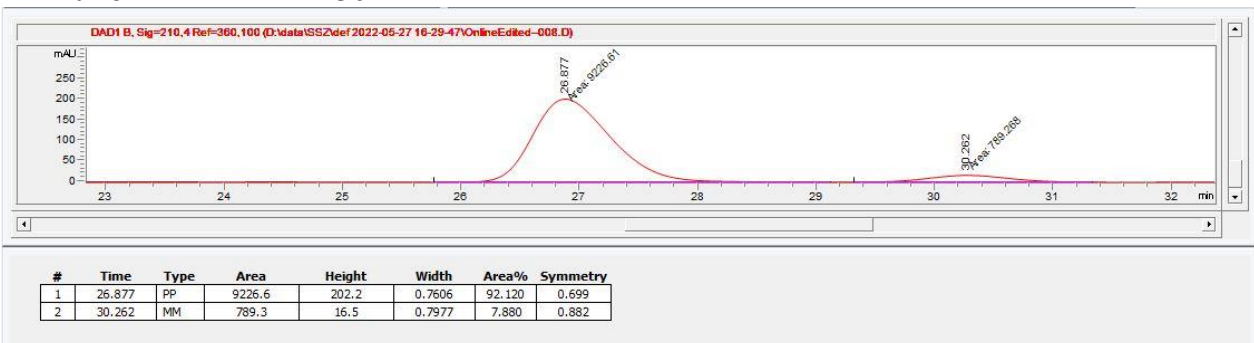
C. Intermolecular hydroalkylation of alkenes[225]
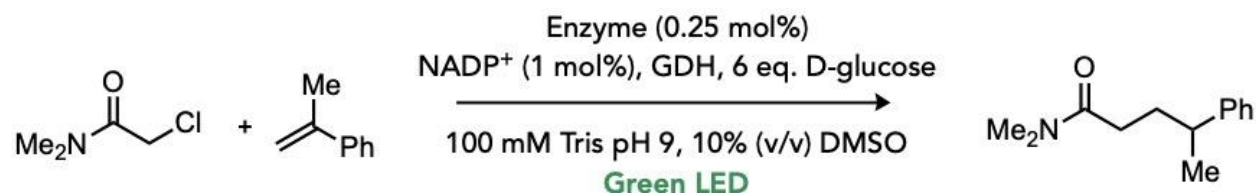
The α-chloroamide, α-methylstyrene, NADP+, GDH and glucose were weighed outside of the glove box and brought in along with PCR tubes. The PCR tube was "charged" with 6 equivalents of glucose dissolved in 100 mM Tris pH 9 such that the final concentration of the substrate after all the reagents were added was 27 mM. A 10 mg/mL stock solution of GDH was made using 100 mM Tris pH 9 and 5 μL of this solution was added to the PCR tube. A 5 mg/mL stock solution of NADP$^+$ was made using 100 mM Tris pH 9 and 1.34 μL of this solution was added to the PCR tube. Then 0.25 mol% of GluER-T36A or the ATTO dye-GluER-T36A conjugate was added. A 0.1 mg/1.5uL (0.9 μmol) solution of the α-chloroamide was made using DMSO and 1.5 uL was added to the PCR tube. A 0.372 mg/1.5 μL (3.5 equivalents) solution of α-methylstyrene was made using DMSO and 1.5 μL was added to the PCR tube. The PCR tube was capped and placed in the quarter dram shell vial in the recrystallization dish. It was then irradiated with green LEDs on the 3rd brightest LED setting for 48 hours with shaking and a fan placed on top.

After the reaction was completed, the protein was crashed out with 300 μL of acetonitrile and 25 μL of a 2 mg/mL solution of 1,3,5-tribromobenzene was added as an internal standard. Yields were then analyzed by calibration curve using an LC-MS (Figure S17). To confirm the enantiomeric ratio did not change, four reactions were pooled together and diluted with water and extracted with equal volume of ethyl acetate twice. The ethyl acetate was removed *in vacuo* and the crude residue was resuspended in 1:1 IPA/hexanes. This solution was passed through a filter

and a sodium sulfate plug and subjected to Chiral HPLC analysis using a 2% IPA in hexanes method on the OD column from ChiralPak.
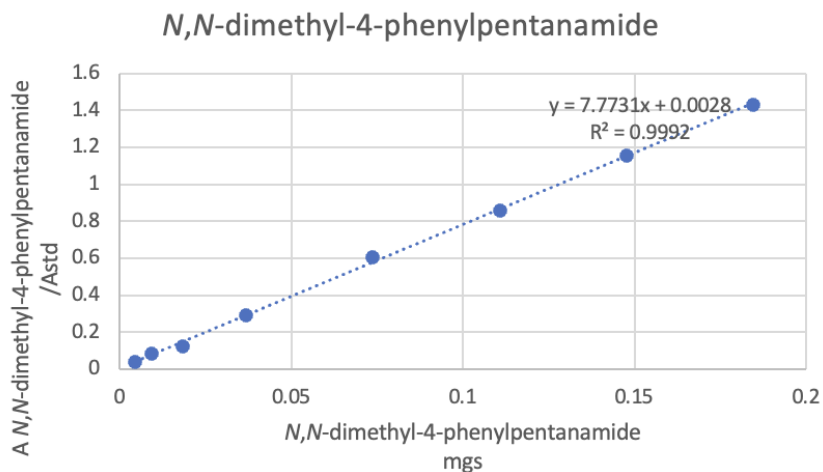
Figure S3.17: Yield calibration curve.

Yields:

GluER T36A-ATTO 565 conjugate:
Yield: 51 ± 1 % yield
Enantiomeric Ratio: 99:1

GluER T36A
Yield: <1 % yield
Enantiomeric Ratio: n.d.

Chiral HPLC Traces:

Racemic:

#	Time	Type	Area	Height	Width	Area%	Symmetry
1	17.723	MM	3440.1	72	0.7961	50.295	0.498
2	22.371	MM	3399.8	56.8	0.9974	49.705	0.497

With GluER T36A-ATTO 565

DAD1 B, Sig=210,4 Ref=360,100 (D:\data\SSZ\def 2022-05-25 14-54-40\OnlineEdited-025.D)

#	Time	Type	Area	Height	Width	Area%	Symmetry
1	18.435	MM	9008.4	180.5	0.8318	98.862	0.472
2	23.301	PM	103.7	2.4	0.7247	1.138	0.927
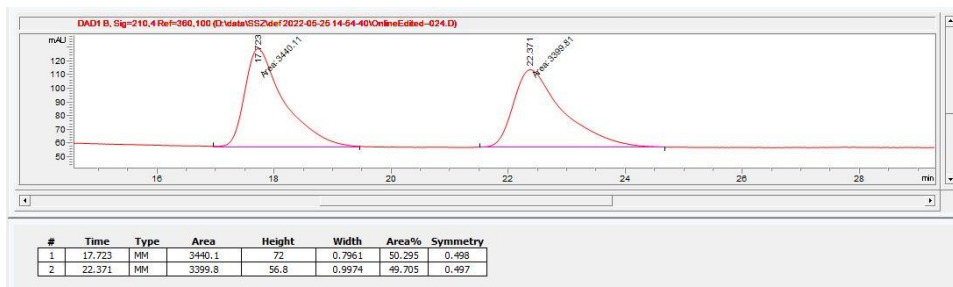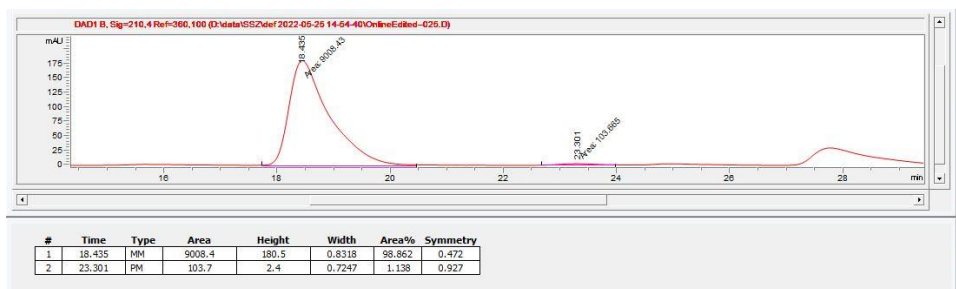
II.   RPE-GluER-T36A Conjugates

1. Construction and Purification of RPE-GluER-T36A

All reactions and spectroscopic studies were performed in Phosphate Buffered Saline (PBS; 0.1 M sodium phosphate, 0.1 M sodium chloride, pH = 7.5, filter sterilized and degassed). R-phycoerythrin (RPE; Agilent Cat. No. PB-32) was kept at 4°C until needed, at which time it was buffer exchanged into PBS by centrifugal filtration through 50 kD centrifugal filters (Millipore) to a final concentration of 11.75 mg/mL and volume of 500 μL. Immediately before reacting, we prepared a 275 mM solution of Pierce N-succinimidyl-S-acetylthioacetate (SATA, ThermoFisher Cat. No. 26102). The RPE was reacted with 15 μL Pierce SATA solution (168x molar excess) for 30 m, room temperature, shaking at 300 RPM on an incubator shaker. The reaction mixture was buffer exchanged to PBS via centrifugal filtration to remove any unreacted Pierce SATA. Then, it was immediately diluted to 5 mL and combined with 2 mL deacetylation solution (0.5 M hydroxylamine, 25 mM EDTA in PBS) for 2 h at room temperature and rocked. This reaction modifies the lysine residues of RPE to exhibit thiols. Before reaction with GluER-T36A, the RPE product was rapidly buffer exchanged back into PBS buffer through centrifugal filtration.

GluER-T36A was prepared using a previously published method,[220] and kept frozen at -20°C. When needed, ~1 h before the end of the deacetylation of RPE, roughly 25 nmol (batch dependent)

was defrosted and buffer exchanged into PBS using centrifugal filtration through 10 kD filters (Millipore, Cat. No. UFC501096). GluER-T36A was then diluted to a volume of 1 mL. Just before reaction, a 25 mM solution of succinimidyl iodoacetate (SIA, ThermoFisher Cat. No. 22349) was prepared. The following procedure was performed in the dark to prevent photodegradation of SIA. The 1 mL GluER-T36A was reacted with 50 μL SIA solution (50x molar excess) for 30 m at room temperature in PBS on an incubator shaker at 300 RPM. This reaction modifies the lysines of GluER-T36A to exhibit iodo groups. Then, GluER-T36A was buffer exchanged into PBS via centrifugal filtration.

The following procedure was also performed in the dark. 800 μL modified RPE and 200 μL modified GluER-T36A were combined and reacted together for 75 m at room temperature on an incubator shaker at 300 RPM. The reaction mixture was purified first through multiple centrifugal filtrations in 50 kD centrifuge tubes to remove any unreacted GluER-T36A. Then, the reaction mixtures were placed in Ni-NTA columns, and allowed to equilibrate onto the column overnight. The His tag appended to the GluER-T36A binds to the column, but unreacted RPE will not. Then, unreacted RPE was eluted through the column using 9 CV wash buffer (PBS), and successive buffers with increasing amounts of imidazole (3 CV 20 mM imidazole in PBS, 3 CV 100 mM imidazole in PBS, and 3 CV 400 mM imidazole in PBS) released the RPE-GluER-T36A product(s). An SDS-PAGE fluorescent gel image is shown in Figure S3.18, showing high-mass (>75 kD) product bands appearing in the imidazole eluents.
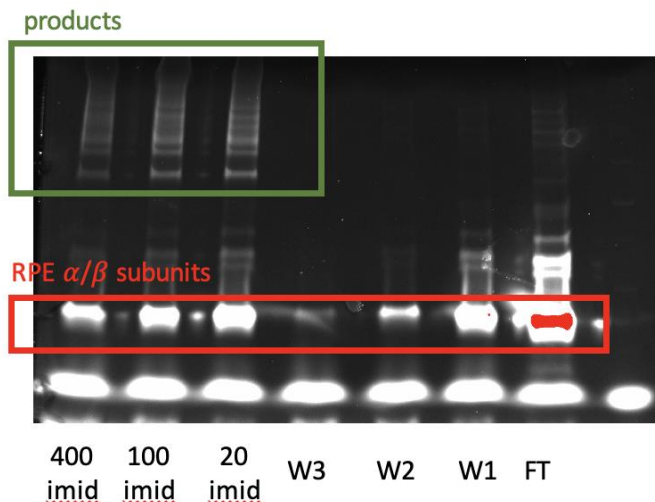
Figure S3.18: Fluorescent gel image of RPE-GluER-T36A during Ni:NTA purification.

2. Determination of Successful Conjugation and Stability Experiments

UV-visible absorption spectroscopy and steady-state fluorescence spectroscopy were obtained using the same instrumentation and cuvettes as described for ATTO dye-GluER-T36A conjugates in PBS. Figure S3.19 shows the UV-visible absorption spectra of 2 RPE-GluER-T36A samples overlaid with the spectra of RPE and GluER-T36A. A 1:3 eq simple mixture spectra is also shown with good agreement to the conjugate, indicating successful conjugation and easily determining the labeling ratio. The spectra could also be fit using linear decomposition of the component spectra. The conjugate was also visibly colored pink after Ni-NTA chromatography, and exhibited fluorescence characteristic of RPE (Figure S3.19), indicative of successful conjugation.
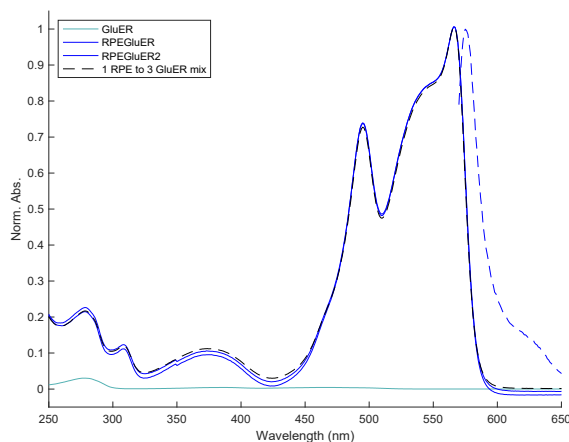
Figure S3.19: Steady-state measurements. UV-vis absorption spectra of RPE-GluER-T36A (solid blue), GluER-T36A (teal), and a simple mixture (dashed black). An emission spectrum of RPE-GluER-T36A is also shown in dashed blue.

Stability experiments on RPE-GluER-T36A

RPE-GluER-T36A was examined for stability over 24 h using the same procedure as described for ATTO 565-GluER-T36A, but with red LED irradiation without agitation to reflect the reaction conditions described below. The percent of scatter in the absorption spectrum after 24 h was <1% and >99% of the 0 h absorption spectrum remained after 24 h, signaling very little degradation.

3. FRET Calculations

RPE has 72 surface exposed lysine residues, as described previously.[49] Predictive FRET calculations were performed using Förster theory as described above for the ATTO-GluER-T36A conjugates, except this compound is a single donor, multi acceptor system similar to our previously published biohybrids.[49] Therefore, the calculated conjugate FRET rates and efficiencies were found by summing the rates of 3 individual FRET rates (one contributed by each acceptor) randomly chosen from among the conjugatable lysine residues.[176] The donor-acceptor distance was calculated by summing the distance from an emitting chromophore on RPE to a conjugatable lysine, the length of the SATA crosslinker (2.8 Å), the length of the SIA crosslinker (1.5 Å), and

the distance from a conjugatable lysine to the flavin of GluER-T36A (total average distance ~ 68.3 Å). The spectral overlap integral of the sample was 8.52×10^{13} $\text{nm}^4 \text{ M}^{-1} \text{ cm}^{-1}$ for the oxidized flavin state and 4.27×10^{13} $\text{nm}^4 \text{ M}^{-1} \text{ cm}^{-1}$ for the charge-transfer state and the Forster distance, $R_0 = 30.9$ Å for the oxidized flavin state and $R_0 = 27.5$ Å for the charge-transfer state. The individual FRET rates were ensemble averaged 100x to account for inhomogeneity in the system, leading to an average FRET efficiency of 16.8% and 10.2% and timescales of 9.50×10^{-9} s and 2.93×10^{-8} s for the oxidized flavin and charge-transfer states, respectively.

4. Fluorescence Lifetime Measurements to Confirm Successful Energy Transfer

The fluorescence lifetime of the RPE-GluER-T36A conjugates was compared to the fluorescence lifetime of unreacted RPE to confirm the occurrence of energy transfer (Figure S3.20). The instrumentation was the same as described above for ATTO dye-GluER-T36A conjugates, and the same 550 nm excitation and 580 nm emission filters were used. All samples were fit to a monoexponential function. The fluorescence decay of RPE possessed a lifetime of 2.34 ns, and a simple mixture of 1 eq RPE and 3 eq GluER-T36A possessed a lifetime of 2.63 ns, both in agreement with values found previously.[49,181,226] The fluorescence lifetime of RPE-GluER-T36A was 1.92 ns. This data suggests a FRET efficiency of 18%, on par with the predictive FRET calculations.
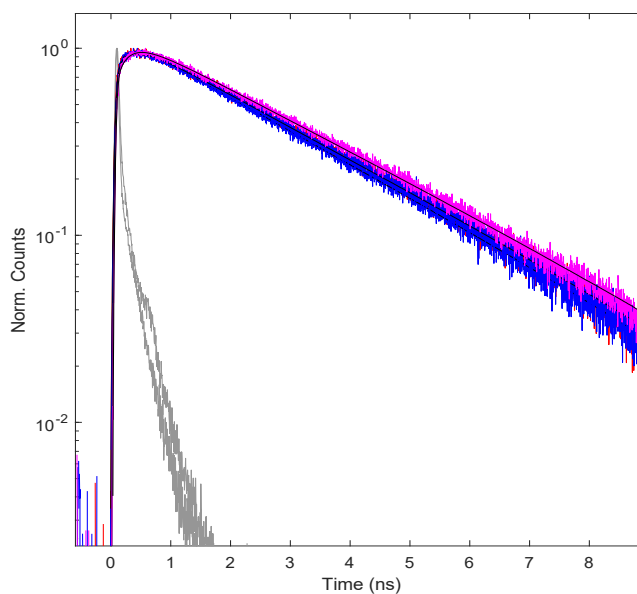
Figure S3.20: Fluorescence lifetime measurements. RPE-GluER-T36A conjugate (blue), RPE (red, obscured), and a simple mixture of RPE and GluER-T36A (magenta), along with the IRF (gray).

5. Test Reactions

The lactam cyclization was run using the same conditions discussed in the previous section as the ATTO dye-GluER-T36A conjugates using 0.15 mol% of the RPE-GluER-T36A conjugate with irradiation via the red LED setting on the 3568 SMD LED light strips and no shaking. Red light irradiation of the RPE-GluER-T36A conjugate enabled red light activity (3.3% yield) compared to trace yields that were found with GluER-T36A alone and an unconjugated mixture of GluER-T36A and RPE.

CHAPTER 4:
ULTRAFAST SPECTROSCOPIC INVESTIGATION OF EMERGING MOLECULAR SPECIES – Cu(I) PHENANTHROLINE BASED PHOTOCATALYSTS AND MODULAR DONOR-ACCEPTOR CAGES

This chapter discusses the preliminary results of two projects which investigate the ultrafast dynamics of molecular species. The first section explores the relaxation of Cu(I) complexes after excitation to their higher lying singlet Franck-Condon excited states and the second explores the charge separation and charge recombination dynamics of donor-Pd(II)-acceptor cages. They are grouped together in this work and within the supporting information for this chapter, but are intended to be published independently as fuller works once further analysis and interpretation occurs.

4.1 ULTRAFAST EXPLORATION OF THE HIGH ENERGY STATES OF Cu(I) BIS(R-PHENANTHROLINE) COMPLEXES

Transition metal photocatalysts with earth-abundant metal centers are being increasingly studied for their photophysics and photochemistry. The base materials for these complexes are more affordable, more environmentally friendly, and less toxic than the most often used ruthenium and iridium centered species.[227,228] However, their photophysical characteristics are lacking. After excitation, Ru(II) and Ir(III) form an initially excited ^{1}MLCT state which then rapidly converts into a ^{3}MLCT state via intersystem crossing.[1,2] The lifetime of second and third row metal complexes are long (μs) and they are easily accessible for both oxidative and reductive chemistry, which has led to these complexes being employed to catalyze a large number of reactions.[1,2] First row metal species have metal-centered excited states lower in energy than their charge-transfer transitions (the Primogenic Effect), which causes rapid relaxation from the charge-transfer manifold to the metal-centered states after excitation.[229] This relaxation results in lower energy final states for reactivity, decreased lifetimes, and a metal-centered reactive molecule shielded by

its ligands. Therefore, many first row metals have been underutilized in photoredox catalysis, though some exploration has occurred.[230]
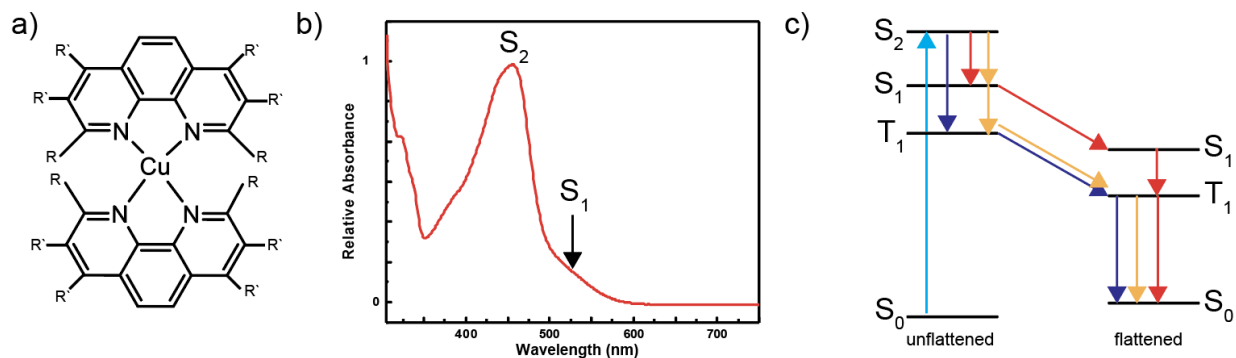
Figure 4.1: Structure, ground state electronics, and proposed relaxation pathways. (a) The general structure of Cu(I)bis(R-phenanthrolines), where R and R' signify potential substitution locations. (b) Absorption spectrum of Cu(I)bis(dimethylphenanthroline) showing the S_2 and S_1 excitations. All of the complexes possess this general structure in different peak ratios. (c) After excitation at 400 nm (light blue), three different relaxation pathways have been proposed, shown in red, dark blue, and yellow.

Cu(I) complexes, by contrast, are first row metal centered, but they do not suffer from the rapid relaxation into metal-centered electronic states because of their filled d^{10} orbital electron configuration, which has led to their rapid exploration and demonstration for photocatalysis.[227,231] Cu(I) bis(R-phenanthroline) species have been studied for their unique photophysical properties because after excitation, the ligands flatten from an initially tetrahedral configuration due to a pseudo-Jahn-Teller distortion before intersystem crossing to a long lived ^{3}MLCT state.[12] The lifetime of the resultant ^{3}MLCT state, and the length of each of the relaxation processes, has been shown to be modulated by the identity of the substituents on the phenanthroline ligand (R and R' in Figure 4.1a), achieving luminescence lifetimes of up to 4.3 μs.[12,232] Increased bulkiness of the ligand substituents is theorized to have a long range inductive electronic effect, leading to the modularity of the lifetimes.[232] The ultrafast excited state dynamics are underexplored, and when initially excited to the higher lying singlet electronic state(s) using 400 nm light (Figure 4.1b),

relaxation has been thought to proceed via multiple different pathways (Figure 4.1c).[12,233,234] Excitation to the higher lying singlet state(s) (S_2) may result in rapid (~100 fs) internal conversion to the lower lying excited singlet (S_1) followed by flattening of the complex (~400 fs) and intersystem crossing to the triplet manifold (T_1) or the lower lying singlet may be followed by intersystem crossing directly to the triplet state manifold (450 fs), and the flattening may then occur within the triplet states.[233] Another posited pathway is direct intersystem crossing from the higher lying singlet excited state to the triplet manifold where flattening and further relaxation occur.[12] It is also uncertain whether or not the higher lying singlet state relaxation is subject to the same ligand-dependent lengthening of relaxation as the lower lying states are (47 fs in Cu *bis*-dimethylphenanthroline vs. 135 fs in Cu *bis*-diphenylphenanthroline).[12] Herein, initial ultrafast transient absorption (TA) spectroscopy experiments to shed light on these processes are reported.

Ten Cu(I)bis(phenanthroline) complexes were studied, each with a differently substituted phenanthroline ligand (chemical structures are shown in Figure S4.1). Figure 4.1b shows the absorption spectrum of Cu(I)bis(dimethylphenanthroline), which is a benchmark compound and provides a benchmark absorption spectrum for all of the other complexes. While the relative absorbance between them may vary, all of the complexes possess a strongly absorbing band to the higher lying singlet charge-transfer manifold centered around 450 nm and a weaker absorbing band to the lower lying singlet charge transfer manifold centered around 525 nm.[12] Prior literature has examined the emission of the higher lying singlet S_2 state using ultrafast fluorescence measurements.[12] This emission is Stokes shifted from main absorption and centered around 510 nm. Prior TA spectroscopy on these complexes has shown a ground state bleach (GSB) feature centered around 450 nm and a rapidly and constantly evolving excited state absorption (ESA) feature which allows the tracking of the relevant dynamics at hand.[12,232]
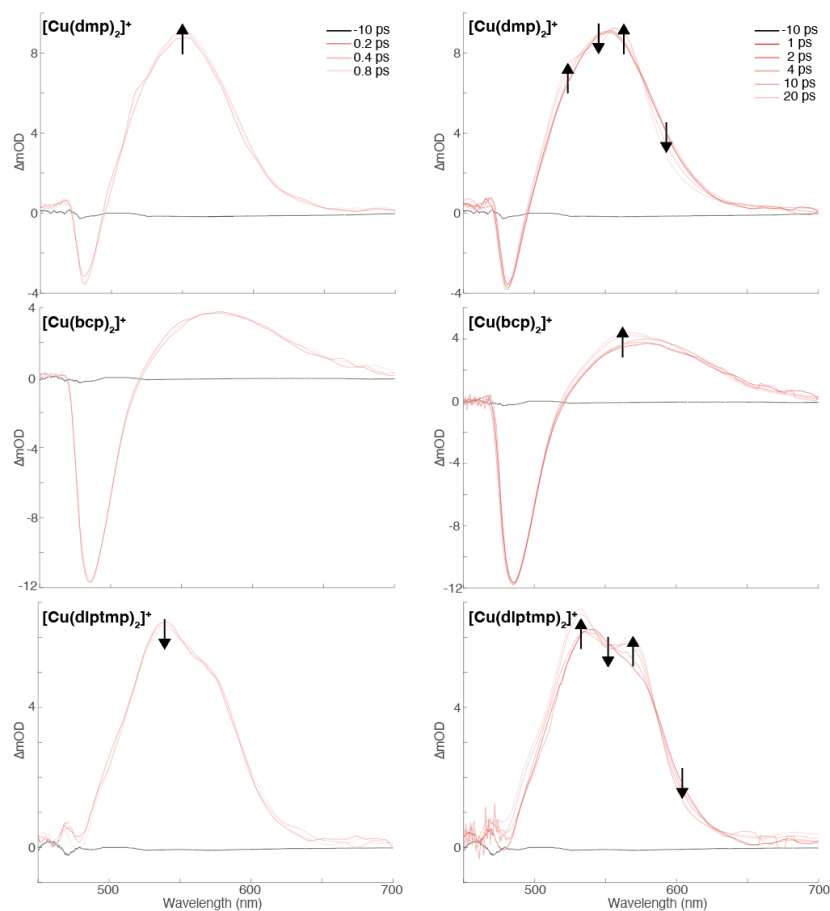
Figure 4.2: TA spectra of three select complexes. Left, the TA spectra from 200 to 800 fs showing initial evolution, and right, the TA spectra from 1 to 20 ps showing further changes. Directionality is given by selected arrows.

We performed ultrafast transient absorption spectroscopy (setup described in SI Section 4.1) on all ten of the complexes to mainly examine the short time dynamics and initial state transitions. The acquired spectra for three select complexes are shown in Figure 4.2 and arrows are added to show the time evolution. The complexes shown, $[Cu(dmp)_2]^+$ (dmp = 2,9-dimethyl-1,10-phenanthroline), $[Cu(bcp)_2]^+$ (bcp = bathocuproine), and $[Cu(diptmp)_2]^+$ (diptmp = 2,9-diisopropyl-3,4,7,8-tetramethyl-1,10-phenanthroline) all exhibit the large ESA feature expected, with the dmp and bcp complexes also showing the long lived GSB. Qualitatively, all of the spectra exhibit strongly changing dynamics on the >1 ps timescale which match prior literature.[12] Briefly,

for the $[Cu(dmp)_2]^+$ complex, the rise centered at 550 nm from 200-800 fs corresponds to the flattening distortion with a timescale of 200 fs, and the spectral dynamics occurring 1 ps to 20 ps correspond to the intersystem crossing of the flattened complex to its triplet state with a timescale of 1.8 ps. Therefore, the qualitative agreement in spectral evolution allowed for a more thorough investigation of the short time dynamics which provide insight into the higher lying S_2 states.

In order to examine these states, kinetic traces for each of the three complexes were extracted from the data at 510 nm, which is presumably where the stimulated emission (SE) of the S_2 is, based on prior literature results from ultrafast fluorescence experiments.[12] The traces were cropped to isolate their rise time features, as the predicted dynamics will be <200 fs, and then fit using a convolution of the 78 fs IRF and a biexponential decay after subtracting the nonresonant response of the tetrahydrofuran solvent (Figure 4.3). The first component of the biexponential fit corresponds to the lifetime of the S_2 state, fit with a negative amplitude as it traces the stimulated emission and the second would theoretically correspond to the flattening distortion from the S_1 state after the internal conversion, fit with a positive amplitude corresponding to the ESA. We note theoretically because cropping the kinetic traces to isolate the rise time features limits the utility of the data for this feature. The timescales obtained for the second component were 7.4 ps for $[Cu(dmp)_2]^+$, 20 ps for $[Cu(bcp)_2]^+$, and 200 ps for $[Cu(diptmp)_2]^+$, which increase as expected with bulkier ligand identity. They each had a relative amplitude of the total fitting function of 24%, 19%, and 42% , signaling that the short time component is more significant to the overall rise. The first component had fitted lifetimes of 55 fs (76% relative amplitude) for $[Cu(dmp)_2]^+$, 35 fs (81% relative amplitude) for $[Cu(bcp)_2]^+$, and 180 fs (58% relative amplitude) for $[Cu(diptmp)_2]^+$, which roughly increase with bulkier ligand identity. Although the nonresonant response of the THF was

subtracted from the data, there are still residual spikes present in the traces, especially evident for $[Cu(bcp)_2]^+$, complicating the data analysis and adding a potential source of error.
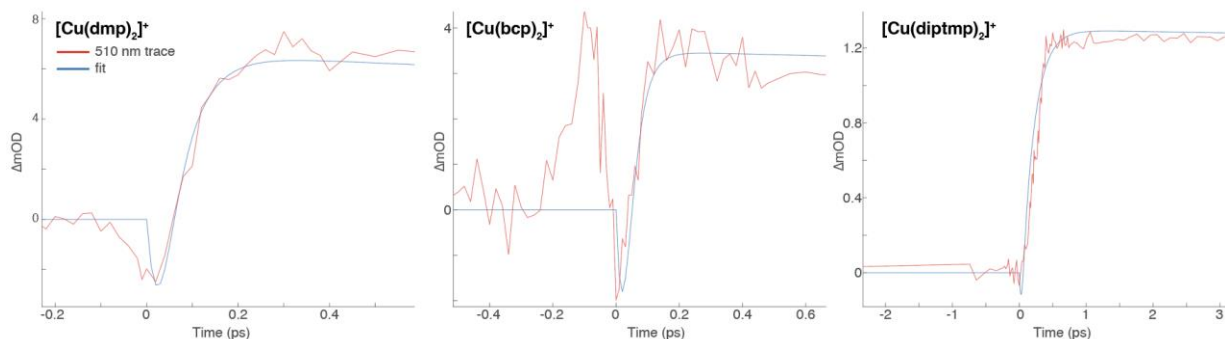
Figure 4.3: Kinetic traces and fits for three complexes.

This data and very initial analysis seem to indicate that the lifetime of the S2 state is in fact subjected to the same inductive effects which cause the systematic change in the other lifetimes of the complexes. Because the S_2 state is MLCT in nature, it would presumably be affected by changes in the electronic structure of the ligand, so this result is not completely surprising. Further analysis is required to determine whether or not the rest of the complexes follow a similar trend in their fitted lifetimes. Another hindrance to proper assignment of the features is the overlapping ESA, SE, and in the case of $[Cu(bcp)_2]^+$, an overlapping GSB feature. Further detailed global analysis will shed light on the underlying features that can be found within the TA datasets, and potential future experiments, such as two-dimensional electronic spectroscopy (2DES), may allow for the explicit observation of changes in the electronic structure during these very short timescales.[235–237] Overall, much work remains to be completed, but the initial results of this work are promising.

4.2 INVESTIGATION OF THE ULTRAFAST DYNAMICS OF DONOR-Pd(II)-ACCEPTOR CAGES VIA SYSTEMATIC LIGAND SUBSTITUTION

Supramolecular chemistry has received much attention in recent years for the unique properties self-assembly and host guest chemistry can achieve, such as binding molecules for biomedical applications, creating unique molecular motors, and acting as catalytic species.[43,82,238,239] Complexes like rotaxanes self-assemble multiple molecules to create larger structures similar to beads on a necklace and are able to perform the previously listed feats.[240] Supramolecular structures have been developed to perform large scale energy and charge transfer.[241–245]

The Clever lab has developed a synthetic strategy for greater structural control over donor-acceptor supramolecular complexes via spatially restricting the cage formation.[246] Like a puzzle, certain combinations of donors and acceptors will only fit together in certain ways. Changing the properties of the substituents in both the donor and acceptor can then drive different structures of cages to be formed.[246–248] To-be-published results have spectroscopically explored a single donor-Pd(II)-acceptor cage and its charge separation and recombination upon light absorption. Herein, we report the different kinetics of six combinations of donor-Pd(II)-acceptor cages (D-Pd(II)-A) (Figure 4.4) through a systematic study using transient absorption (TA) spectroscopy. Preliminary results find that the major timescale observable, corresponding to charge recombination, depends on the thermodynamic driving force of charge recombination between the component molecules, and all of the complexes possess similar relaxation dynamics across the scope of components.
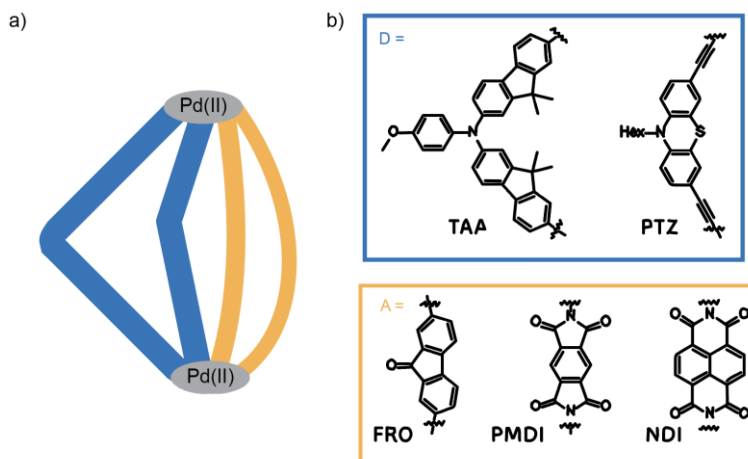
Figure 4.4: Structure of the resulting D-Pd(II)-A cage and its substituents. (a) Cartoon structure of the cages and (b) molecular structures of the donors and acceptors.

Synthesis. The D-Pd(II)-A cages were a 1:1:1 combination of a donor molecule chosen among modified phenothiazine (PTZ) or triarylamine (TAA), a Pd(II) metal ion linking on top and bottom, and an acceptor molecule chosen among modified pyromellitic diimide (PMDI), naphthalene diimide (NDI), or fluorenone (FRO) (Figure 4.4b). Modified ligands were synthesized by the Clever lab. D-Pd(II)-A synthesis is afforded by mixing of the starting materials which self-assemble in the presence of the palladium salt, and can be confirmed by observing the loss of emission of the donor under a UV lamp.

Steady-state absorption spectra. The steady-state absorption spectra of each donor and acceptor in the visible region are shown in Figure S4.2. Overall, TAA has a broad absorption band from 325-475 nm and a peak at 280 nm and PTZ has two broad absorption bands which overlap at 290 nm and 380 nm for the donor species. These broad absorption bands are quite representative of conjugated organic molecules. For the acceptor species, FRO has a strong pi-pi* absorption at 275 nm with a featured shoulder at 320 nm and a small band at 425 nm, NDI has two sharp features at 350 and 375 nm, and PMDI has nearly no visible absorption. When charge separation occurs between the donor and acceptor substituents within the cages, a donor radical cation and acceptor

radical anion are formed, and the relevant absorption bands of these excited state species can be examined through electrochemical oxidation/reduction.

Spectroelectrochemistry. Via reduction or oxidation of the donor and acceptor molecules, we can gain some insight into the excited state properties of the individual molecules by obtaining their spectra (Clever lab). By subtracting the ground state absorption spectrum from the one obtained after electrochemical oxidation/reduction, the initial TA spectrum is roughly obtained. In the individual spectra, all donors and acceptors possess notable features in the visible region of the absorption spectrum. TAA mainly absorbs below 450 nm in the neutral ground state, and this is reflected by a predicted ground state bleach feature at 388 nm in the TA spectrum. The oxidized TAA absorbs more strongly in the visible region, leading to predicted positive ΔA features with peaks at 460, 568, and 800 nm. The PTZ donor similarly exhibits a predicted ground state bleach feature at 389 nm, and two pronounced predicted excited state absorption features at 513 and 679 nm resultant from oxidation. As for the acceptor species, PMDI exhibits predicted excited state absorption peaks across the visible range at 416 and 715 nm, NDI has both a strong predicted ESA at 474 nm with a weaker ESA at 605 nm and a predicted GSB at 389 nm, and FRO has only one predicted ESA features at 571 nm. The spectroelectrochemical results along with their predicted transient features are shown in Figures S4.3 and S4.3. The results of these measurements suggest that in the experimental TA data in our absorption region (485-565 nm), we will mainly observe a broad excited state absorption containing all of the features of both the donor and acceptor components within a single cage.

Transient absorption spectra. TA data was obtained for all compounds in the spectral region of 485-565 nm to the time delay of 800 ps. Based on prior results obtained for these cages (Clever lab, unpublished), we fitted the data to a three-component parallel model in global analysis

consisting of a ~1 ps component, a ~30 ps component, and a ~1 ns (or linear offset) component, described more fully in SI Section 4.3.2 and visualized in Figure 4.5a. As charge separation to donor and acceptor species occurs within the timescale of the IRF (~273 fs), the parallel relaxation of the species back to the ground state is the most observable dynamic. Due to instrumental limitations in our delay stage resolution, we are unable to place concrete values or interpretation to the long-time ~1 ns component, which was previously assigned as the relaxation of the *trans*-Pd(II)D$^+$A$^-$, but the values obtained are provided in SI Table S4.1. More concretely, we were able to obtain information regarding the kinetics for all samples of the ~1 ps time, identified previously as the relaxation of the Pd(I) D$^+$A, and the ~30 ps time, identified previously as the relaxation of the *cis*-Pd(II)D$^+$A$^-$. Representative examples of the TA spectra for each of the two donors with the NDI acceptor are shown in Figure 4.5b, and all spectra and single wavelength kinetic fitting is shown in SI Figures S4.5, S4.6, and S4.7. All fitted rate values are provided in SI Table S4.1.
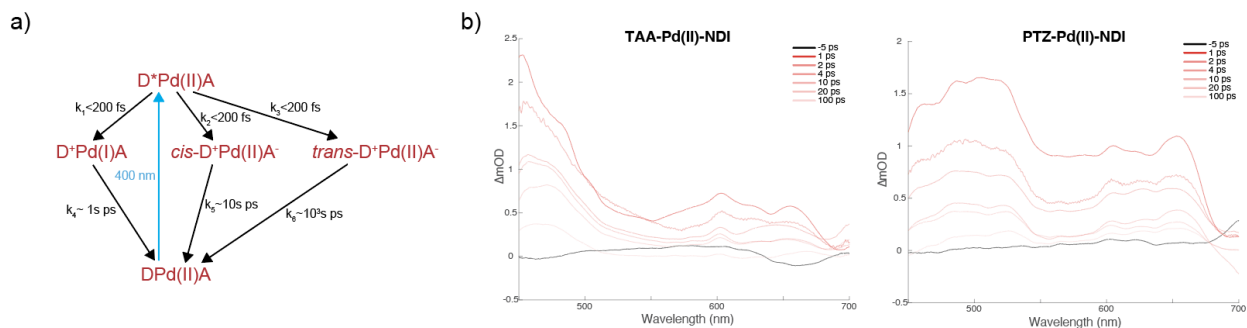
Figure 4.5: Jablonski diagram and TA spectra of D-Pd(II)-A cages. (a) State diagram of the donor acceptor cages after excitation with 400 nm light, showing possible charge separation and recombination timescales. (b) Representative TA spectra for D-Pd(II)-NDI cages.

Qualitatively, the TA spectra all exhibit a broad excited state absorption (ESA) across the probe pulse wavelength range as predicted in the spectroelectrochemical results for all six samples. For the cages which contain PTZ as donor, all exhibit the calculated species associated spectra (SAS, Figure S4.4) which have broad dual peaks of roughly equivalent magnitude at 500 and 600

nm for the initial ~1 ps component. This component represents much of the relative amplitude of each of the components for each sample, as much as 79%. This value is similar to prior results and is resultant from relaxation from the initially charge separated species via the Pd(II) linker itself. As the Pd(II) linkers are positively charged by their nature, they represent a natural sink for negative charge to congregate, and much of the amplitude of the initial transient absorption spectra confirm this thought. Also, this initial component SAS heavily resembles the donor only spectroelectrochemical results, which would be expected in the case where the acceptor is not completely involved in relaxation after photoexcitation. For the other two components, the mid-time ~30 ps component and the long-time nanosecond component, more mixed results are obtained. They both show broad features across the spectral range, representing a mixture of the predicted donor and acceptor features. For example, the 600 nm transient peak of NDI are present in all samples containing this acceptor. For the cages containing the TAA donor, much of the same SAS features and reasons are expected and confirmed. The initial component SAS nearly exactly mirrors the difference spectroelectrochemical spectrum of the TAA donor, having a very strong peak at 450 nm. Then, the second two components have spectral features mixed between donor and acceptor as they represent the decay of both species to the ground state.

Most interesting regarding the results of the TA spectral fitting are how the second component, representing charge recombination between the donor and *cis*-acceptor species in the cage, tracks roughly with the thermodynamic driving force of the recombination. This correlation is shown in Figure 4.6. The thermodynamic driving values for charge separation and recombination, dG, were calculated using the Rehm-Weller equation and values obtained from C-V measurements of each of the donors and acceptors (Clever lab). This correlation between rate and thermodynamics will be further explored by applying Marcus theory to the data after

prediction via collaboration with theorists. Further insight into the exact identity of the spectral makeup and analysis of the data is necessary in order to more concretely identify the dynamics at play between the states. Higher time resolution data will also provide further detail into the charge separation step. Overall, the systematic variance of ligand identity in the D-Pd(II)-A cages shows that, in combination with a non-stochastic assembly method, control over the dynamics of charge separation and the prediction of these properties are achievable. This work lays the foundation for further exploration into other supramolecular charge separated species and the application of larger scale charge separation to higher order structures.
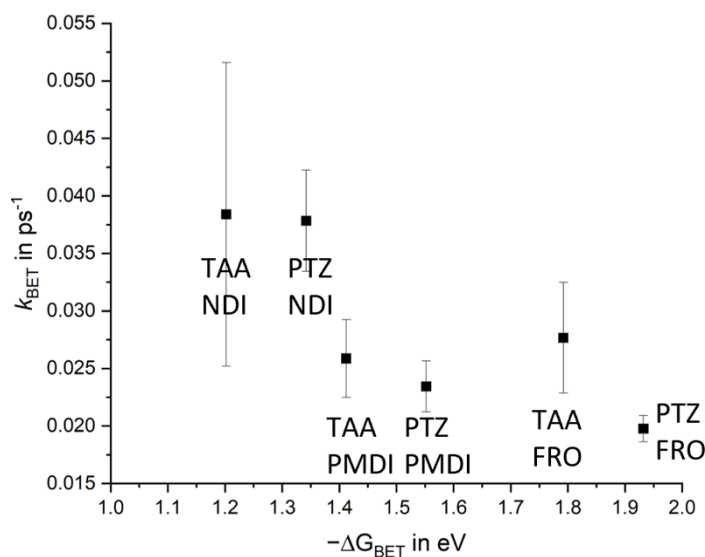
Figure 4.6: Correlation of back electron transfer rate with thermodynamic driving force in D-Pd(II)-A cages.

4.3 SUPPLEMENTARY INFORMATION
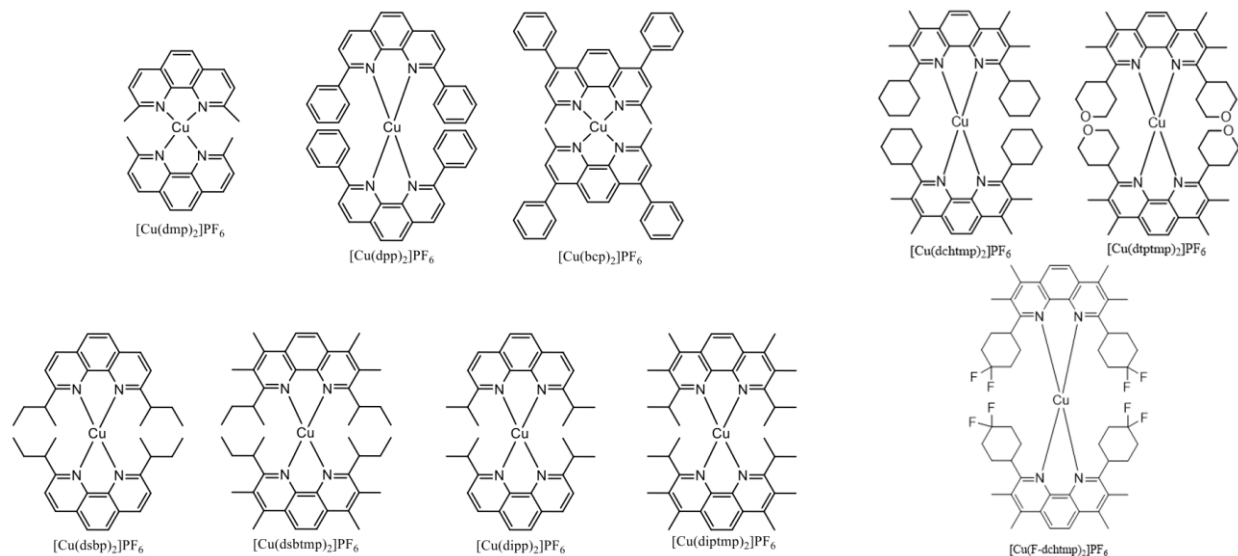
Figure S4.1: Structures of the Cu(I)bis(R-phenanthroline) complexes studied herein.

4.3.1 TA Spectroscopy experimental details for Cu(I) complexes.

The transient absorption (TA) spectroscopy setup consists of a regeneratively amplified Ti:Sapphire laser (Libra, Coherent, Santa Clara, CA) producing ~50 fs laser pulses centered around 800 nm at 5 kHz repetition rate. The pump arm consisted of a time-delayed second harmonically generated pulse filtered to 400 +/- 10 nm excitation operating at a power of 2.4 mW (960 nJ/pulse) via focusing the fundamental beam into a BBO crystal. The pump alternated shots at 2.5 kHz using an optically-gated chopper. The probe arm consisted of focusing the fundamental into an Ar-filled tube to generate a white light continuum, which was compressed via prisms and filtered to a range of 475-700 nm (Thorlabs FGS600 colored glass filter). The probe arm was detected after non-collinear focusing with a home-built Czerny-Turner spectrograph and was detected with a CCD array (Aviiva EM2, Teledyne e2v) on a shot-to-shot basis. Each two consecutive laser shots were used to calculate the TA spectrum at each time delay using DA = log($I_{pump\ off}$/$I_{pump\ on}$). For each scan, 2500 TA spectra were collected at each time delay across the TA trace and further traces were

133

repeated and averaged until good signal-to-noise was obtained. The overall instrument time resolution was determined to be 78 fs obtained via frequency resolved optical gating (SFG-FROG). Analysis was performed using Matlab by extracting the kinetic traces at desired wavelengths and fitting with a biexponential decay convoluted with a Gaussian IRF.
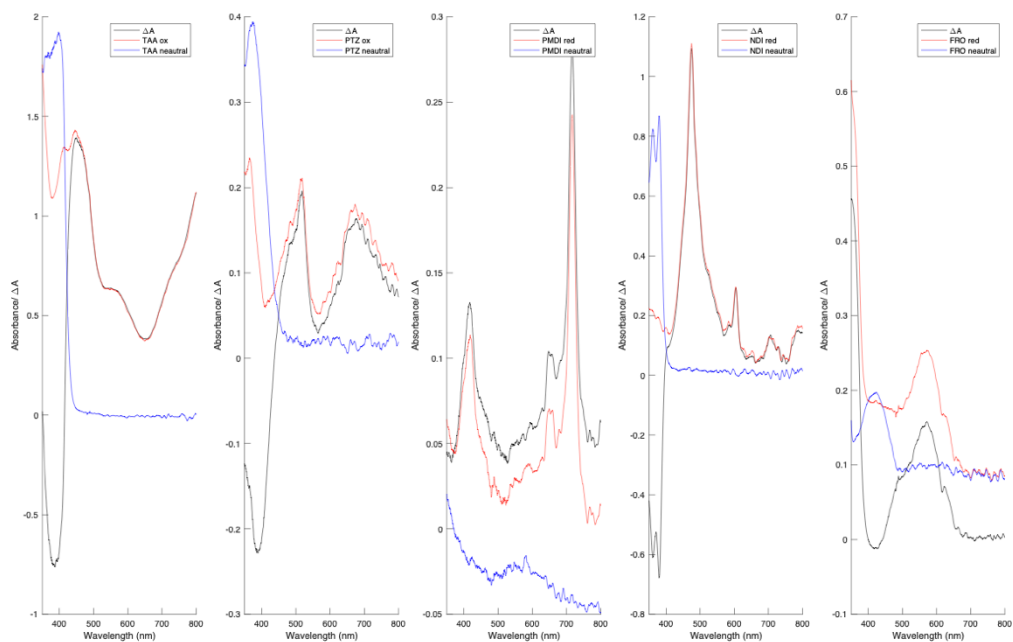
Figure S4.2: Ground state spectra and spectroelectrochemistry of the donor and acceptor species in D-Pd(II)-A cages. By subtracting the neutral spectrum from the ionic spectrum, one can obtain a rough prediction of the TA spectrum for the components.
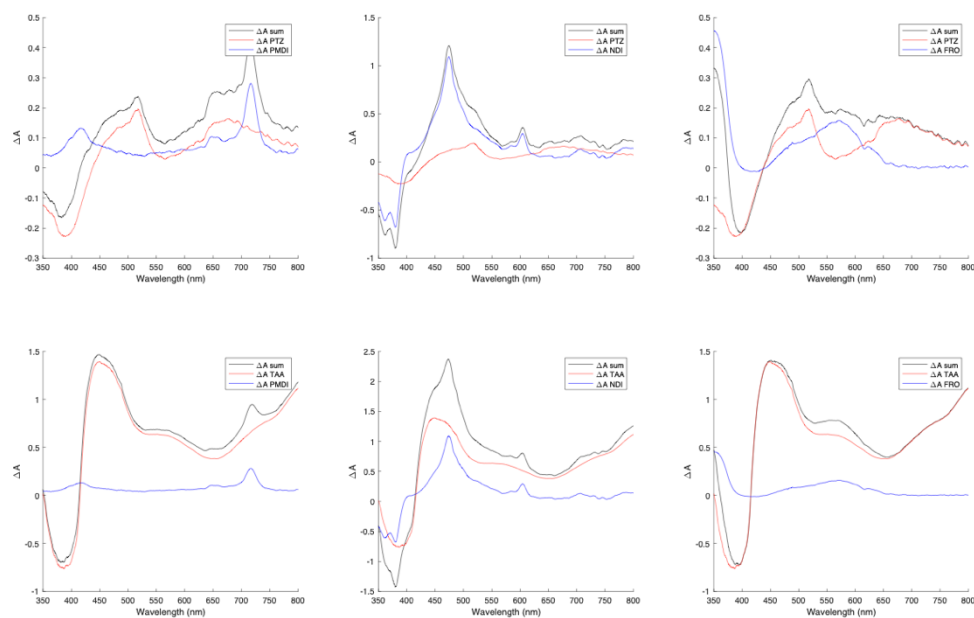
Figure S4.3: Sum of the charged donor and acceptor species difference spectra. This summation allows for a rough prediction of the cage TA spectrum.

4.3.2 TA Spectroscopy experimental details for D-Pd(II)-A Cages. All cage samples were filtered through a 200 nm filter to remove any aggregates and prepared to an OD = ~0.3 at 1 mm path length in acetonitrile.

The transient absorption (TA) spectroscopy setup consists of a regeneratively amplified Ti:Sapphire laser (Libra, Coherent, Santa Clara, CA) producing ~50 fs laser pulses centered around 800 nm at 5 kHz repetition rate. The pump arm consisted of a time-delayed second harmonically generated pulse filtered to 400 +/- 10 nm excitation operating at a power of 1 mW (400 nJ/pulse) via focusing the fundamental beam into a BBO crystal. The pump alternated shots at 2.5 kHz using an optically-gated chopper. The probe arm consisted of focusing the fundamental into an Ar-filled tube to generate a white light continuum, which was compressed via prisms and filtered to a range of 475-700 nm (Thorlabs FGS600 colored glass filter). The probe arm was detected after non-

collinear focusing with a home-built Czerny-Turner spectrograph and was detected with a CCD array (Aviiva EM2, Teledyne e2v) on a shot-to-shot basis. Each two consecutive laser shots were used to calculate the TA spectrum at each time delay using $DA = log(I_{pump\ off}/I_{pump\ on})$. For each scan, 2500 TA spectra were collected at each time delay across the TA trace and further traces were repeated and averaged until good signal-to-noise was obtained. The overall instrument time resolution was determined to be 273 fs obtained via frequency resolved optical gating (SFG-FROG).

Global analysis for the TA data was performed using the Glotaran software[180] after single wavelength and spectrally integrated fitting was performed using Matlab. Based on prior unpublished results from the Clever lab, charge separation from the donor species (PTZ or TAA) to the acceptor species (PMDI, NDI, or FRO) has occurred within the instrument response time. Therefore, relaxation is the only process left to occur, and in combination with knowledge from the prior results, all samples were fit to a parallel three component exponential decay model. The results of this model for each sample are summarized in Table S4.1, and the species associated spectra (SAS) for each sample are shown in Figure S4.4. The rate decay constants broadly match the prior results - a ~1 ps, ~30 ps, and a long-lived nanosecond component. Data were fit first in Matlab using a biexponential decay with a constant offset term, which captured the long-time component as our delay stage only moves to 800 ps, and a term fixed to the IRF time of 273 fs. Then, the data for the first two components was input into Glotaran, where a value for the long-time component could be found by free fitting. This value was then held constant, and the other two were allowed to float in order to more finely obtain useful fitted values. In some cases, the short time component would collapse for best fit in global analysis, and so, we needed to restrict

the free fit to the value obtained by integrating the single wavelength fitting found via Matlab, which provides a rough estimate of the global kinetics. The SAS and TA spectra agree with the difference spectra shown in Figure S4.3 within reason and within the wavelength range of the probe light.

Table S4.1: Fitted time constants from global analysis.

Sample	t_1 (ps)	t_2 (ps)	t_3 (ps)
PTZ-PMDI	1.52	39.8	2.70×10^3
	1.47	45.5	2.88×10^3
PTZ-NDI	1.32	24.3	2.73×10^3
	1.23	28.6	2.73×10^3
PTZ-FRO	2.02	52.6	1.49×10^3
	1.09	48.5	1.49×10^3
TAA-PMDI	0.926*	42.2	0.906×10^3
	0.926*	35.1	0.906×10^3
TAA-NDI	1.40*	32.4	0.264×10^3
	1.40*	20.0	0.264×10^3
TAA-FRO	0.450	40.5	0.463×10^3
	1.51*	31.8	0.463×10^3

*denotes component fixed to spectrally integrated values obtained in Matlab
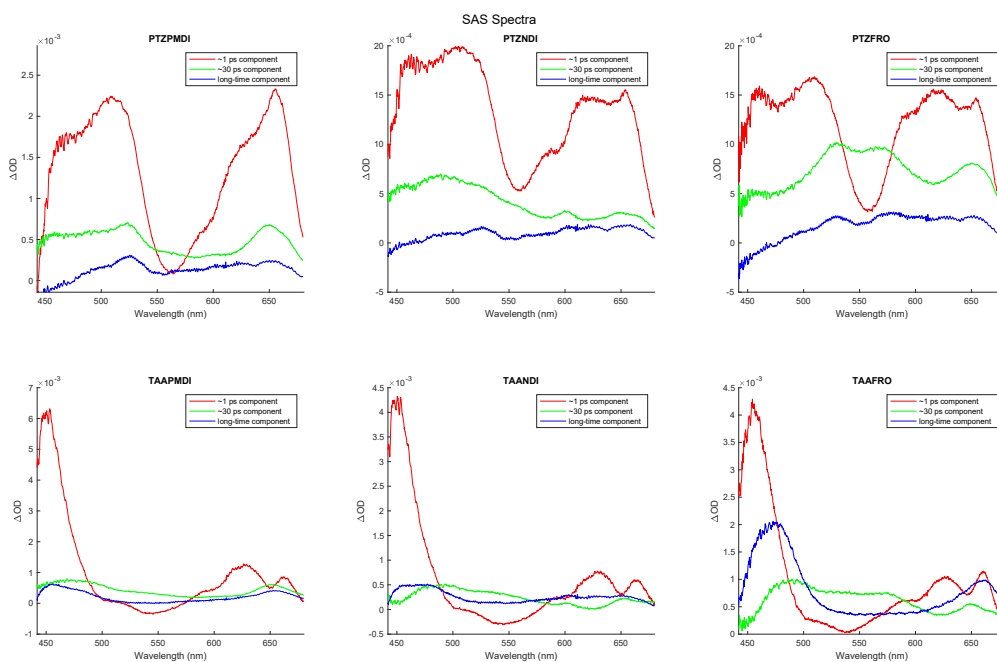
Figure S4.4: Species Associated Spectra (SAS) of D-Pd(II)-A cages. The SAS spectra for each of the three components obtained from global analysis.
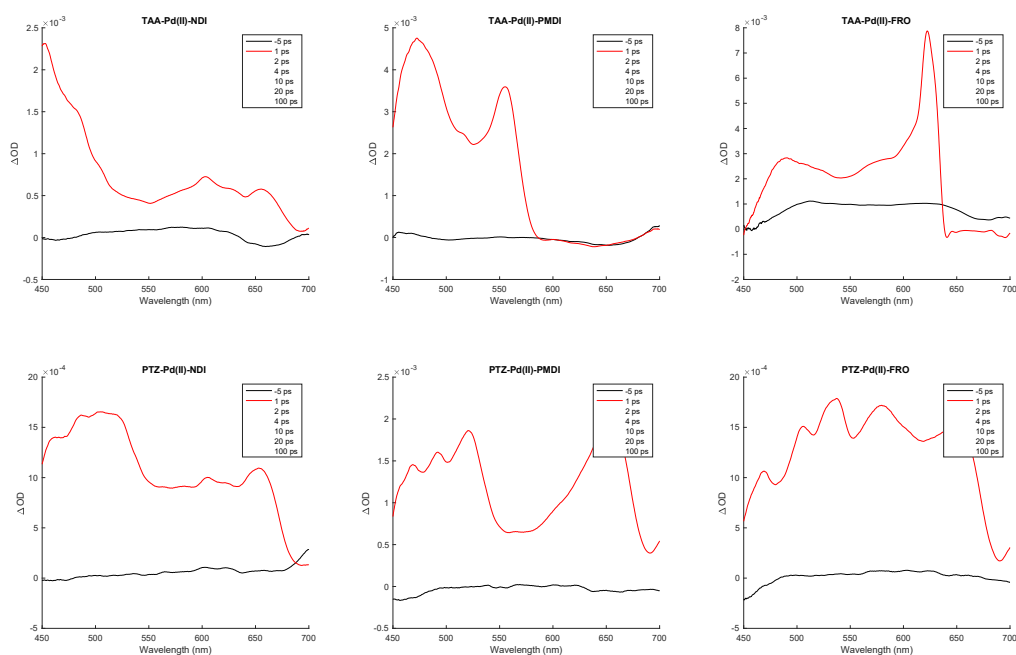
Figure S4.5: Representative TA spectra for all D-Pd(II)-A cages.
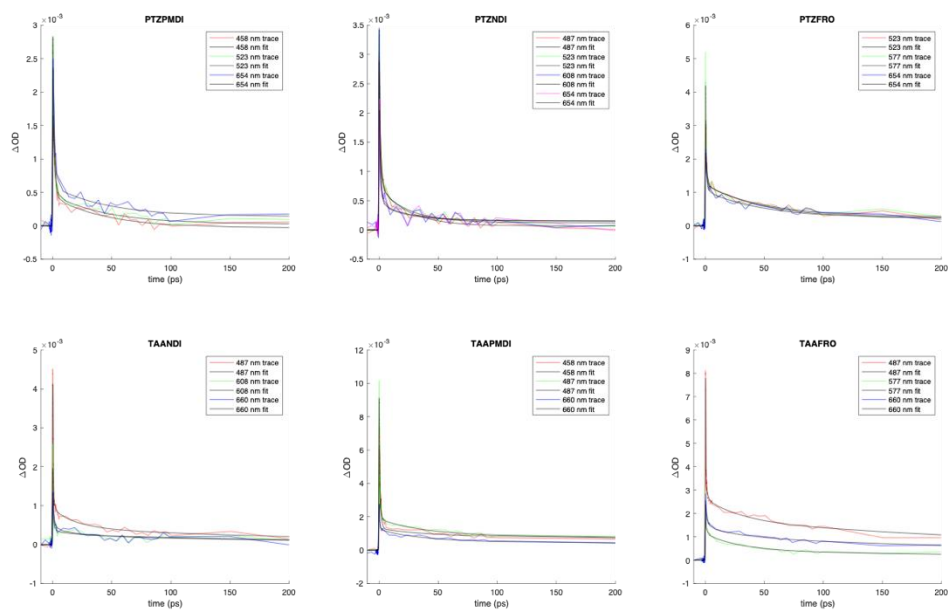
Figure S4.6: Fitted single wavelength kinetics, zoomed. Fitted single wavelength kinetic traces at important wavelengths, zoomed to show up to 200 ps.
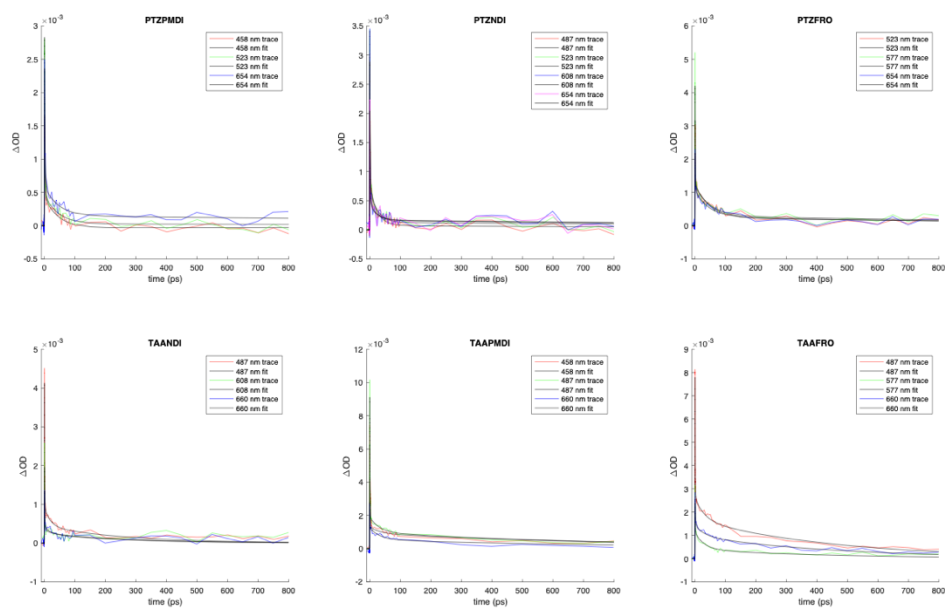
Figure S4.7: Fitted single wavelength kinetics. Fitted single wavelength kinetic traces at important wavelengths, up to 800 ps.

CHAPTER 5:
FUTURE DIRECTIONS AND CONCLUSION

5.1 NEW DEVELOPMENTS AND POTENTIAL FUTURE CHALLENGES OF BIOINSPIRED PHOTOCATALYSTS

The potential future of bioinspired light harvesting catalysis:

a) Exploration of uphill energy transfer

b) Earth abundant reactive species

c) Harnessing multiple photons and electrons
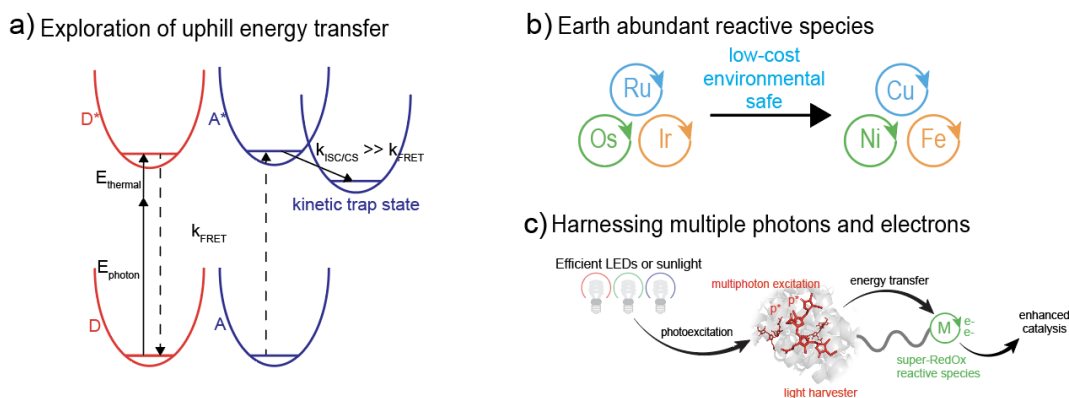
Figure 5.1: Potential future goals to improve bioinspired catalysts. (a) Further utilization of uphill energy transfer steps similar to photosynthetic organisms. (b) Replacement of heavy metal compounds with reactive first row analogues. (c) Improvements in the ability to harness, transfer, and utilize multiple photon absorptions for extremely high energy reactivity on a single species.

Pushes to optimize light utilization for catalysis have made great strides, even over the last half decade, but there are further advancements to be attained. Figure 5.1 graphically depicts some of the potential for future bioinspired catalysts. The requirements for uphill energy transfer are more stringent than downhill FRET (Figure 5.1a), but its potential utility is enormous. Note that uphill FRET does not break any fundamental laws of thermodynamics - the kinetic product of the transfer is simply targeted. Energetically, thermal (or other) types of energy can fill the gap required to move uphill, as was calculated for a 600 nm photon to excite $[Ru(bpy)_3]^{2+}$ in our initial report.[49] The goal is to exploit the kinetic product before it returns to ground state or transfers back. After energy transfer from light harvester to reactive moiety, a trapping state needs to be rapidly

populated. An intersystem crossing or charge separation is best for this need, and both of these steps are already present in most used catalysts, as their longer natural lifetimes are better for collision-based reactivity. A triplet state or physical charge separation means that reverse (downhill) energy transfer via FRET is impeded. To exploit this process, further thought of catalyst and conjugate design is needed, but possibilities for unique reactivity remain numerous. As many reactions are run at higher than room temperature, energetic contributions from thermal energy can be advantageously used to push reactivity higher in energy with lower energy light. With a highly optimized absorber, light capture across the visible range could be achieved, and as demonstrated, even minimal spectral overlap can lead to high efficiencies of energy transfer, especially if multiple acceptors are employed. Uphill energy transfer achieved via conjugated bioinspired systems easily results in the goal of having high-energy reactivity with broadly absorbing low-energy light, and these aspects should be considered in catalyst design. The scope of potential reactions that could benefit with this approach is enormous, especially when applied to biological tissue, where high energy reactivity for specific bond formation (i.e. for wound healing or cell mapping) is necessary along with low energy light which can penetrate biological media.[77,249–253]

An added benefit to division and specialization of function for catalysis is the ability to tailor the reactive species for a specific type of reactivity or application, without worry to its light harvesting properties. In essence, one could start with a desired application, whether this is a challenging reaction methodology or a highly stereoselective reaction, and design a catalyst which achieves this goal first. No matter how poorly or where in the spectral region the developed catalyst absorbs, the catalyst could be conjugated and sensitized with an optimized light harvester chosen from a library of potential candidates, working backwards to achieve full optimization of the process. This approach is similar to dual catalyst systems whereby combination of a photocatalyst

and a chiral complex result in high energy stereoselective reactivity, examples of which have been demonstrated by the Yoon lab.[254,255] The components were not conjugated and triplet energy transfer was proposed as the operative mechanism. We believe this work can be similarly built upon using the bioinspired approach to achieve enhanced efficiencies in reactivity.

With the development and popularization of directed evolution, the possibilities for enzymatic design are nearly limitless and methods to improve their photoefficiency are desired.[256–258] We previously mentioned how Hyster and coworkers develop photoenzymes which perform non-native reactions on a wider substrate scope. More recently, they expressed 'ene'-reductase enzyme mutants from *Gluconobacter* which absorb red light at an absorption shoulder of 550-800 nm and perform a lactam cyclization reaction, with the highest yield obtained being 99% with 98:2 *er* for the GluER-G6+K283G mutant. The mechanism was proposed to take place via a $\pi - \pi^*$ transition from the active site flavin to the enzyme bound substrate.[259] For future directions, one can envision evolving a photoenzyme with a very strongly absorbing pigment within the enzyme structure itself near the active site as a compliment to the flavin, acting as a fully engineered pigment protein reactive complex. Then, energy transfer to the active site bound substrate would be optimal, as the donor acceptor distance would be even smaller than the two component conjugates discussed previously. These systems could perform non-native reactivity with supercharged light absorption capabilities, and depending on the targeted reaction modality, could perform high energy reactivity with broad and strong absorbing properties in a single, defined system containing both optimized light harvesting and reactive portions of the process.

For photocatalysts based on transition metal complexes, there is a strong urge to move "upwards" in the periodic table away from third row metals to first and second row metal centered systems (Figure 5.1b). Ru, Os, and Ir complexes have all been demonstrated, but they are less

abundant in earth's crust (with Ir being the least abundant crust metal of all) and more expensive.[228] The raw materials within Fe, Cu, Cr, Ni, Zn, etc. centered complexes are cheaper and more abundant, not to mention more environmentally friendly, and so utilizing these metals for catalysis is important. However, their photophysical properties are lackluster: they possess small absorption cross sections, their lowest energy states after relaxation are often very low energy for reactivity and short lived compared to their heavy metal counterparts.[229] There are many ongoing studies concerning the use of these metal complexes in examination of their photophysics and reactivity,[260–267] capabilities as upconverting sensitizers,[23,89–91,268–270] and exploration of the unique ability to exploit their ligand to metal charge transfer states for reactivity.[271] An attached optimized absorber could potentially strengthen the number of excited state earth abundant species in solution. While one can supercharge absorbing capabilities, the catalyst is still limited by low energy metal centered reactive states after relaxation, meaning one drawback to these types of metal complexes is solved, but assistance in improving reactivity is necessary, such as ligand modification to try and make higher energy in nature. The upsides to this approach are immense, however, as a fully earth abundant system could be developed with extremely high efficiency light harvesting and transfer capabilities as well as reactivity.

Then, approaches to harnessing multiple photons for excitation and then utilizing this to transfer multiple electrons for reactivity can continue to be examined inspired by the Z-scheme of photosynthesis (Figure 5.1c). The Wenger lab has already demonstrated a Z-scheme-like catalytic system excited with a 623 nm LED where a Cu(dap)$_2$ catalyst is photoexcited, transfers its excitation to a dicyanoanthracene (DCA) molecule, which is then excited again, and performs multiple types of reactivity (hydrodehalogenation, detosylation, and C-C formation).[272] The Z-scheme structure has also been demonstrated using 456 nm light to excite a perylene diimide

variant termed PTDI, which performed atom transfer radical polymerization.[273] Ilic et al. proposed a two-step consecutive excitation mechanism for an initially Fe(III) ground state complex that performed atom transfer radical addition with similar reaction efficiencies as heavy metal counterparts, demonstrating the viability of both earth abundant metals and multi-excitation in catalysis.[274] The biohybrid approach via energy transfer could make multiexcitation chemistry more controllable on a single species for super-RedOx reactivity. Multi-electron processes require funneling multiple excitations away/toward one reactive moiety, and multiple sequential excitations are only afforded if the absorbing power of the light harvester is immense or if the light source for excitation is extremely powerful. Strongly absorbing species such as photosynthetic light harvesting proteins with molar absorption coefficients on the order of millions can theoretically be multiply excited, effectively funnel this energy to a targeted attached reactive species, and develop strongly reducing or oxidizing states. The available reaction scope of photochemistry is then nearly limitless in terms of energetic requirements, and one can dream of photocatalytically generating energy relevant hydrocarbons from simple starting materials, for example.

5.2 OUTLOOK AND CONCLUSION

Photoredox catalysis is a relatively new field of chemistry, and as such, excitement is high and development occurs rapidly. All of the approaches to supercharging light absorption and reactivity discussed herein are extremely valuable, and all of them lead to unique reaction methodologies being developed and pursued. The separation and optimization of individual light harvesting and reactive species allows for neither portion of the process to suffer from inefficiency. By separating these processes, as Nature does, strong broad-spectrum absorption can be achieved

while also performing high energy, optimized reactivity. No matter the chosen approach, photocatalysis will continue to be researched and implemented in industrial reactivity over the next decades. Possibly, a green future lies ahead with chemical synthesis running on solar powered catalysts, producing little to no carbon or energetic waste.

REFERENCES

(1)   Shaw, M. H.; Twilton, J.; MacMillan, D. W. C. Photoredox Catalysis in Organic Chemistry. *Journal of Organic Chemistry* **2016**, *81* (16), 6898–6926. https://doi.org/10.1021/acs.joc.6b01449.

(2)   Prier, C. K.; Rankic, D. A.; MacMillan, D. W. C. Visible Light Photoredox Catalysis with Transition Metal Complexes: Applications in Organic Synthesis. *Chem Rev* **2013**, *113* (7), 5322–5363. https://doi.org/10.1021/cr300503r.

(3)   Hassaan, M. A.; El-Nemr, M. A.; Elkatory, M. R.; Ragab, S.; Niculescu, V. C.; El Nemr, A. Principles of Photocatalysts and Their Different Applications: A Review. *Topics in Current Chemistry*. Springer Science and Business Media Deutschland GmbH December 1, 2023. https://doi.org/10.1007/s41061-023-00444-7.

(4)   Millet, A.; Cesana, P. T.; Sedillo, K.; Bird, M. J.; Schlau-Cohen, G. S.; Doyle, A. G.; Macmillan, D. W. C.; Scholes, G. D. Bioinspired Supercharging of Photoredox Catalysis for Applications in Energy and Chemical Manufacturing. *Acc Chem Res* **2022**, *55* (10), 1423–1434. https://doi.org/10.1021/acs.accounts.2c00083.

(5)   Connell, T. U. The Forgotten Reagent of Photoredox Catalysis. *Dalton Transactions* **2022**, *51* (35), 13176–13188. https://doi.org/10.1039/d2dt01491b.

(6)   Candish, L.; Collins, K. D.; Cook, G. C.; Douglas, J. J.; Gómez-Suárez, A.; Jolit, A.; Keess, S. Photocatalysis in the Life Science Industry. *Chem Rev* **2022**, *122* (2), 2907–2980. https://doi.org/10.1021/acs.chemrev.1c00416.

(7)   Swierk, J. R. The Cost of Quantum Yield. *Org Process Res Dev* **2023**, *27* (7), 1411–1419. https://doi.org/10.1021/acs.oprd.3c00167.

(8)   Sayre, H. J.; Tian, L.; Son, M.; Hart, S. M.; Liu, X.; Arias-Rotondo, D. M.; Rand, B. P.; Schlau-Cohen, G. S.; Scholes, G. D. Solar Fuels and Feedstocks: The Quest for Renewable Black Gold. *Energy Environ Sci* **2021**, *14* (3), 1402–1419. https://doi.org/10.1039/d0ee03300f.

(9)   Kalyanasundaram, K. Photophysics, Photochemistry and Solar Energy Conversion with Tris(Bipyridyl)Ruthenium(II) and Its Analogues. *Coord Chem Rev* **1982**, *46* (C), 159–244. https://doi.org/10.1016/0010-8545(82)85003-0.

(10)   Dongare, P.; Myron, B. D. B.; Wang, L.; Thompson, D. W.; Meyer, T. J. [Ru(Bpy)3]2+ Revisited. Is It Localized or Delocalized? How Does It Decay? *Coord Chem Rev* **2017**, *345*, 86–107. https://doi.org/10.1016/j.ccr.2017.03.009.

(11)   de Groot, L. H. M.; Ilic, A.; Schwarz, J.; Wärnmark, K. Iron Photoredox Catalysis-Past, Present, and Future. *J Am Chem Soc* **2023**, *145* (17), 9369–9388. https://doi.org/10.1021/jacs.3c01000.

(12)   Iwamura, M.; Takeuchi, S.; Tahara, T. Ultrafast Excited-State Dynamics of Copper(I) Complexes. *Acc Chem Res* **2015**, *48* (3), 782–791. https://doi.org/10.1021/ar500353h.

(13)   Grimm, J. B.; Tkachuk, A. N.; Patel, R.; Hennigan, S. T.; Gutu, A.; Dong, P.; Gandin, V.; Osowski, A. M.; Holland, K. L.; Liu, Z. J.; Brown, T. A.; Lavis, L. D. Optimized Red-Absorbing Dyes for Imaging and Sensing. *J Am Chem Soc* **2023**, *145* (42), 23000–23013. https://doi.org/10.1021/jacs.3c05273.

(14)   Fabian, J.; Nakazumi, H.; Matsuoka, M. Near-Infrared Absorbing Dyes. *Chem. Rev* **1992**, *92* (6), 1197–1226.

(15) Sun, J.; Goldys, E. M. Linear Absorption and Molar Extinction Coefficients in Direct Semiconductor Quantum Dots. *Journal of Physical Chemistry C* **2008**, *112* (25), 9261–9266. https://doi.org/10.1021/jp800700m.

(16) Toufanian, R.; Zhong, X.; Kays, J. C.; Saeboe, A. M.; Dennis, A. M. Correlating ZnSe Quantum Dot Absorption with Particle Size and Concentration. *Chemistry of Materials* **2021**, *33* (18), 7527–7536. https://doi.org/10.1021/acs.chemmater.1c02501.

(17) Jain, P. K.; Lee, K. S.; El-Sayed, I. H.; El-Sayed, M. A. Calculated Absorption and Scattering Properties of Gold Nanoparticles of Different Size, Shape, and Composition: Applications in Biological Imaging and Biomedicine. *Journal of Physical Chemistry B* **2006**, *110* (14), 7238–7248. https://doi.org/10.1021/jp057170o.

(18) Neckel, H. The Solar Radiation Between 3300 and 12500 A. *Sol Phys* **1984**, *90*, 205–258.

(19) Beck, L. R.; Xie, K. A.; Goldschmid, S. L.; Kariofillis, S. K.; Joe, C. L.; Sherwood, T. C.; Sezen-Edmonds, M.; Rovis, T. Red-Shifting Blue Light Photoredox Catalysis for Organic Synthesis: A Graphical Review. *SynOpen* **2023**, *7* (1), 76–87. https://doi.org/10.1055/s-0040-1720060.

(20) Glaser, F.; Kerzig, C.; Wenger, O. S. Sensitization-Initiated Electron Transfer via Upconversion: Mechanism and Photocatalytic Applications. *Chem Sci* **2021**, *12* (29), 9922–9933. https://doi.org/10.1039/d1sc02085d.

(21) Singh-Rachford, T. N.; Castellano, F. N. Photon Upconversion Based on Sensitized Triplet-Triplet Annihilation. *Coord Chem Rev* **2010**, *254* (21–22), 2560–2573. https://doi.org/10.1016/j.ccr.2010.01.003.

(22) Ravetz, B. D.; Pun, A. B.; Churchill, M.; Congreve, D. N.; Rovis, T.; Campos, L. M. Photoredox Catalysis Using Infrared Light via Triplet Fusion Upconversion. *Nature* **2019**, *565*, 343–346. https://doi.org/10.1038/s41586-018-0835-2.

(23) Li, H.; Wang, C.; Glaser, F.; Sinha, N.; Wenger, O. S. Metal-Organic Bichromophore Lowers the Upconversion Excitation Power Threshold and Promotes UV Photoreactions. *J Am Chem Soc* **2023**, *145* (20), 11402–11414. https://doi.org/10.1021/jacs.3c02609.

(24) Mirkovic, T.; Ostroumov, E. E.; Anna, J. M.; Van Grondelle, R.; Govindjee; Scholes, G. D. Light Absorption and Energy Transfer in the Antenna Complexes of Photosynthetic Organisms. *Chem Rev* **2017**, *117* (2), 249–293. https://doi.org/10.1021/acs.chemrev.6b00002.

(25) Scholes, G. D.; Fleming, G. R.; Olaya-Castro, A.; Van Grondelle, R. Lessons from Nature about Solar Light Harvesting. *Nat Chem* **2011**, *3* (10), 763–774. https://doi.org/10.1038/nchem.1145.

(26) Scholes, G. D.; Mirkovic, T.; Turner, D. B.; Fassioli, F.; Buchleitner, A. Solar Light Harvesting by Energy Transfer: From Ecology to Coherence. *Energy Environ Sci* **2012**, *5* (11), 9374–9393. https://doi.org/10.1039/c2ee23013e.

(27) MacColl, R.; Guard-Frier, D. *Phycobiliproteins*, 2018 Reiss.; CRC Press: Boca Raton, Fl, 1987.

(28) Hogewoning, S. W.; Wientjes, E.; Douwstra, P.; Trouwborst, G.; van Ieperen, W.; Croce, R.; Harbinson, J. Photosynthetic Quantum Yield Dynamics: From Photosystems to Leaves. *Plant Cell* **2012**, *24* (5), 1921–1935. https://doi.org/10.1105/tpc.112.097972.

(29) Blankenship, R. E. *Molecular Mechanisms of Photosynthesis*; Blackwell Science Ltd: Oxford, 2002.

(30) Arsenault, E. A.; Yoneda, Y.; Iwai, M.; Niyogi, K. K.; Fleming, G. R. Vibronic Mixing Enables Ultrafast Energy Flow in Light-Harvesting Complex II. *Nat Commun* **2020**, *11* (1). https://doi.org/10.1038/s41467-020-14970-1.

(31) Croce, R.; Van Amerongen, H. Natural Strategies for Photosynthetic Light Harvesting. *Nat Chem Biol* **2014**, *10* (7), 492–501. https://doi.org/10.1038/nchembio.1555.

(32) Sil, S.; Tilluck, R. W.; Mohan T. M, N.; Leslie, C. H.; Rose, J. B.; Domínguez-Martín, M. A.; Lou, W.; Kerfeld, C. A.; Beck, W. F. Excitation Energy Transfer and Vibronic Coherence in Intact Phycobilisomes. *Nat Chem* **2022**, *14* (11), 1286–1294. https://doi.org/10.1038/s41557-022-01026-8.

(33) Watanabe, M.; Ikeuchi, M. Phycobilisome: Architecture of a Light-Harvesting Supercomplex. *Photosynth Res* **2013**, *116* (2–3), 265–276. https://doi.org/10.1007/s11120-013-9905-3.

(34) Zhang, J.; Ma, J.; Liu, D.; Qin, S.; Sun, S.; Zhao, J.; Sui, S. F. Structure of Phycobilisome from the Red Alga Griffithsia Pacifica. *Nature* **2017**, *551* (7678), 57–63. https://doi.org/10.1038/nature24278.

(35) Ma, J.; You, X.; Sun, S.; Wang, X.; Qin, S.; Sui, S. F. Structural Basis of Energy Transfer in Porphyridium Purpureum Phycobilisome. *Nature* **2020**, *579* (7797), 146–151. https://doi.org/10.1038/s41586-020-2020-7.

(36) Cogdell, R. J.; Isaacs, N. W.; Freer, A. A.; Howard, T. D.; Gardiner, A. T.; Prince, S. M.; Papiz, M. Z. The Structural Basis of Light-Harvesting in Purple Bacteria. *FEBS Lett* **2003**, *555*, 35–39. https://doi.org/10.1016/S0014-5793(03)01102-5.

(37) Scheuring, S.; Sturgis, J. N. Chromatic Adaptation of Photosynthetic Membranes. *Science* **2005**, *309*, 484–487.

(38) Wang, D.; Fiebig, O. C.; Harris, D.; Toporik, H.; Ji, Y. I.; Chuang, C.; Nairat, M.; Tong, A. L.; Ogren, J. I.; Hart, S. M.; Cao, J. I.; Sturgis, J. N.; Mazor, Y.; Schlau-Cohen, G. S. Elucidating Interprotein Energy Transfer Dynamics within the Antenna Network from Purple Bacteria *PNAS* **2023**, *120* (28), e220477120. https://doi.org/10.1073/pnas.

(39) Fiebig, O. C.; Harris, D.; Wang, D.; Hoffmann, M. P.; Schlau-Cohen, G. S. Ultrafast Dynamics of Photosynthetic Light Harvesting: Strategies for Acclimation Across Organisms. *Annu Rev Phys Chem* **2023**, *74*, 493–520. https://doi.org/10.1146/annurev-physchem-083122.

(40) Collini, E.; Curutchet, C.; Mirkovic, T.; Scholes, G. D. Electronic Energy Transfer in Photosynthetic Antenna Systems. In *Energy Transfer Dynamics in Biomaterial Systems*; Springer Berlin Heidelberg: Berlin, Heidelberg, 2009; pp 3–34. https://doi.org/10.1007/978-3-642-02306-4_1.

(41) Zhang, B.; Sun, L. Artificial Photosynthesis: Opportunities and Challenges of Molecular Catalysts. *Chem Soc Rev* **2019**, *48* (7), 2216–2264. https://doi.org/10.1039/c8cs00897c.

(42) Frischmann, P. D.; Mahata, K.; Würthner, F. Powering the Future of Molecular Artificial Photosynthesis with Light-Harvesting Metallosupramolecular Dye Assemblies. *Chem Soc Rev* **2013**, *42* (4), 1847–1870. https://doi.org/10.1039/c2cs35223k.

(43) Ham, R.; Nielsen, C. J.; Pullen, S.; Reek, J. N. H. Supramolecular Coordination Cages for Artificial Photosynthesis and Synthetic Photocatalysis. *Chem Rev* **2023**, *123* (9), 5225–5261. https://doi.org/10.1021/acs.chemrev.2c00759.

(44) Valeur, B.; Berberan-Santos, M. N. *Molecular Fluorescence: Principles and Applications*, 2nd ed.; Wiley-VCH: Weinheim, Germany, 2012.

(45)   Dubose, J. T.; Kamat, P. V. Energy Versus Electron Transfer: Managing Excited-State Interactions in Perovskite Nanocrystal-Molecular Hybrids. *Chem Rev* **2022**, *122* (15), 12475–12494. https://doi.org/10.1021/acs.chemrev.2c00172.

(46)   Sk, B.; Hirata, S. Förster Resonance Energy Transfer Involving the Triplet State. *Chemical Communications* **2023**, *59* (44), 6643–6659. https://doi.org/10.1039/d3cc00748k.

(47)   Giera, W.; Szewczyk, S.; McConnell, M. D.; Redding, K. E.; van Grondelle, R.; Gibasiewicz, K. Uphill Energy Transfer in Photosystem I from Chlamydomonas Reinhardtii. Time-Resolved Fluorescence Measurements at 77 K. *Photosynth Res* **2018**, *137* (2), 321–335. https://doi.org/10.1007/s11120-018-0506-z.

(48)   Kosugi, M.; Ozawa, S. I.; Takahashi, Y.; Kamei, Y.; Itoh, S.; Kudoh, S.; Kashino, Y.; Koike, H. Red-Shifted Chlorophyll a Bands Allow Uphill Energy Transfer to Photosystem II Reaction Centers in an Aerial Green Alga, Prasiola Crispa, Harvested in Antarctica. *Biochim Biophys Acta Bioenerg* **2020**, *1861* (2). https://doi.org/10.1016/j.bbabio.2019.148139.

(49)   Cesana, P. T.; Li, B. X.; Shepard, S. G.; Ting, S. I.; Hart, S. M.; Olson, C. M.; Martinez Alvarado, J. I.; Son, M.; Steiman, T. J.; Castellano, F. N.; Doyle, A. G.; MacMillan, D. W. C.; Schlau-Cohen, G. S. A Biohybrid Strategy for Enabling Photoredox Catalysis with Low-Energy Light. *Chem* **2022**, *8*, 174–185. https://doi.org/10.1016/j.chempr.2021.10.010.

(50)   Kosugi, M.; Kawasaki, M.; Shibata, Y.; Hara, K.; Takaichi, S.; Moriya, T.; Adachi, N.; Kamei, Y.; Kashino, Y.; Kudoh, S.; Koike, H.; Senda, T. Uphill Energy Transfer Mechanism for Photosynthesis in an Antarctic Alga. *Nat Commun* **2023**, *14* (1). https://doi.org/10.1038/s41467-023-36245-1.

(51)   Marcus, R. A.; Sutin, N. Electron Transfers in Chemistry and Biology. *Biochim Biophys Acta* **1985**, *811* (3), 265–322.

(52)   Buscemi, G.; Trotta, M.; Vona, D.; Farinola, G. M.; Milano, F.; Ragni, R. Supramolecular Biohybrid Construct for Photoconversion Based on a Bacterial Reaction Center Covalently Bound to Cytochrome c by an Organic Light Harvesting Bridge. *Bioconjug Chem* **2023**, *34* (4), 629–637. https://doi.org/10.1021/acs.bioconjchem.2c00527.

(53)   Amoruso, G.; Liu, J.; Polak, D. W.; Tiwari, K.; Jones, M. R.; Oliver, T. A. A. High-Efficiency Excitation Energy Transfer in Biohybrid Quantum Dot-Bacterial Reaction Center Nanoconjugates. *Journal of Physical Chemistry Letters* **2021**, *12* (23), 5448–5455. https://doi.org/10.1021/acs.jpclett.1c01407.

(54)   Hassan Omar, O.; La Gatta, S.; Tangorra, R. R.; Milano, F.; Ragni, R.; Operamolla, A.; Argazzi, R.; Chiorboli, C.; Agostiano, A.; Trotta, M.; Farinola, G. M. Synthetic Antenna Functioning As Light Harvester in the Whole Visible Region for Enhanced Hybrid Photosynthetic Reaction Centers. *Bioconjug Chem* **2016**, *27* (7), 1614–1623. https://doi.org/10.1021/acs.bioconjchem.6b00175.

(55)   Grzyb, J.; Walczewska-Szewc, K.; Sławski, J.; Trojnar, M. Quantum Dot Clusters as Self-Assembled Antennae with Phycocyanine and Phycobilisomes as Energy Acceptors. *Physical Chemistry Chemical Physics* **2021**, *23* (42), 24505–24517. https://doi.org/10.1039/d1cp03347f.

(56)   Yoneda, Y.; Noji, T.; Mizutani, N.; Kato, D.; Kondo, M.; Miyasaka, H.; Nagasawa, Y.; Dewa, T. Energy Transfer Dynamics and the Mechanism of Biohybrid Photosynthetic Antenna Complexes Chemically Linked with Artificial Chromophores. *Physical Chemistry Chemical Physics* **2022**, *24* (40), 24714–24726. https://doi.org/10.1039/d2cp02465a.

(57)   Wang, Y.; Zhu, R.; Hang, Y.; Wang, R.; Dong, R.; Yu, S.; Xing, L. B. Artificial Supramolecular Light-Harvesting Systems Based on a Pyrene Derivative for Photochemical Catalysis. *Polym Chem* **2022**, *14* (3), 248–252. https://doi.org/10.1039/d2py01344d.

(58)   Strieth-Kalthoff, F.; Glorius, F. Triplet Energy Transfer Photocatalysis: Unlocking the Next Level. *Chem* **2020**, *6* (8), 1888–1903. https://doi.org/10.1016/j.chempr.2020.07.010.

(59)   Ghosh, I.; Shaikh, R. S.; König, B. Sensitization-Initiated Electron Transfer for Photoredox Catalysis. *Angewandte Chemie International Edition* **2017**, *56*, 8544–8549. https://doi.org/10.1002/ange.201703004.

(60)   Zuo, Z.; Ahneman, D. T.; Chu, L.; Terrett, J. A.; Doyle, A. G.; Macmillan, D. W. C. Merging Photoredox with Nickel Catalysis: Coupling of α-Carboxyl Sp 3-Carbons with Aryl Halides. *Science (1979)* **2014**, *345* (6195), 437–440.

(61)   Cagan, D. A.; Bím, D.; Kazmierczak, N. P.; Hadt, R. G. Mechanisms of Photoredox Catalysis Featuring Nickel-Bipyridine Complexes. *ACS Catalysis* **2024**, *14* (11), 9055–9076. https://doi.org/10.1021/acscatal.4c02036.

(62)   Tian, L.; Till, N. A.; Kudisch, B.; MacMillan, D. W. C.; Scholes, G. D. Transient Absorption Spectroscopy Offers Mechanistic Insights for an Iridium/Nickel-Catalyzed C-O Coupling. *J Am Chem Soc* **2020**, *142* (10), 4555–4559. https://doi.org/10.1021/jacs.9b12835.

(63)   Ting, S. I.; Garakyaraghi, S.; Taliaferro, C. M.; Shields, B. J.; Scholes, G. D.; Castellano, F. N.; Doyle, A. G. D-d Excited States of Ni(II) Complexes Relevant to Photoredox Catalysis: Spectroscopic Identification and Mechanistic Implications. *J Am Chem Soc* **2020**, *142* (12), 5800–5810. https://doi.org/10.1021/jacs.0c00781.

(64)   Xia, C.; Wu, W.; Yu, T.; Xie, X.; Van Oversteeg, C.; Gerritsen, H. C.; De Mello Donega, C. Size-Dependent Band-Gap and Molar Absorption Coefficients of Colloidal CuInS2 Quantum Dots. *ACS Nano* **2018**, *12* (8), 8350–8361. https://doi.org/10.1021/acsnano.8b03641.

(65)   Mulfort, K. L.; Utschig, L. M. Modular Homogeneous Chromophore-Catalyst Assemblies. *Acc Chem Res* **2016**, *49* (5), 835–843. https://doi.org/10.1021/acs.accounts.5b00539.

(66)   Soltau, S. R.; Dahlberg, P. D.; Niklas, J.; Poluektov, O. G.; Mulfort, K. L.; Utschig, L. M. Ru-Protein-Co Biohybrids Designed for Solar Hydrogen Production: Understanding Electron Transfer Pathways Related to Photocatalytic Function. *Chem Sci* **2016**, *7* (12), 7068–7078. https://doi.org/10.1039/C6SC03121H.

(67)   Soltau, S. R.; Niklas, J.; Dahlberg, P. D.; Poluektov, O. G.; Tiede, D. M.; Mulfort, K. L.; Utschig, L. M. Aqueous Light Driven Hydrogen Production by a Ru-Ferredoxin-Co Biohybrid. *Chemical Communications* **2015**, *51* (53), 10628–10631. https://doi.org/10.1039/c5cc03006d.

(68)   Utschig, L. M.; Brahmachari, U.; Mulfort, K. L.; Niklas, J.; Poluektov, O. G. Biohybrid Photosynthetic Charge Accumulation Detected by Flavin Semiquinone Formation in Ferredoxin-NADP+ Reductase. *Chem Sci* **2022**, *13* (22), 6502–6511. https://doi.org/10.1039/d2sc01546c.

(69)   Utterback, J. K.; Ruzicka, J. L.; Keller, H. R.; Pellows, L. M.; Dukovic, G. Electron Transfer from Semiconductor Nanocrystals to Redox Enzymes. *Annu Rev Phys Chem* **2020**, *71*, 335–359. https://doi.org/10.1146/annurev-physchem-050317-014232.

(70)   Clinger, A.; Yang, Z. Y.; Pellows, L. M.; King, P.; Mus, F.; Peters, J. W.; Dukovic, G.; Seefeldt, L. C. Hole-Scavenging in Photo-Driven N2 Reduction Catalyzed by a CdS-Nitrogenase MoFe Protein Biohybrid System. *J Inorg Biochem* **2024**, *253*. https://doi.org/10.1016/j.jinorgbio.2024.112484.

(71) Brown, K. A.; Ruzicka, J.; Kallas, H.; Chica, B.; Mulder, D. W.; Peters, J. W.; Seefeldt, L. C.; Dukovic, G.; King, P. W. Excitation-Rate Determines Product Stoichiometry in Photochemical Ammonia Production by CdS Quantum Dot-Nitrogenase MoFe Protein Complexes. *ACS Catal* **2020**, *10* (19), 11147–11152. https://doi.org/10.1021/acscatal.0c02933.

(72) Brown, K. A.; Harris, D. F.; Wilker, M. B.; Rasmussen, A.; Khadka, N.; Hamby, H.; Keable, S.; Dukovic, G.; Peters, J. W.; Seefeldt, L. C.; King, P. W. Light-Driven Dinitrogen Reduction Catalyzed by a CdS:Nitrogenase MoFe Protein Biohybrid. *Science* **2016**, *352* (6284), 448–450. https://doi.org/10.1126/science.aaf2091.

(73) Huang, J.; Zarzycki, J.; Gunner, M. R.; Parson, W. W.; Kern, J. F.; Yano, J.; Ducat, D. C.; Kramer, D. M. Mesoscopic to Macroscopic Electron Transfer by Hopping in a Crystal Network of Cytochromes. *J Am Chem Soc* **2020**, *142* (23), 10459–10467. https://doi.org/10.1021/jacs.0c02729.

(74) Yuan, Y.; Jin, N.; Saghy, P.; Dube, L.; Zhu, H.; Chen, O. Quantum Dot Photocatalysts for Organic Transformations. *Journal of Physical Chemistry Letters* **2021**, *12* (30), 7180–7193. https://doi.org/10.1021/acs.jpclett.1c01717.

(75) Michalet, X.; Pinaud, F. F.; Bentolila, L. A.; Tsay, J. M.; Doose, S.; Li, J. J.; Sundaresan, G.; Wu, A. M.; Gambhir, S. S.; Weiss, S. Quantum Dots for Live Cells, in Vivo Imaging, and Diagnostics. *Science* **2005**, *307* (5709), 538–544.

(76) Ravetz, B. D.; Tay, N. E. S.; Joe, C. L.; Sezen-Edmonds, M.; Schmidt, M. A.; Tan, Y.; Janey, J. M.; Eastgate, M. D.; Rovis, T. Development of a Platform for Near-Infrared Photoredox Catalysis. *ACS Cent Sci* **2020**, *6* (11), 2053–2059. https://doi.org/10.1021/acscentsci.0c00948.

(77) Buksh, B. F.; Knutson, S. D.; Oakley, J. V.; Bissonnette, N. B.; Oblinsky, D. G.; Schwoerer, M. P.; Seath, C. P.; Geri, J. B.; Rodriguez-Rivera, F. P.; Parker, D. L.; Scholes, G. D.; Ploss, A.; MacMillan, D. W. C. MMap-Red: Proximity Labeling by Red Light Photocatalysis. *J Am Chem Soc* **2022**, *144* (14), 6154–6162. https://doi.org/10.1021/jacs.2c01384.

(78) Xie, K. A.; Bednarova, E.; Joe, C. L.; Lin, C.; Sherwood, T. C.; Simmons, E. M.; Lainhart, B. C.; Rovis, T. Orange Light-Driven C(Sp2)-C(Sp3) Cross-Coupling via Spin-Forbidden Ir(III) Metallaphotoredox Catalysis. *J Am Chem Soc* **2023**, *145* (36), 19925–19931. https://doi.org/10.1021/jacs.3c06285.

(79) Cabanero, D. C.; Nguyen, J. A.; Cazin, C. S. J.; Nolan, S. P.; Rovis, T. Deep Red to Near-Infrared Light-Controlled Ruthenium-Catalyzed Olefin Metathesis. *ACS Catal* **2023**, *13* (7), 4384–4390. https://doi.org/10.1021/acscatal.3c00473.

(80) Goldschmid, S. L.; Soon Tay, N. E.; Joe, C. L.; Lainhart, B. C.; Sherwood, T. C.; Simmons, E. M.; Sezen-Edmonds, M.; Rovis, T. Overcoming Photochemical Limitations in Metallaphotoredox Catalysis: Red-Light-Driven C-N Cross-Coupling. *J Am Chem Soc* **2022**, *144* (49), 22409–22415. https://doi.org/10.1021/jacs.2c09745.

(81) Shi, J.; Su, Z.; Li, X.; Feng, J.; Men, C. Impacts of Host-Guest Assembly on the Photophysical and Photocatalytic Properties of Heterogenized Molecular Photosensitizer and Catalysts. *J Mater Chem A Mater* **2023**, *11* (13), 6646–6658. https://doi.org/10.1039/d2ta09715j.

(82) Ma, X.; Zhao, Y. Biomedical Applications of Supramolecular Systems Based on Host-Guest Interactions. *Chem Rev* **2015**, *115* (15), 7794–7839. https://doi.org/10.1021/cr500392w.

(83) Fernando, P. U. A. I.; Shepelytskyi, Y.; Cesana, P. T.; Wade, A.; Grynko, V.; Mendieta, A. M.; Seveney, L. E.; Brown, J. D.; Hane, F. T.; Albert, M. S.; Deboef, B. Decacationic

Pillar[5]Arene: A New Scaffold for the Development of 129Xe MRI Imaging Agents. *ACS Omega* **2020**, *5* (43), 27783–27788. https://doi.org/10.1021/acsomega.0c02565.

(84) Komulainen, S.; Iresh Fernando, P. U. A.; Mareš, J.; Selent, A.; Khalili, R.; Cesana, P. T.; Ebeling, A.; Kantola, A. M.; Beyeh, N. K.; Rissanen, K.; DeBoef, B.; Lantto, P.; Telkki, V. V. Encapsulation of Xenon by Bridged Resorcinarene Cages with High 129Xe NMR Chemical Shift and Efficient Exchange Dynamics. *Cell Rep Phys Sci* **2023**, *4* (2). https://doi.org/10.1016/j.xcrp.2023.101281.

(85) Li, H.; Yang, J.; Li, D.; Li, X.; Li, J.; He, C. Host-Guest Approach to Promoting Photocatalysis Based on Consecutive Photo-Induced Electron-Transfer Processes via Efficient Förster Resonance Energy Transfer. *Angewandte Chemie International Edition* **2024**, e202409094. https://doi.org/10.1002/anie.202409094.

(86) Li, Y.; Li, N.; Li, G.; Qiao, Y.; Zhang, M.; Zhang, L.; Guo, Q. H.; He, G. The Green Box: Selenoviologen-Based Tetracationic Cyclophane for Electrochromism, Host-Guest Interactions, and Visible-Light Photocatalysis. *J Am Chem Soc* **2023**, *145* (16), 9118–9128. https://doi.org/10.1021/jacs.3c00800.

(87) Huang, L.; Han, G. Triplet–Triplet Annihilation Photon Upconversion-Mediated Photochemical Reactions. *Nat Rev Chem* **2024**, *8* (4), 238–255. https://doi.org/10.1038/s41570-024-00585-3.

(88) Awwad, N.; Bui, A. T.; Danilov, E. O.; Castellano, F. N. Visible-Light-Initiated Free-Radical Polymerization by Homomolecular Triplet-Triplet Annihilation. *Chem* **2020**, *6* (11), 3071–3085. https://doi.org/10.1016/j.chempr.2020.08.019.

(89) Bilger, J. B.; Kerzig, C.; Larsen, C. B.; Wenger, O. S. A Photorobust Mo(0) Complex Mimicking [Os(2,2′-Bipyridine)3]2+and Its Application in Red-to-Blue Upconversion. *J Am Chem Soc* **2021**, *143* (3), 1651–1663. https://doi.org/10.1021/jacs.0c12805.

(90) Wellauer, J.; Ziereisen, F.; Sinha, N.; Prescimone, A.; Velić, A.; Meyer, F.; Wenger, O. S. Iron(III) Carbene Complexes with Tunable Excited State Energies for Photoredox and Upconversion. *J Am Chem Soc* **2024**. https://doi.org/10.1021/jacs.4c00605.

(91) Wang, C.; Wegeberg, C.; Wenger, O. S. First-Row D6 Metal Complex Enables Photon Upconversion and Initiates Blue Light-Dependent Polymerization with Red Light. *Angewandte Chemie - International Edition* **2023**, *62* (43), e202311470. https://doi.org/10.1002/anie.202311470.

(92) Douglas, J. J.; Sevrin, M. J.; Stephenson, C. R. J. Visible Light Photocatalysis: Applications and New Disconnections in the Synthesis of Pharmaceutical Agents. *Org Process Res Dev* **2016**, *20* (7), 1134–1147. https://doi.org/10.1021/acs.oprd.6b00125.

(93) Fagnoni, M.; Dondi, D.; Ravelli, D.; Albini, A. Photocatalysis for the Formation of the C-C Bond. *Chem Rev* **2007**, *107* (6), 2725–2756. https://doi.org/10.1021/cr068352x.

(94) Osterloh, F. E. Photocatalysis versus Photosynthesis: A Sensitivity Analysis of Devices for Solar Energy Conversion and Chemical Transformations. *ACS Energy Lett* **2017**, *2* (2), 445–453. https://doi.org/10.1021/acsenergylett.6b00665.

(95) Zhu, S.; Wang, D. Photocatalysis: Basic Principles, Diverse Forms of Implementations and Emerging Scientific Opportunities. *Adv Energy Mater* **2017**, *7* (23), 1700841. https://doi.org/10.1002/aenm.201700841.

(96) Turro, N. J. Energy Transfer Processes. *Pure and Applied Chemistry* **1977**, *49* (4), 405–429. https://doi.org/https://doi.org/10.7916/D8RV0V0T.

(97) Kavarnos, G. J.; Turro, N. J. Photosensitization by Reversible Electron Transfer: Theories, Experimental Evidence, and Examples. *Chem Rev* **1986**, *86* (2), 401–449. https://doi.org/https://doi.org/10.1021/cr00072a005.

(98) Prier, C. K.; Rankic, D. A.; MacMillan, D. W. C. Visible Light Photoredox Catalysis with Transition Metal Complexes: Applications in Organic Synthesis. *Chem Rev* **2013**, *113* (7), 5322–5363. https://doi.org/10.1021/cr300503r.

(99) Cheng, W. M.; Shang, R. Transition Metal-Catalyzed Organic Reactions under Visible Light: Recent Developments and Future Perspectives. *ACS Catal* **2020**, *10* (16), 9170–9196. https://doi.org/10.1021/acscatal.0c01979.

(100) Shaw, M. H.; Twilton, J.; MacMillan, D. W. C. Photoredox Catalysis in Organic Chemistry. *Journal of Organic Chemistry* **2016**, *81* (16), 6898–6926. https://doi.org/10.1021/acs.joc.6b01449.

(101) Xuan, J.; Xiao, W. J. Visible-Light Photoredox Catalysis. *Angewandte Chemie - International Edition* **2012**, *51* (28), 6828–6838. https://doi.org/10.1002/anie.201200223.

(102) Romero, N. A.; Nicewicz, D. A. Organic Photoredox Catalysis. *Chem Rev* **2016**, *116* (17), 10075–10166. https://doi.org/10.1021/acs.chemrev.6b00057.

(103) Tucker, J. W.; Stephenson, C. R. J. Shining Light on Photoredox Catalysis: Theory and Synthetic Applications. *Journal of Organic Chemistry* **2012**, *77* (4), 1617–1622. https://doi.org/10.1021/jo202538x.

(104) Sayre, H. J.; Tian, L.; Son, M.; Hart, S. M.; Liu, X.; Arias-Rotondo, D. M.; Rand, B. P.; Schlau-Cohen, G. S.; Scholes, G. D. Solar Fuels and Feedstocks: The Quest for Renewable Black Gold. *Energy Environ Sci* **2021**, *14* (3), 1402–1419. https://doi.org/10.1039/d0ee03300f.

(105) McCusker, J. K. Electronic Structure in the Transition Metal Block and Its Implications for Light Harvesting. *Science* **2019**, *363* (6426), 484–488. https://doi.org/10.1126/science.aav9104.

(106) Shaw, G. B.; Styers-Barnett, D. J.; Gannon, E. Z.; Granger, J. C.; Papanikolas, J. M. Interligand Electron Transfer Dynamics in [Os(Bpy) 3] 2+: Exploring the Excited State Potential Surfaces with Femtosecond Spectroscopy. *Journal of Physical Chemistry A* **2004**, *108* (23), 4998–5006. https://doi.org/10.1021/jp0363850.

(107) Dongare, P.; Myron, B. D. B.; Wang, L.; Thompson, D. W.; Meyer, T. J. [Ru(Bpy)3]2+ Revisited. Is It Localized or Delocalized? How Does It Decay? *Coord Chem Rev* **2017**, *345*, 86–107. https://doi.org/10.1016/j.ccr.2017.03.009.

(108) McCusker, J. K. Femtosecond Absorption Spectroscopy of Transition Metal Charge-Transfer Complexes. *Acc Chem Res* **2003**, *36* (12), 876–887. https://doi.org/10.1021/ar030111d.

(109) Li, P.; Terrett, J. A.; Zbieg, J. R. Visible-Light Photocatalysis as an Enabling Technology for Drug Discovery: A Paradigm Shift for Chemical Reactivity. *ACS Med Chem Lett* **2020**, *11* (11), 2120–2130. https://doi.org/10.1021/acsmedchemlett.0c00436.

(110) Weng, Y.; Song, C.; Chiang, C. W.; Lei, A. Single Electron Transfer-Based Peptide/Protein Bioconjugations Driven by Biocompatible Energy Input. *Commun Chem* **2020**, *3* (1), 1–11. https://doi.org/10.1038/s42004-020-00413-x.

(111) Bottecchia, C.; Noël, T. Photocatalytic Modification of Amino Acids, Peptides, and Proteins. *Chemistry - A European Journal* **2019**, *25* (1), 26–42. https://doi.org/10.1002/chem.201803074.

(112) Ryu, K. A.; Kaszuba, C. M.; Bissonnette, N. B.; Oslund, R. C.; Fadeyi, O. O. Interrogating Biological Systems Using Visible-Light-Powered Catalysis. *Nat Rev Chem* **2021**, *5* (5), 322–337. https://doi.org/10.1038/s41570-021-00265-6.

(113) Mirkovic, T.; Ostroumov, E. E.; Anna, J. M.; Van Grondelle, R.; Govindjee; Scholes, G. D. Light Absorption and Energy Transfer in the Antenna Complexes of Photosynthetic Organisms. *Chem Rev* **2017**, *117* (2), 249–293. https://doi.org/10.1021/acs.chemrev.6b00002.

(114) Frank, H. A.; Cogdell, R. J. *Light Capture in Photosynthesis*; Elsevier Ltd., 2012; Vol. 8. https://doi.org/10.1016/B978-0-12-374920-8.00808-0.

(115) Watanabe, M.; Ikeuchi, M. Phycobilisome: Architecture of a Light-Harvesting Supercomplex. *Photosynth Res* **2013**, *116* (2–3), 265–276. https://doi.org/10.1007/s11120-013-9905-3.

(116) Ma, J.; You, X.; Sun, S.; Wang, X.; Qin, S.; Sui, S. F. Structural Basis of Energy Transfer in Porphyridium Purpureum Phycobilisome. *Nature* **2020**, *579* (7797), 146–151. https://doi.org/10.1038/s41586-020-2020-7.

(117) Zhang, J.; Ma, J.; Liu, D.; Qin, S.; Sun, S.; Zhao, J.; Sui, S. F. Structure of Phycobilisome from the Red Alga Griffithsia Pacifica. *Nature* **2017**, *551* (7678), 57–63. https://doi.org/10.1038/nature24278.

(118) Saer, R. G.; Blankenship, R. E. Light Harvesting in Phototrophic Bacteria: Structure and Function. *Biochemical Journal* **2017**, *474* (13), 2107–2131. https://doi.org/10.1042/BCJ20160753.

(119) Chen, H.; Dang, W.; Xie, J.; Zhao, J.; Weng, Y. Ultrafast Energy Transfer Pathways in R-Phycoerythrin from Polysiphonia Urceolata. *Photosynth Res* **2012**, *111* (1–2), 81–86. https://doi.org/10.1007/s11120-011-9708-3.

(120) Gaigalas, A.; Gallagher, T.; Cole, K. D.; Singh, T.; Wang, L.; Zhang, Y.-Z. A Multistate Model for the Fluorescence Response of R-Phycoerythrin. *Photochem Photobiol* **2006**, *82* (3), 635. https://doi.org/10.1562/2005-05-26-ra-544.

(121) Seibert, M.; Connolly, J. S. Fluorescence Properties of C-Phycocyanin Isolated From a Thermophilic Cyanobacterium. *Photochem Photobiol* **1984**, *40* (2), 267–271. https://doi.org/10.1111/j.1751-1097.1984.tb04585.x.

(122) O'Carra, P.; O'Heocha, C.; Carrol, D. M. Spectral Properties of the Phycobilins. II. Phycoerythrobilin. *Biochemistry* **1964**, *3* (9), 1343–1350. https://doi.org/10.1021/bi00897a026.

(123) MacColl, R.; Guard-Frier, D. *Phycobiliproteins*, 2018 Reiss.; CRC Press: Boca Raton, Fl, 1987.

(124) Mulfort, K. L.; Utschig, L. M. Modular Homogeneous Chromophore-Catalyst Assemblies. *Acc Chem Res* **2016**, *49* (5), 835–843. https://doi.org/10.1021/acs.accounts.5b00539.

(125) Soltau, S. R.; Dahlberg, P. D.; Niklas, J.; Poluektov, O. G.; Mulfort, K. L.; Utschig, L. M. Ru-Protein-Co Biohybrids Designed for Solar Hydrogen Production: Understanding Electron Transfer Pathways Related to Photocatalytic Function. *Chem Sci* **2016**, *7* (12), 7068–7078. https://doi.org/10.1039/C6SC03121H.

(126) Kathiravan, A.; Chandramohan, M.; Renganathan, R.; Sekar, S. Photoinduced Electron Transfer from Phycoerythrin to Colloidal Metal Semiconductor Nanoparticles. *Spectrochim Acta A Mol Biomol Spectrosc.* **2009**, *72* (3), 496–501. https://doi.org/10.1016/j.saa.2008.10.021.

(127) Proppe, A. H.; Li, Y. C.; Aspuru-Guzik, A.; Berlinguette, C. P.; Chang, C. J.; Cogdell, R.; Doyle, A. G.; Flick, J.; Gabor, N. M.; van Grondelle, R.; Hammes-Schiffer, S.; Jaffer, S. A.; Kelley, S. O.; Leclerc, M.; Leo, K.; Mallouk, T. E.; Narang, P.; Schlau-Cohen, G. S.; Scholes, G. D.; Vojvodic, A.; Yam, V. W. W.; Yang, J. Y.; Sargent, E. H. Bioinspiration in Light Harvesting and Catalysis. *Nat Rev Mater* **2020**, *5* (11), 828–846. https://doi.org/10.1038/s41578-020-0222-0.

(128) Grimme, R. A.; Lubner, C. E.; Bryant, D. A.; Golbeck, J. H. Photosystem I/Molecular Wire/Metal Nanoparticle Bioconjugates for the Photocatalytic Production of H2. *J Am Chem Soc* **2008**, *130* (20), 6308–6309. https://doi.org/10.1021/ja800923y.

(129) Edwards, E. H.; Bren, K. L. Light-Driven Catalysis with Engineered Enzymes and Biomimetic Systems. *Biotechnol Appl Biochem* **2020**, *67* (4), 463–483. https://doi.org/10.1002/bab.1976.

(130) Brown, K. A.; Wilker, M. B.; Boehm, M.; Hamby, H.; Dukovic, G.; King, P. W. Photocatalytic Regeneration of Nicotinamide Cofactors by Quantum Dot-Enzyme Biohybrid Complexes. *ACS Catal* **2016**, *6* (4), 2201–2204. https://doi.org/10.1021/acscatal.5b02850.

(131) Herman, L.; Ghosh, S.; Defrancq, E.; Mesmaeker, A. K. De. Ru(II) Complexes and Light: Molecular Tools for Biomolecules. *J Phys Org Chem* **2008**, *21* (7–8), 670–681. https://doi.org/10.1002/poc.1355.

(132) Schwochert, T. D.; Cruz, C. L.; Watters, J. W.; Reynolds, E. W.; Nicewicz, D. A.; Brustad, E. M. Design and Evaluation of Artificial Hybrid Photoredox Biocatalysts. *ChemBioChem* **2020**, *21* (21), 3146–3150. https://doi.org/10.1002/cbic.202000362.

(133) Utterback, J. K.; Ruzicka, J. L.; Keller, H. R.; Pellows, L. M.; Dukovic, G. Electron Transfer from Semiconductor Nanocrystals to Redox Enzymes. *Annu Rev Phys Chem* **2020**, *71*, 335–359. https://doi.org/10.1146/annurev-physchem-050317-014232.

(134) Wilker, M. B.; Shinopoulos, K. E.; Brown, K. A.; Mulder, D. W.; King, P. W.; Dukovic, G. Electron Transfer Kinetics in CdS Nanorod-[FeFe]-Hydrogenase Complexes and Implications for Photochemical H2 Generation. *J Am Chem Soc* **2014**, *136* (11), 4316–4324. https://doi.org/10.1021/ja413001p.

(135) Arias-Rotondo, D. M.; McCusker, J. K. The Photophysics of Photoredox Catalysis: A Roadmap for Catalyst Design. *Chem Soc Rev* **2016**, *45* (21), 5803–5820. https://doi.org/10.1039/c6cs00526h.

(136) Rupp, M.; Auvray, T.; Rousset, E.; Mercier, G. M.; Marvaud, V.; Kurth, D. G.; Hanan, G. S. Photocatalytic Hydrogen Evolution Driven by a Heteroleptic Ruthenium(II) Bis(Terpyridine) Complex. *Inorg Chem* **2019**, *58* (14), 9127–9134. https://doi.org/10.1021/acs.inorgchem.9b00698.

(137) Ma, B.; Chen, G.; Fave, C.; Chen, L.; Kuriki, R.; Maeda, K.; Ishitani, O.; Lau, T.-C.; Bonin, J.; Robert, M. Efficient Visible-Light-Driven CO 2 Reduction by a Cobalt Molecular Catalyst Covalently Linked to Mesoporous Carbon Nitride. *J Am Chem Soc* **2020**, *142* (13), 6188–6195. https://doi.org/10.1021/jacs.9b13930.

(138) Scandola, F.; Indelli, M. T.; Chiorboli, C.; Bignozzi, C. A. Photoinduced Electron and Energy Transfer in Polynuclear Complexes. *Top Curr Chem* **1990**, *158*, 73–149. https://doi.org/https://doi.org/10.1007/3-540-52568-8_3.

(139) Strieth-Kalthoff, F.; James, M. J.; Teders, M.; Pitzer, L.; Glorius, F. Energy Transfer Catalysis Mediated by Visible Light: Principles, Applications, Directions. *Chem Soc Rev* **2018**, *47* (19), 7190–7202. https://doi.org/10.1039/c8cs00054a.

(140) Frischmann, P. D.; Mahata, K.; Würthner, F. Powering the Future of Molecular Artificial Photosynthesis with Light-Harvesting Metallosupramolecular Dye Assemblies. *Chem Soc Rev* **2013**, *42* (4), 1847–1870. https://doi.org/10.1039/c2cs35223k.

(141) Kimura, E.; Wada, S.; Shionoya, M.; Okazaki, Y. New Series of Multifunctionalized Nickel (II)-Cyclam (Cyclam = 1,4,8,11-Tetraazacyclotetradecane) Complexes. Application to the Photoreduction of Carbon Dioxide. *Inorg Chem* **1994**, *33* (4), 770–778. https://doi.org/https://doi.org/10.1021/ic00082a025.

(142) Hennessey, S.; Farràs, P.; Benet-Buchholz, J.; Llobet, A. A Bpp-Based Dinuclear Ruthenium Photocatalyst for Visible Light-Driven Oxidation Reactions. *Catal Sci Technol* **2019**, *9* (23), 6760–6768. https://doi.org/10.1039/c9cy01796h.

(143) Yamazaki, Y.; Ishitani, O. Synthesis of Os(II)-Re(i)-Ru(II) Hetero-Trinuclear Complexes and Their Photophysical Properties and Photocatalytic Abilities. *Chem Sci* **2018**, *9* (4), 1031–1041. https://doi.org/10.1039/c7sc04162d.

(144) Liu, Y. X.; Summers, M. A.; Scully, S. R.; McGehee, M. D. Resonance Energy Transfer from Organic Chromophores to Fullerene Molecules. *J Appl Phys* **2006**, *99* (9), 093251-(1-4). https://doi.org/10.1063/1.2195890.

(145) Cerfontaine, S.; Wehlin, S. A. M.; Elias, B.; Troian-Gautier, L. Photostable Polynuclear Ruthenium(II) Photosensitizers Competent for Dehalogenation Photoredox Catalysis at 590 Nm. *J Am Chem Soc* **2020**, *142* (12), 5549–5555. https://doi.org/10.1021/jacs.0c01503.

(146) Cerfontaine, S.; Troian-Gautier, L.; Duez, Q.; Cornil, J.; Gerbaux, P.; Elias, B. MLCT Excited-State Behavior of Trinuclear Ruthenium(II) 2,2′-Bipyridine Complexes. *Inorg Chem* **2021**, *60* (1), 366–379. https://doi.org/10.1021/acs.inorgchem.0c03004.

(147) Ravetz, B. D.; Tay, N. E. S.; Joe, C. L.; Sezen-Edmonds, M.; Schmidt, M. A.; Tan, Y.; Janey, J. M.; Eastgate, M. D.; Rovis, T. Development of a Platform for Near-Infrared Photoredox Catalysis. *ACS Cent Sci* **2020**, *6* (11), 2053–2059. https://doi.org/10.1021/acscentsci.0c00948.

(148) Thompson, D. W.; Ito, A.; Meyer, T. J. [Ru(Bpy)3]2+* and Other Remarkable Metal-to-Ligand Charge Transfer (MLCT) Excited States. *Pure and Applied Chemistry* **2013**, *85* (7), 1257–1305. https://doi.org/10.1351/PAC-CON-13-03-04.

(149) Maurer, A. B.; Meyer, G. J. Stark Spectroscopic Evidence That a Spin Change Accompanies Light Absorption in Transition Metal Polypyridyl Complexes. *J Am Chem Soc* **2020**, *142* (15), 6847–6851. https://doi.org/10.1021/jacs.9b13602.

(150) Hofbeck, T.; Yersin, H. The Triplet State of Fac-Ir(Ppy)3. *Inorg Chem* **2010**, *49* (20), 9290–9299. https://doi.org/10.1021/ic100872w.

(151) Ravetz, B. D.; Pun, A. B.; Churchill, M.; Congreve, D. N.; Rovis, T.; Campos, L. M. Photoredox Catalysis Using Infrared Light via Triplet Fusion Upconversion. *Nature* **2019**, *565*, 343–346. https://doi.org/10.1038/s41586-018-0835-2.

(152) Freitag, M.; Möller, N.; Rühling, A.; Strassert, C. A.; Ravoo, B. J.; Glorius, F. Photocatalysis in the Dark: Near-Infrared Light Driven Photoredox Catalysis by an Upconversion Nanoparticle/Photocatalyst System. *ChemPhotoChem* **2019**, *3* (1), 24–27. https://doi.org/10.1002/cptc.201800212.

(153) Huang, L.; Wu, W.; Li, Y.; Huang, K.; Zeng, L.; Lin, W.; Han, G. Highly Effective Near-Infrared Activating Triplet-Triplet Annihilation Upconversion for Photoredox Catalysis. *J Am Chem Soc* **2020**, *142* (43), 18460–18470. https://doi.org/10.1021/jacs.0c06976.

(154) Yamazaki, Y.; Rohacova, J.; Koike, K.; Ishitani, O. Synthesis and Light-Harvesting Functions of Ring-Shaped Re(I) Trinuclear Complexes Connected with an Emissive Ru(II) Complex. *JACS Au* **2021**, *1* (3), 294–307. https://doi.org/10.1021/jacsau.0c00114.

(155) Kent, C. A.; Liu, D.; Ma, L.; Papanikolas, J. M.; Meyer, T. J.; Lin, W. Light Harvesting in Microscale Metal Organic Frameworks by Energy Migration and Interfacial Electron Transfer Quenching. *J Am Chem Soc* **2011**, *133* (33), 12940–12943. https://doi.org/https://doi.org/10.1021/ja204214t.

(156) Yamazaki, Y.; Rohacova, J.; Ohtsu, H.; Kawano, M.; Ishitani, O. Synthesis of Re(I) Rings Comprising Different Re(I) Units and Their Light-Harvesting Abilities. *Inorg Chem* **2018**, *57* (24), 15158–15171. https://doi.org/10.1021/acs.inorgchem.8b02421.

(157) Mattson, G.; Conklin, E.; Desai, S.; Nielander, G.; Savage, M. D.; Morgensen, S. A Practical Approach to Crosslinking. *Mol Biol Rep* **1993**, *17* (3), 167–183. https://doi.org/https://doi.org/10.1007/BF00986726.

(158) Mädler, S.; Bich, C.; Touboul, D.; Zenobi, R. Chemical Cross-Linking with NHS Esters: A Systematic Study on Amino Acid Reactivities. *Journal of Mass Spectrometry* **2009**, *44* (5), 694–706. https://doi.org/10.1002/jms.1544.

(159) Isailovic, D.; Li, H. W.; Yeung, E. S. Isolation and Characterization of R-Phycoerythrin Subunits and Enzymatic Digests. *J Chromatogr A* **2004**, *1051* (1–2), 119–130. https://doi.org/10.1016/j.chroma.2004.07.038.

(160) Damrauer, N. H.; Cerullo, G.; Yeh, A.; Boussie, T. R.; Shank, C. V.; McCusker, J. K. Femtosecond Dynamics of Excited-State Evolution in [Ru(Bpy)3]2+. *Science* **1997**, *11* (8), 621–625. https://doi.org/10.1126/science.275.5296.54.

(161) Mukuta, T.; Tanaka, S.; Inagaki, A.; Koshihara, S. Y.; Onda, K. Direct Observation of the Triplet Metal-Centered State in [Ru(Bpy)3]2+ Using Time-Resolved Infrared Spectroscopy. *ChemistrySelect* **2016**, *1* (1), 2802–2807. https://doi.org/10.1002/slct.201600747.

(162) Tyson, E. L.; Niemeyer, Z. L.; Yoon, T. P. Redox Mediators in Visible Light Photocatalysis: Photocatalytic Radical Thiol-Ene Additions. *Journal of Organic Chemistry* **2014**, *79* (3), 1427–1436. https://doi.org/10.1021/jo500031g.

(163) Gao, X. F.; Du, J. J.; Liu, Z.; Guo, J. Visible-Light-Induced Specific Desulfurization of Cysteinyl Peptide and Glycopeptide in Aqueous Solution. *Org Lett* **2016**, *18* (5), 1166–1169. https://doi.org/10.1021/acs.orglett.6b00292.

(164) Nolan, M. D.; Scanlan, E. M. Applications of Thiol-Ene Chemistry for Peptide Science. *Front Chem* **2020**, *8* (November), 1–21. https://doi.org/10.3389/fchem.2020.583272.

(165) Tyson, E. L.; Ament, M. S.; Yoon, T. P. Transition Metal Photoredox Catalysis of Radical Thiol-Ene Reactions. *Journal of Organic Chemistry* **2013**, *78* (5), 2046–2050. https://doi.org/10.1021/jo3020825.

(166) van Grondelle, R. Excitation Energy Transfer, Trapping and Annihilation in Photosynthetic Systems. *BBA Reviews On Bioenergetics* **1985**, *811* (2), 147–195. https://doi.org/10.1016/0304-4173(85)90017-5.

(167) Lindsey, J. S.; Taniguchi, M.; Bocian, D. F.; Holten, D. The Fluorescence Quantum Yield Parameter in Förster Resonance Energy Transfer (FRET)—Meaning, Misperception, and Molecular Design. *Chemical Physics Reviews* **2021**, *2* (1), 011302. https://doi.org/10.1063/5.0041132.

(168) Lange, J.-P. Performance Metrics for Sustainable Catalysis in Industry. *Nat Catal* **2021**, *4* (3), 186–192. https://doi.org/10.1038/s41929-021-00585-2.

(169) Mak, C. H.; Han, X.; Du, M.; Kai, J. J.; Tsang, K. F.; Jia, G.; Cheng, K. C.; Shen, H. H.; Hsu, H. Y. Heterogenization of Homogeneous Photocatalysts Utilizing Synthetic and Natural Support Materials. *J Mater Chem A Mater* **2021**, *9* (8), 4454–4504. https://doi.org/10.1039/d0ta08334h.

(170) Oi, V. T.; Glazer, A. N.; Stryer, L. Fluorescent Phycobiliprotein Conjugates for Analyses of Cells and Molecules. *J Cell Biol* **1982**, *93* (3), 981–986. https://doi.org/10.1083/jcb.93.3.981.

(171) Son, M.; Mosquera-Vasquez, S.; Schlau-Cohen, G. S. Ultrabroadband 2D Electronic Spectroscopy with High Speed, Shot-to-Shot Detection. *Opt Express* **2017**, *25* (16), 18950–18962. https://doi.org/https://doi.org/10.1364/OE.25.018950.

(172) Munier, M.; Jubeau, S.; Wijaya, A.; Morançais, M.; Dumay, J.; Marchal, L.; Jaouen, P.; Fleurence, J. Physicochemical Factors Affecting the Stability of Two Pigments: R-Phycoerythrin of Grateloupia Turuturu and B-Phycoerythrin of Porphyridium Cruentum. *Food Chem* **2014**, *150*, 400–407. https://doi.org/10.1016/j.foodchem.2013.10.113.

(173) Preus, S. *Scatter in UV-vis Absorption Spectra*. http://www.fluortools.com/software/ae/documentation/tools/scatter.

(174) Contreras-Martel, C.; Martinez-Oyanedel, J.; Bunster, M.; Legrand, P.; Piras, C.; Vernede, X.; Fontecilla-Camps, J. C. Crystallization and 2.2 Å Resolution Structure of R-Phycoerythrin from Gracilaria Chilensis: A Case of Perfect Hemihedral Twinning. *Acta Crystallogr D Biol Crystallogr* **2001**, *57* (1), 52–60. https://doi.org/10.1107/S0907444900015274.

(175) Isailovic, D.; Li, H. W.; Yeung, E. S. Isolation and Characterization of R-Phycoerythrin Subunits and Enzymatic Digests. *J Chromatogr A* **2004**, *1051* (1–2), 119–130. https://doi.org/10.1016/j.chroma.2004.07.038.

(176) Koushik, S. V.; Blank, P. S.; Vogel, S. S. Anomalous Surplus Energy Transfer Observed with Multiple FRET Acceptors. *PLoS One* **2009**, *4* (11), e8031. https://doi.org/10.1371/journal.pone.0008031.

(177) Son, M.; Mosquera-Vasquez, S.; Schlau-Cohen, G. S. Ultrabroadband 2D Electronic Spectroscopy with High Speed, Shot-to-Shot Detection. *Opt Express* **2017**, *25* (16), 18950–18962. https://doi.org/10.1364/OE.25.018950.

(178) Pervak, V.; Ahmad, I.; Trubetskov, M. K.; Tikhonravov, A. V.; Krausz, F. Double-Angle Multilayer Mirrors with Smooth Dispersion Characteristics. *Opt Express* **2009**, *17* (10), 7943. https://doi.org/10.1364/oe.17.007943.

(179) van Grondelle, R. Excitation Energy Transfer, Trapping and Annihilation in Photosynthetic Systems. *Biochim Biophys Acta Bioenerg* **1985**, *811* (2), 147–195. https://doi.org/10.1016/0304-4173(85)90017-5.

(180) Snellenburg, J. J.; Laptenok, S.; Seger, R.; Mullen, K. M.; van Stokkum, I. H. M. Glotaran: A Java-Based Graphical User Interface for the R Package TIMP. *J Stat Softw* **2012**, *49* (3), 1–22. https://doi.org/10.18637/jss.v049.i03.

(181) Chen, H.; Dang, W.; Xie, J.; Zhao, J.; Weng, Y. Ultrafast Energy Transfer Pathways in R-Phycoerythrin from Polysiphonia Urceolata. *Photosynth Res* **2012**, *111* (1–2), 81–86. https://doi.org/10.1007/s11120-011-9708-3.

(182) Tyson, E. L.; Niemeyer, Z. L.; Yoon, T. P. Redox Mediators in Visible Light Photocatalysis: Photocatalytic Radical Thiol-Ene Additions. *Journal of Organic Chemistry* **2014**, *79* (3), 1427–1436. https://doi.org/10.1021/jo500031g.

(183) Xu, W. Z.; Zhang, X.; Kadla, J. F. Design of Functionalized Cellulosic Honeycomb Films: Site-Specific Biomolecule Modification via "Click Chemistry." *Biomacromolecules* **2012**, *13* (2), 350–357. https://doi.org/10.1021/bm201364r.

(184) Merbouh, N.; Wallner, F. K.; Cociorva, O. M.; Seeberger, P. H. 3-Mercaptopropanol as a Traceless Linker for Chemical and Enzymatic Synthesis of Oligosaccharides. *Org Lett* **2007**, *9* (4), 651–653. https://doi.org/10.1021/ol062922y.

(185) Hennessy, E. T.; Betley, T. A. Complex N-Heterocycle Synthesis via Iron-Catalyzed, Direct C-H Bond Amination. *Science* **2013**, *340* (May), 591–596. https://doi.org/10.1126/science.1233701.

(186) Dondoni, A.; Massi, A.; Nanni, P.; Roda, A. A New Ligation Strategy for Peptide and Protein Glycosylation: Photoinduced Thiol-Ene Coupling. *Chemistry - A European Journal* **2009**, *15* (43), 11444–11449. https://doi.org/10.1002/chem.200901746.

(187) Gao, X. F.; Du, J. J.; Liu, Z.; Guo, J. Visible-Light-Induced Specific Desulfurization of Cysteinyl Peptide and Glycopeptide in Aqueous Solution. *Org Lett* **2016**, *18* (5), 1166–1169. https://doi.org/10.1021/acs.orglett.6b00292.

(188) Lehóczki, T.; Józsa, É.; Osz, K. Ferrioxalate Actinometry with Online Spectrophotometric Detection. *J Photochem Photobiol A Chem* **2013**, *251*, 63–68. https://doi.org/10.1016/j.jphotochem.2012.10.005.

(189) Reiß, B.; Hu, Q.; Riedle, E.; Wagenknecht, H.-A. The Dependence of Chemical Quantum Yields of Visible Light Photoredox Catalysis on the Irradiation Power. *ChemPhotoChem* **2021**. https://doi.org/10.1002/cptc.202100090.

(190) Patti, A.; Sanfilippo, C. Stereoselective Promiscuous Reactions Catalyzed by Lipases. *Int J Mol Sci* **2022**, *23* (5), 2675. https://doi.org/10.3390/ijms23052675.

(191) Hall, M. Enzymatic Strategies for Asymmetric Synthesis. *RSC Chem Biol* **2021**, *2* (4), 958–989. https://doi.org/10.1039/d1cb00080b.

(192) Losada-Garcia, N.; Cabrera, Z.; Urrutia, P.; Garcia-Sanz, C.; Andreu, A.; Palomo, J. M. Recent Advances in Enzymatic and Chemoenzymatic Cascade Processes. *Catalysts* **2020**, *10* (11), 1258. https://doi.org/10.3390/catal10111258.

(193) Li, R.; Kong, W.; An, Z. Enzyme Catalysis for Reversible Deactivation Radical Polymerization. *Angew. Chem. Int. Ed.* **2022**, e202202033. https://doi.org/10.1002/anie.202202033.

(194) Athavale, S. V.; Gao, S.; Liu, Z.; Mallojjala, S. C.; Hirschi, J. S.; Arnold, F. H. Biocatalytic, Intermolecular C−H Bond Functionalization for the Synthesis of Enantioenriched Amides. *Angew. Chem. Int. Ed.* **2021**, *60* (47), 24864–24869. https://doi.org/10.1002/anie.202110873.

(195) Liu, Z.; Qin, Z. Y.; Zhu, L.; Athavale, S. V.; Sengupta, A.; Jia, Z. J.; Garcia-Borràs, M.; Houk, K. N.; Arnold, F. H. An Enzymatic Platform for Primary Amination of 1-Aryl-2-Alkyl Alkynes. *J Am Chem Soc* **2022**, *144* (1), 80–85. https://doi.org/10.1021/jacs.1c11340.

(196) Liu, Z.; Calvó-Tusell, C.; Zhou, A. Z.; Chen, K.; Garcia-Borràs, M.; Arnold, F. H. Dual-Function Enzyme Catalysis for Enantioselective Carbon–Nitrogen Bond Formation. *Nat Chem* **2021**, *13* (12), 1166–1172. https://doi.org/10.1038/s41557-021-00794-z.

(197) Miller, D. C.; Athavale, S. V.; Arnold, F. H. Combining Chemistry and Protein Engineering for New-to-Nature Biocatalysis. *Nature Synthesis* **2022**, *1* (1), 18–23. https://doi.org/10.1038/s44160-021-00008-x.

(198) Biegasiewicz, K. F.; Cooper, S. J.; Gao, X.; Oblinsky, D. G.; Kim, J. H.; Garfinkle, S. E.; Joyce, L. A.; Sandoval, B. A.; Scholes, G. D.; Hyster, T. K. Photoexcitation of

Flavoenzymes Enables a Stereoselective Radical Cyclization. *Science* **2019**, *364* (6446), 1166–1169. https://doi.org/10.1126/science.aaw1143.

(199) Nicholls, B. T.; Qiao, T.; Hyster, T. K. A Photoenzyme for Challenging Lactam Radical Cyclizations. *Synlett* **2022**, *33* (12), 1204–1208. https://doi.org/10.1055/s-0040-1719872.

(200) Gao, X.; Turek-Herman, J. R.; Choi, Y. J.; Cohen, R. D.; Hyster, T. K. Photoenzymatic Synthesis of α-Tertiary Amines by Engineered Flavin-Dependent "Ene"-Reductases. *J Am Chem Soc* **2021**, *143* (47), 19643–19647. https://doi.org/10.1021/jacs.1c09828.

(201) Clayman, P. D.; Hyster, T. K. Photoenzymatic Generation of Unstabilized Alkyl Radicals: An Asymmetric Reductive Cyclization. *J Am Chem Soc* **2020**, *142* (37), 15673–15677. https://doi.org/10.1021/jacs.0c07918.

(202) Sandoval, B. A.; Clayman, P. D.; Oblinsky, D. G.; Oh, S.; Nakano, Y.; Bird, M.; Scholes, G. D.; Hyster, T. K. Photoenzymatic Reductions Enabled by Direct Excitation of Flavin-Dependent "Ene"-Reductases. *J Am Chem Soc* **2021**, *143* (4), 1735–1739. https://doi.org/10.1021/jacs.0c11494.

(203) Nicholls, B. T.; Oblinsky, D. G.; Kurtoic, S. I.; Grosheva, D.; Ye, Y.; Scholes, G. D.; Hyster, T. K. Engineering a Non-Natural Photoenzyme for Improved Photon Efficiency. *Angew. Chem. Int. Ed.* **2022**, *61*, e202113842. https://doi.org/10.1002/anie.202113842.

(204) Page, C. G.; Cooper, S. J.; Dehovitz, J. S.; Oblinsky, D. G.; Biegasiewicz, K. F.; Antropow, A. H.; Armbrust, K. W.; Ellis, J. M.; Hamann, L. G.; Horn, E. J.; Oberg, K. M.; Scholes, G. D.; Hyster, T. K. Quaternary Charge-Transfer Complex Enables Photoenzymatic Intermolecular Hydroalkylation of Olefins. *J Am Chem Soc* **2021**, *143* (1), 97–102. https://doi.org/10.1021/jacs.0c11462.

(205) Zhang, S.; Liu, S.; Sun, Y.; Li, S.; Shi, J.; Jiang, Z. Enzyme-Photo-Coupled Catalytic Systems. *Chem Soc Rev* **2021**, *50* (24), 13449–13466. https://doi.org/10.1039/d1cs00392e.

(206) Chen, J.; Guan, Z.; He, Y. H. Photoenzymatic Approaches in Organic Synthesis. *Asian J Org Chem* **2019**, *8* (10), 1775–1790. https://doi.org/10.1002/ajoc.201900427.

(207) Su, D.; Kabir, M. P.; Orozco-Gonzalez, Y.; Gozem, S.; Gadda, G. Fluorescence Properties of Flavin Semiquinone Radicals in Nitronate Monooxygenase. *ChemBioChem* **2019**, *20* (13), 1646–1652. https://doi.org/10.1002/cbic.201900016.

(208) Scholes, G. D.; Mirkovic, T.; Turner, D. B.; Fassioli, F.; Buchleitner, A. Solar Light Harvesting by Energy Transfer: From Ecology to Coherence. *Energy Environ Sci* **2012**, *5* (11), 9374–9393. https://doi.org/10.1039/c2ee23013e.

(209) Scholes, G. D.; Fleming, G. R.; Olaya-Castro, A.; Van Grondelle, R. Lessons from Nature about Solar Light Harvesting. *Nat Chem* **2011**, *3* (10), 763–774. https://doi.org/10.1038/nchem.1145.

(210) Van Grondelle, R.; Dekker, J. P.; Gillbro, T.; Sundstrom, V. Energy Transfer and Trapping in Photosynthesis. *Biochimica et Biophysica Acta* **1994**, *1187* (1), 1–65. https://doi.org/10.1016/0005-2728(94)90166-X.

(211) Cogdell, R. J.; Gall, A.; Köhler, J. The Architecture and Function of the Light-Harvesting Apparatus of Purple Bacteria: From Single Molecules to in Vivo Membranes. *Q Rev Biophys* **2006**, *39* (3), 227–324. https://doi.org/10.1017/S0033583506004434.

(212) Croce, R.; van Amerongen, H. Light Harvesting in Oxygenic Photosynthesis: Structural Biology Meets Spectroscopy. *Science* **2020**, *369* (6506), eaay2058. https://doi.org/10.1126/science.aay2058.

(213) Glaser, F.; Kerzig, C.; Wenger, O. S. Sensitization-Initiated Electron Transfer via Upconversion: Mechanism and Photocatalytic Applications. *Chem Sci* **2021**, *12* (29), 9922–9933. https://doi.org/10.1039/d1sc02085d.

(214) Amoruso, G.; Liu, J.; Polak, D. W.; Tiwari, K.; Jones, M. R.; Oliver, T. A. A. High-Efficiency Excitation Energy Transfer in Biohybrid Quantum Dot-Bacterial Reaction Center Nanoconjugates. *Journal of Physical Chemistry Letters* **2021**, *12* (23), 5448–5455. https://doi.org/10.1021/acs.jpclett.1c01407.

(215) Cesana, P. T.; Li, B. X.; Shepard, S. G.; Ting, S. I.; Hart, S. M.; Olson, C. M.; Martinez Alvarado, J. I.; Son, M.; Steiman, T. J.; Castellano, F. N.; Doyle, A. G.; MacMillan, D. W. C.; Schlau-Cohen, G. S. A Biohybrid Strategy for Enabling Photoredox Catalysis with Low-Energy Light. *Chem* **2022**, *8*, 1–12. https://doi.org/10.1016/j.chempr.2021.10.010.

(216) Gordiichuk, P. I.; Rimmerman, D.; Paul, A.; Gautier, D. A.; Gruszka, A.; Saller, M.; De Vries, J. W.; Wetzelaer, G. J. A. H.; Manca, M.; Gomulya, W.; Matmor, M.; Gloukhikh, E.; Loznik, M.; Ashkenasy, N.; Blom, P. W. M.; Rögner, M.; Loi, M. A.; Richter, S.; Herrmann, A. Filling the Green Gap of a Megadalton Photosystem I Complex by Conjugation of Organic Dyes. *Bioconjug Chem* **2016**, *27* (1), 36–41. https://doi.org/10.1021/acs.bioconjchem.5b00583.

(217) Valdes-Aguilera, O.; Neckers, D. C. Aggregation Phenomena in Xanthene Dyes. *Acc. Chem. Res.* **1989**, *22* (5), 171–177.

(218) Valeur, B.; Berberan-Santos, M. N. *Molecular Fluorescence: Principles and Applications*, 2nd ed.; Wiley-VCH: Weinheim, Germany, 2012.

(219) ATTO-TEC. *Recommended Procedures for Labeling*. https://www.atto-tec.com/fileadmin/user_upload/Katalog_Flyer_Support/Procedures.pdf (accessed 2021-09-15).

(220) Biegasiewicz, K. F.; Cooper, S. J.; Gao, X.; Oblinsky, D. G.; Kim, J. H.; Garfinkle, S. E.; Joyce, L. A.; Sandoval, B. A.; Scholes, G. D.; Hyster, T. K. Photoexcitation of Flavoenzymes Enables a Stereoselective Radical Cyclization. *Science* **2019**, *364* (6446), 1166–1169. https://doi.org/10.1126/science.aaw1143.

(221) Saito, R.; Sato, T.; Ikai, A.; Tanaka, N. Structure of Bovine Carbonic Anhydrase II at 1.95 Å Resolution. *Acta Crystallogr D Biol Crystallogr* **2004**, *60* (4), 792–795. https://doi.org/10.1107/S0907444904003166.

(222) Su, D.; Kabir, M. P.; Orozco-Gonzalez, Y.; Gozem, S.; Gadda, G. Fluorescence Properties of Flavin Semiquinone Radicals in Nitronate Monooxygenase. *ChemBioChem* **2019**, *20* (13), 1646–1652. https://doi.org/10.1002/cbic.201900016.

(223) Zhuang, B.; Liebl, U.; Vos, M. H. Flavoprotein Photochemistry: Fundamental Processes and Photocatalytic Perspectives. *J Phys Chem B* **2022**, *126* (17), 3199–3207. https://doi.org/10.1021/acs.jpcb.2c00969.

(224) Fábián, Á. I.; Rente, T.; SzölloSi, J.; Matyus, L.; Jenei, A. Strength in Numbers: Effects of Acceptor Abundance on FRET Efficiency. *ChemPhysChem* **2010**, *11* (17), 3713–3721. https://doi.org/10.1002/cphc.201000568.

(225) Page, C. G.; Cooper, S. J.; Dehovitz, J. S.; Oblinsky, D. G.; Biegasiewicz, K. F.; Antropow, A. H.; Armbrust, K. W.; Ellis, J. M.; Hamann, L. G.; Horn, E. J.; Oberg, K. M.; Scholes, G. D.; Hyster, T. K. Quaternary Charge-Transfer Complex Enables Photoenzymatic Intermolecular Hydroalkylation of Olefins. *J Am Chem Soc* **2021**, *143* (1), 97–102. https://doi.org/10.1021/jacs.0c11462.

(226) Gaigalas, A.; Gallagher, T.; Cole, K. D.; Singh, T.; Wang, L.; Zhang, Y.-Z. A Multistate Model for the Fluorescence Response of R-Phycoerythrin. *Photochem Photobiol* **2006**, *82* (3), 635. https://doi.org/10.1562/2005-05-26-ra-544.

(227) Hockin, B. M.; Li, C.; Robertson, N.; Zysman-Colman, E. Photoredox Catalysts Based on Earth-Abundant Metal Complexes. *Catal Sci Technol* **2019**, *9* (4), 889–915. https://doi.org/10.1039/c8cy02336k.

(228) Hazel, G. B.; Hedrick, J. B.; Orris, G. J. *Rare Earth Elements-Critical Resources for High Technology*; 2002.

(229) McCusker, J. K. Electronic Structure in the Transition Metal Block and Its Implications for Light Harvesting. *Science* **2019**, *363* (6426), 484–488. https://doi.org/10.1126/science.aav9104.

(230) Woodhouse, M. D.; McCusker, J. K. Mechanistic Origin of Photoredox Catalysis Involving Iron(II) Polypyridyl Chromophores. *J Am Chem Soc* **2020**, *142* (38), 16229–16233. https://doi.org/10.1021/jacs.0c08389.

(231) Hossain, A.; Bhattacharyya, A.; Reiser, O. Copper's Rapid Ascent in Visible-Light Photoredox Catalysis. *Science* **2019**, *364* (6439), eaav9713. https://doi.org/10.1126/science.aav9713.

(232) Rosko, M. C.; Espinoza, E. M.; Arteta, S.; Kromer, S.; Wheeler, J. P.; Castellano, F. N. Employing Long-Range Inductive Effects to Modulate Metal-to-Ligand Charge Transfer Photoluminescence in Homoleptic Cu(I) Complexes. *Inorg Chem* **2023**, *62* (7), 3248–3259. https://doi.org/10.1021/acs.inorgchem.2c04315.

(233) Capano, G.; Chergui, M.; Rothlisberger, U.; Tavernelli, I.; Penfold, T. J. A Quantum Dynamics Study of the Ultrafast Relaxation in a Prototypical Cu(I)-Phenanthroline. *Journal of Physical Chemistry A* **2014**, *118* (42), 9861–9869. https://doi.org/10.1021/jp509728m.

(234) Shaw, G. B.; Grant, C. D.; Shirota, H.; Castner, E. W.; Meyer, G. J.; Chen, L. X. Ultrafast Structural Rearrangements in the MLCT Excited State for Copper(I) Bis-Phenanthrolines in Solution. *J Am Chem Soc* **2007**, *129* (7), 2147–2160. https://doi.org/10.1021/ja067271f.

(235) Biswas, S.; Kim, J. W.; Zhang, X.; Scholes, G. D. Coherent Two-Dimensional and Broadband Electronic Spectroscopies. *Chemical Reviews*. American Chemical Society February 9, 2022, pp 4257–4321. https://doi.org/10.1021/acs.chemrev.1c00623.

(236) Anna, J. M.; Song, Y.; Dinshaw, R.; Scholes, G. D. Two-Dimensional Electronic Spectroscopy for Mapping Molecular Photophysics. *Pure and Applied Chemistry* **2013**, *85* (7), 1307–1319. https://doi.org/10.1351/PAC-CON-12-10-21.

(237) Petkov, B. K.; Gellen, T. A.; Farfan, C. A.; Carbery, W. P.; Hetzler, B. E.; Trauner, D.; Li, X.; Glover, W. J.; Ulness, D. J.; Turner, D. B. Two-Dimensional Electronic Spectroscopy Reveals the Spectral Dynamics of Förster Resonance Energy Transfer. *Chem* **2019**, *5* (8), 2111–2125. https://doi.org/10.1016/j.chempr.2019.05.005.

(238) Yang, X.; Ullah, Z.; Stoddart, J. F.; Yavuz, C. T. Porous Organic Cages. *Chem Rev* **2023**, *123* (8), 4602–4634. https://doi.org/10.1021/acs.chemrev.2c00667.

(239) Aprahamian, I.; Goldup, S. M. Non-Equilibrium Steady States in Catalysis, Molecular Motors, and Supramolecular Materials: Why Networks and Language Matter. *J Am Chem Soc* **2023**, *145* (26), 14169–14183. https://doi.org/10.1021/jacs.2c12665.

(240) Hane, F. T.; Fernando, A.; Prete, B. R. J.; Peloquin, B.; Karas, S.; Chaudhuri, S.; Chahal, S.; Shepelytskyi, Y.; Wade, A.; Li, T.; Deboef, B.; Albert, M. S. Cyclodextrin-Based Pseudorotaxanes: Easily Conjugatable Scaffolds for Synthesizing Hyperpolarized Xenon-

129 Magnetic Resonance Imaging Agents. *ACS Omega* **2018**, *3* (1), 677–681. https://doi.org/10.1021/acsomega.7b01744.

(241) Kumar, M.; Venkata Rao, K.; George, S. J. Supramolecular Charge Transfer Nanostructures. *Physical Chemistry Chemical Physics* **2014**, *16* (4), 1300–1313. https://doi.org/10.1039/c3cp54190h.

(242) Xiao, T.; Zhang, L.; Wu, H.; Qian, H.; Ren, D.; Li, Z. Y.; Sun, X. Q. Supramolecular Polymer-Directed Light-Harvesting System Based on a Stepwise Energy Transfer Cascade. *Chemical Communications* **2021**, *57* (47), 5782–5785. https://doi.org/10.1039/d1cc01788h.

(243) Han, Y.; Zhang, X.; Ge, Z.; Gao, Z.; Liao, R.; Wang, F. A Bioinspired Sequential Energy Transfer System Constructed via Supramolecular Copolymerization. *Nat Commun* **2022**, *13*, 3546. https://doi.org/10.1038/s41467-022-31094-w.

(244) Bouwens, T.; Bakker, T. M. A.; Zhu, K.; Hasenack, J.; Dieperink, M.; Brouwer, A. M.; Huijser, A.; Mathew, S.; Reek, J. N. H. Using Supramolecular Machinery to Engineer Directional Charge Propagation in Photoelectrochemical Devices. *Nat Chem* **2023**, *15* (2), 213–221. https://doi.org/10.1038/s41557-022-01068-y.

(245) Das, A.; Ghosh, S. Supramolecular Assemblies by Charge-Transfer Interactions between Donor and Acceptor Chromophores. *Angewandte Chemie - International Edition* **2014**, *53* (8), 2038–2054. https://doi.org/10.1002/anie.201307756.

(246) Wu, K.; Benchimol, E.; Baksi, A.; Clever, G. H. Non-Statistical Assembly of Multicomponent [Pd2ABCD] Cages. *Nat Chem* **2024**, *16* (4), 584–591. https://doi.org/10.1038/s41557-023-01415-7.

(247) Benchimol, E.; Ebbert, K. E.; Walther, A.; Holstein, J. J.; Clever, G. H. Ligand Conformation Controls Assembly of a Helicate/Mesocate, Heteroleptic [Pd2L2L'2] Cages and a Six-Jagged [Pd6L12] Ring. *Chemistry – A European Journal* **2024**, e202401850. https://doi.org/10.1002/chem.202401850.

(248) Neukirch, L.; Kulas, M. D.; Holstein, J. J.; Clever, G. H. Non-Templated Assembly of D5h-Symmetric Pd5L10 Rings by Precise Ligand Angle Adjustment. *Chemistry - A European Journal* **2024**, *30* (27), e202400132. https://doi.org/10.1002/chem.202400132.

(249) Ryu, K. A.; Kaszuba, C. M.; Bissonnette, N. B.; Oslund, R. C.; Fadeyi, O. O. Interrogating Biological Systems Using Visible-Light-Powered Catalysis. *Nat Rev Chem* **2021**, *5* (5), 322–337. https://doi.org/10.1038/s41570-021-00265-6.

(250) Cabanero, D. C.; Kariofillis, S. K.; Johns, A. C.; Kim, J.; Ni, J.; Park, S.; Parker, D. L.; Ramil, C. P.; Roy, X.; Shah, N. H.; Rovis, T. Photocatalytic Activation of Aryl(Trifluoromethyl) Diazos to Carbenes for High-Resolution Protein Labeling with Red Light. *J Am Chem Soc* **2024**, *146* (2), 1337–1345. https://doi.org/10.1021/jacs.3c09545.

(251) Li, P.; Terrett, J. A.; Zbieg, J. R. Visible-Light Photocatalysis as an Enabling Technology for Drug Discovery: A Paradigm Shift for Chemical Reactivity. *ACS Med Chem Lett* **2020**, *11* (11), 2120–2130. https://doi.org/10.1021/acsmedchemlett.0c00436.

(252) Faustova, M.; Nikolskaya, E.; Sokol, M.; Fomicheva, M.; Petrov, R.; Yabbarov, N. Metalloporphyrins in Medicine: From History to Recent Trends. *ACS Appl Bio Mater* **2020**, *3* (12), 8146–8171. https://doi.org/10.1021/acsabm.0c00941.

(253) Rybicka-Jasińska, K.; Wdowik, T.; Łuczak, K.; Wierzba, A. J.; Drapała, O.; Gryko, D. Porphyrins as Promising Photocatalysts for Red-Light-Induced Functionalizations of Biomolecules. *ACS Organic and Inorganic Au* **2022**, *2* (5), 422–426. https://doi.org/10.1021/acsorginorgau.2c00025.

(254) Chapman, S. J.; Swords, W. B.; Le, C. M.; Guzei, I. A.; Toste, F. D.; Yoon, T. P. Cooperative Stereoinduction in Asymmetric Photocatalysis. *J Am Chem Soc* **2022**, *144* (9), 4206–4213. https://doi.org/10.1021/jacs.2c00063.

(255) Yoon, T. P. Photochemical Stereocontrol Using Tandem Photoredox-Chiral Lewis Acid Catalysis. *Acc Chem Res* **2016**, *49* (10), 2307–2315. https://doi.org/10.1021/acs.accounts.6b00280.

(256) Wang, Y.; Xue, P.; Cao, M.; Yu, T.; Lane, S. T.; Zhao, H. Directed Evolution: Methodologies and Applications. *Chem Rev* **2021**, *121* (20), 12384–12444. https://doi.org/10.1021/acs.chemrev.1c00260.

(257) Alphand, V.; van Berkel, W. J. H.; Jurkaš, V.; Kara, S.; Kourist, R.; Kroutil, W.; Mascia, F.; Nowaczyk, M. M.; Paul, C. E.; Schmidt, S.; Spasic, J.; Tamagnini, P.; Winkler, C. K. Exciting Enzymes: Current State and Future Perspective of Photobiocatalysis. *ChemPhotoChem* **2023**, *7* (7). https://doi.org/10.1002/cptc.202200325.

(258) de Kok, N. A. W.; Schmidt, S. Tapping into Abiological Reaction Chemistries in Biocatalysis. *Chem Catalysis* **2023**, *3* (100493). https://doi.org/10.1016/j.checat.2022.100493.

(259) Carceller, J. M.; Jayee, B.; Page, C. G.; Oblinsky, D. G.; Chintala, N.; Mondragón-Solórzano, G.; Cao, J.; Alassad, Z.; Zhang, Z.; White, N.; Scholes, G. D.; Dong, S. S.; Hyster, T. K. Engineering a Photoenzyme to Use Red Light. *ChemRxiv* **2024**, No. This content is a preprint and has not been peer reviewed. https://doi.org/10.26434/chemrxiv-2024-cjs5j.

(260) Lee, A.; Son, M.; Deegbey, M.; Woodhouse, M. D.; Hart, S. M.; Beissel, H. F.; Cesana, P. T.; Jakubikova, E.; McCusker, J. K.; Schlau-Cohen, G. S. Observation of Parallel Intersystem Crossing and Charge Transfer-State Dynamics in [Fe(Bpy)3]2+ from Ultrafast 2D Electronic Spectroscopy. *Chem Sci* **2023**, *14* (45), 13140–13150. https://doi.org/10.1039/d3sc02613b.

(261) Auböck, G.; Chergui, M. Sub-50-Fs Photoinduced Spin Crossover in [Fe(Bpy)3]2+. *Nat Chem* **2015**, *7* (8), 629–633. https://doi.org/10.1038/nchem.2305.

(262) Sinha, N.; Wenger, O. S. Photoactive Metal-to-Ligand Charge Transfer Excited States in 3d6 Complexes with Cr0, MnI, FeII, and CoIII. *J Am Chem Soc* **2023**, *145* (9), 4903–4920. https://doi.org/10.1021/jacs.2c13432.

(263) Sinha, N.; Wegeberg, C.; Häussinger, D.; Prescimone, A.; Wenger, O. S. Photoredox-Active Cr(0) Luminophores Featuring Photophysical Properties Competitive with Ru(II) and Os(II) Complexes. *Nat Chem* **2023**, *15* (12), 1730–1736. https://doi.org/10.1038/s41557-023-01297-9.

(264) Bruschi, C.; Gui, X.; Fuhr, O.; Klopper, W.; Bizzarri, C. Reaching Strong Absorption up to 700 Nm with New Benzo[g]Quinoxaline-Based Heteroleptic Copper(i) Complexes for Light-Harvesting Applications. *Dalton Transactions* **2023**, *52* (23), 7809–7818. https://doi.org/10.1039/d3dt00902e.

(265) Ghosh, A.; Yarranton, J. T.; McCusker, J. K. Establishing the Origin of Marcus-Inverted-Region Behaviour in the Excited-State Dynamics of Cobalt(III) Polypyridyl Complexes. *Nat Chem* **2024**. https://doi.org/10.1038/s41557-024-01564-3.

(266) Chan, A. Y.; Ghosh, A.; Yarranton, J. T.; Twilton, J.; Jin, J.; Arias-Rotondo, D. M.; Sakai, H. A.; McCusker, J. K.; C MacMillan, D. W. Exploiting the Marcus Inverted Region for First-Row Transition Metal-Based Photoredox Catalysis. *Science* **2023**, *382*, 191–197.

(267) Sittel, S.; Naumann, R.; Heinze, K. Molecular Rubies in Photoredox Catalysis. *Front Chem* **2022**, *10*, 887439. https://doi.org/10.3389/fchem.2022.887439.

(268) Trippmacher, S.; Demeshko, S.; Prescimone, A.; Meyer, F.; Wenger, O. S.; Wang, C. Ferromagnetically Coupled Chromium(III) Dimer Shows Luminescence and Sensitizes Photon Upconversion. *Chemistry - A European Journal* **2024**, *30* (31), e202400856. https://doi.org/10.1002/chem.202400856.

(269) Kitzmann, W. R.; Hunger, D.; Reponen, A. P. M.; Förster, C.; Schoch, R.; Bauer, M.; Feldmann, S.; van Slageren, J.; Heinze, K. Electronic Structure and Excited-State Dynamics of the NIR-II Emissive Molybdenum(III) Analogue to the Molecular Ruby. *Inorg Chem* **2023**, *62* (39), 15797–15808. https://doi.org/10.1021/acs.inorgchem.3c02186.

(270) Wang, C.; Reichenauer, F.; Kitzmann, W. R.; Kerzig, C.; Heinze, K.; Resch-Genger, U. Efficient Triplet-Triplet Annihilation Upconversion Sensitized by a Chromium(III) Complex via an Underexplored Energy Transfer Mechanism. *Angewandte Chemie - International Edition* **2022**, *61* (27), e202202238. https://doi.org/10.1002/anie.202202238.

(271) Li, C.; Kong, X. Y.; Tan, Z. H.; Yang, C. T.; Soo, H. Sen. Emergence of Ligand-to-Metal Charge Transfer in Homogeneous Photocatalysis and Photosensitization. *Chemical Physics Reviews* **2022**, *3* (2), 021303. https://doi.org/10.1063/5.0086718.

(272) Glaser, F.; Wenger, O. S. Red Light-Based Dual Photoredox Strategy Resembling the Z-Scheme of Natural Photosynthesis. *JACS Au* **2022**, *2* (6), 1488–1503. https://doi.org/10.1021/jacsau.2c00265.

(273) Yang, Y. Y.; Zhang, P.; Hadjichristidis, N. Two-Photon Excitation Photoredox Catalysis Enabled Atom Transfer Radical Polymerization. *J Am Chem Soc* **2023**, *145* (23), 12737–12744. https://doi.org/10.1021/jacs.3c02832.

(274) Ilic, A.; Schwarz, J.; Johnson, C.; de Groot, L. H. M.; Kaufhold, S.; Lomoth, R.; Wärnmark, K. Photoredox Catalysis via Consecutive 2LMCT- and 3MLCT-Excitation of an Fe(Iii/Ii)-N-Heterocyclic Carbene Complex. *Chem Sci* **2022**, *13* (32), 9165–9175. https://doi.org/10.1039/d2sc02122f.